

Air Force Institute of Technology

AFIT Scholar

Theses and Dissertations

Student Graduate Works

9-2022

Optimizing Optical Switching of Non-linear Optimizing Optical Switching of Non-linear Hyperbolic Metamaterials

James A. Ethridge

Follow this and additional works at: <https://scholar.afit.edu/etd>



Part of the [Optics Commons](#)

Recommended Citation

Ethridge, James A., "Optimizing Optical Switching of Non-linear Optimizing Optical Switching of Non-linear Hyperbolic Metamaterials" (2022). *Theses and Dissertations*. 5547.
<https://scholar.afit.edu/etd/5547>

This Dissertation is brought to you for free and open access by the Student Graduate Works at AFIT Scholar. It has been accepted for inclusion in Theses and Dissertations by an authorized administrator of AFIT Scholar. For more information, please contact AFIT.ENWL.Repository@us.af.mil.



**Optimizing Optical Switching of Non-linear
Hyperbolic Metamaterials**

DISSERTATION

James A. Ethridge
AFIT-ENP-DS-22-S-042

**DEPARTMENT OF THE AIR FORCE
AIR UNIVERSITY**

AIR FORCE INSTITUTE OF TECHNOLOGY

Wright-Patterson Air Force Base, Ohio

DISTRIBUTION STATEMENT A.

APPROVED FOR PUBLIC RELEASE; DISTRIBUTION UNLIMITED

The views expressed in this document are those of the author and do not reflect the official policy or position of the United States Air Force, the United States Department of Defense or the United States Government. This material is declared a work of the U.S. Government and is not subject to copyright protection in the United States.

AFIT-ENP-DS-22-S-042

OPTIMIZING OPTICAL SWITCHING OF NON-LINEAR HYPERBOLIC
METAMATERIALS

DISSERTATION

Presented to the Faculty
Graduate School of Engineering and Management
Air Force Institute of Technology
Air University
Air Education and Training Command
in Partial Fulfillment of the Requirements for the
Degree of Doctorate of Philosophy in Applied Physics

James A. Ethridge, B.S, M.S.

September 15, 2022

DISTRIBUTION STATEMENT A.

APPROVED FOR PUBLIC RELEASE; DISTRIBUTION UNLIMITED

AFIT-ENP-DS-22-S-042

OPTIMIZING OPTICAL SWITCHING OF NON-LINEAR HYPERBOLIC
METAMATERIALS

DISSERTATION

James A. Ethridge, B.S, M.S.

Committee Membership:

Dr. M. A. Marciniak
Chair

Dr. A. K. Patnaik
Member

Dr. M. J. Havrilla
Member

Dr. J. G. Jones
Member

Dr. M. D. Ferdinandus
Member

Abstract

Modern optical materials are engineered to be used as optical devices in specific applications, such as optical computing. For optical computing, efficient forms of a particular device, the optical switch, have still not been successfully demonstrated. This problem is addressed in this research through the use of designed optical metamaterials, specifically, hyperbolic metamaterials, which offer the possibility of large non-linear properties with a low switching intensity. One-dimensional layered hyperbolic metamaterials composed of alternating layers metal and dielectric were used here, with ITO as the metal and SiO₂ as the dielectric. The non-linear behavior of the ITO/SiO₂ layered structure was first modeled and optimized. Samples were then fabricated using this optimized design through physical vapor deposition at the Materials and Manufacturing Directorate of the Air Force Research Laboratory, and the linear and non-linear properties of these samples were measured by ellipsometry and the Z-scan technique, respectively. These materials showed a large enhancement of their effective nonlinear properties, and an intensity-dependent switching behavior where the sign of the non-linear absorption coefficient changes from positive to negative. This switching behavior has a switching intensity near 15 GW/cm² and switching width of about 0.15. This is the first experimental demonstration of such behavior in a simple one-dimensional layered hyperbolic metamaterial. Since this behavior is tunable, this technique may now be used to further engineer devices for specific applications. The unique properties of these materials increase their potential for use in optical switching applications.

Table of Contents

	Page
Abstract	iv
List of Tables	vii
List of Figures	viii
I. Introduction	1
1.1 General Issue	1
1.2 Relevant Research	1
1.3 Research Process	2
1.4 Limitations and Challenges	3
1.5 Document Overview	4
II. Theoretical Background	5
2.1 Chapter Overview	5
2.2 Basics of Hyperbolic Metamaterials	5
2.2.1 General Linear Optical Properties	5
2.2.2 Definition of Hyperbolic Metamaterials	7
2.2.3 Layered Hyperbolic Metamaterials	10
2.2.4 Material Systems for Hyperbolic Metamaterials	13
2.3 Non-Linear Hyperbolic Metamaterials	13
2.3.1 Non-Linear Optical Properties and Symmetry	13
2.3.2 Deriving Non-linear Properties of Crystals	18
2.3.3 Deriving Non-Linear Properties of Metals	21
2.3.4 Non-linear Effective Medium	27
2.3.5 Second-Order Non-Linear Processes	29
2.3.6 Third-Order Non-linear Processes and Optical Switching	30
2.3.7 Basics of Plasmons and Surface Plasmons	34
2.3.8 Field Enhancement	35
2.4 Computer Optimized Design of Metamaterials	36
2.4.1 Optimization Algorithms	36
2.5 Summary	39
III. Methodology	40
3.1 Chapter Overview	40
3.2 Fabrication with Physical Vapor Deposition	40
3.3 Experimental Verification	44
3.3.1 Fabrication Quality with Microscopy	44
3.3.2 Linear Measurements with Spectral Ellipsometry	45

	Page
3.3.3 Non-Linear Measurements with Z-Scan	50
3.4 Modeling Linear and Non-linear Hyperbolic Metamaterials	52
3.5 Optimizing Hyperbolic Metamaterials	56
3.6 Computational Tests of Optimization Scheme	61
3.7 Summary	66
IV. Initial Test Results	67
4.1 Chapter Overview	67
4.2 Fabrication Results	67
4.3 Linear Measurement Results	68
4.4 Non-linear Measurement Results	75
4.5 Summary	78
V. Final Results	79
5.1 Chapter Overview	79
5.2 Optimization Results	79
5.3 Fabrication Results	83
5.4 Linear Measurement Results	84
5.5 Non-Linear Measurement Results	88
5.6 Measurement-to-Model Comparisons	94
5.7 Summary	100
VI. Conclusion	101
6.1 Overall Summary	101
6.2 Applications of Research	103
6.3 Publications	104
6.4 Recommendations for Future Research	104
Bibliography	106

List of Tables

Table		Page
1	Non-zero Elements of the $\chi^{(2)}$ Tensor.	16
2	Non-zero Elements of the $\chi^{(3)}$ Tensor.	17
3	Unoptimized Test Designs.	43
4	Optimized Designs.	44
5	Comparison of Design, TEM, and Modeled Metal Fractions for each of the Three Different Designs.	71

List of Figures

Figure	Page
1	Diagram of Hyperbolic Isofrequency Surfaces. 8
2	Example of Centrosymmetric Layered Material. 15
3	Example of Non-centrosymmetric Layered Material. 16
4	Generic Hysteresis Curve for Intrinsic Optical Bistability. 31
5	Diagram of Fabrication System. 41
6	Example TEM of a Layered Metamaterial. 45
7	Diagram of the Ellipsometry Process. 47
8	Diagram of Basic Z-scan Setup. 50
9	Electron and Lattice Temperature Plot of an 310 nm ITO Film. 53
10	Electron and Lattice Temperature Plot of an 310 nm ITO Film from source [1]. 54
11	Non-linear Refraction Plot Showing Angle Enhancement. 55
12	Non-linear Refractive Index Plot Showing Angle Enhancement from source [1]. 55
13	Non-linear Refractive Index Plot Showing Angle Enhancement. 56
14	Pareto Plot in Input Space With Results From <i>Lumerical</i> and MATLAB® Schemes. 58
15	Pareto Plot in Input Space With Results From <i>Lumerical</i> and MATLAB® Schemes. 59
16	Refractive Device Pareto Points in Input Space. 62
17	Refractive Device Pareto Points in Output Space. 63
18	Optical Switch Pareto Points in Input Space. 64
19	Optical Switch Pareto Points in Output Space. 65

Figure	Page
20	TEM of Unoptimized Layered ITO/SiO ₂ Metamaterial. 67
21	Complex Refractive Index for the Constituents of the Layered Metamaterial. 68
22	Comparison between Literature Values and Measured Values for ITO. 69
23	Comparison of Model and Experimental Ellipsometric Psi Data for Different Number of Unit Cells. 70
24	Comparison of Model and Experimental Ellipsometric Psi Data for Different Incidence Angles. 70
25	Extracted Linear Anisotropic Optical Properties for ITO/SiO ₂ metamaterial with 0.5 Metal Fraction. 72
26	Comparison of Ellipsometric Ψ Between Drude Model and Measurement for an ITO Film from October 2021. 73
27	Comparison of Ellipsometric Δ Between Drude Model and Measurement for an ITO Film from October 2021. 73
28	Updated Comparison between Literature Values and Different Measured Values for ITO. 74
29	Open-Aperture and Closed-Aperture Z-scans of ITO/SiO ₂ Metamaterial with 0.5 Metal Fraction and 8 Periods. 75
30	Open and Closed Aperture Z-scans of ITO/SiO ₂ Metamaterial for Different Input Powers. 76
31	Average Open-Aperture Z-Scans for Metamaterials Deposited on Silicon Substrate. 77
32	Pareto Front in Input Parameter Space for Optimized Designs. 81
33	Pareto Front in Output Function Space for Optimized Designs. 82
34	TEM image of a Representative Optimized Sample. 83
35	Comparison of Ellipsometric Ψ Between Drude Model and Measurement for an ITO Film from January 2022. 85

Figure	Page
36	Comparison of Ellipsometric Δ Between Drude Model and Measurement for an ITO Film from January 2022. 85
37	Final Comparison between Literature Values and Different Measured Values for ITO. 86
38	Comparison of Ellipsometric Δ Between EMA and Measurement for the Optimized Hyperbolic Metamaterial. 87
39	Comparison of Ellipsometric Δ Between EMA and Measurement for the Optimized Hyperbolic Metamaterial. 87
40	First Open-Aperture Z-scan Results for the Final Six Growths At Zero Degrees Incidence. 88
41	Open-aperture measurements at 1.78 microns for Optimized Samples. 89
42	Closed-aperture Measurements at 1.78 microns for Optimized Samples. 90
43	Open-aperture Measurements at 1.835 microns for Optimized Samples. 91
44	Closed-aperture Measurements at 1.835 microns for Optimized Samples. 91
45	Data and Fit of Fused Silica Substrate Z-scan. 92
46	The relationship of Transmission Enhancement at 45° with Peak Intensity. 94
47	Visual Explanation of the Switching Width and Intensity. 95
48	The Measured and Modeled Switching Width of the Sample, with Measurement Uncertainties. 96
49	The Measured and Modeled Switching Intensity of the Sample, with Measurement Uncertainties. 98

OPTIMIZING OPTICAL SWITCHING OF NON-LINEAR HYPERBOLIC METAMATERIALS

I. Introduction

1.1 General Issue

Non-linear optical devices offer possible advantages in many areas, such as remote sensing, optical communication and computing, and quantum technology. Specifically for optical computing, a highly efficient optical switch for use in optical memory is needed [2]. Current proposed systems have problems with high switching intensities, low switching widths, or large switching times [3]. These problems can be addressed by using designed metamaterials. These metamaterials can be computer optimized using heuristic algorithms, and have a well known fabrication method, physical vapor deposition. This work focuses on a specific type of metamaterial, the hyperbolic metamaterial, that is capable of strongly non-linear behavior, in addition to having fast electron behavior that allows for small switching times [4].

1.2 Relevant Research

Hyperbolic metamaterials have been studied for many years and for many different applications. For overviews of the general field of hyperbolic metamaterials, refer to the reviews [5, 6, 7]. Hyperbolic metamaterials have often been used for radiative emission and absorption control [8, 9, 10, 11, 12]. Many researchers have made hyperbolic metamaterials of graphene [13, 14, 15, 16]. Hyperbolic metamaterials have been used for thermal control [17, 18]. Hyperbolic metamaterials have been applied

in the biosensing field [19]. The ideas of topological photonics have also been applied to hyperbolic metamaterials [20].

Less work has been done with hyperbolic metamaterials in the non-linear regime, but it is a growing field of interest. Non-linear hyperbolic metamaterial sections are found in general hyperbolic reviews [21, 22]. Using non-linear hyperbolic for quantum applications has been discussed [11, 23]. Applications of non-linear hyperbolic metamaterials include filters for hyperlenses [24], optical switches [25, 26, 27, 28, 29], second harmonic generation [30], and waveguides [31].

The field enhancement used in this work has seen some work before. The general concept of field enhancement has been covered [32, 33, 34]. Field enhancement has been achieved in metamaterials for the purpose of high harmonic generation [35].

Lastly, computer optimization and design of metamaterials is one of the fastest growing fields in all of material science. Only a small selection of relevant research will be referenced here. A general look at some heuristic algorithms for metamaterial design is found in [36]. Genetic algorithms have been used for metamaterial design [37, 38, 39], and particle swarm algorithms have been used [40, 41]. Another topic in optimization is inverse design, where the desired properties are chosen beforehand, and a design that fits those properties is found. Techniques such as neural networks [42, 43] and generative machine learning [44, 45] have also been recently used, but require much more computing power. Much more work on neural networks and machine learning for metamaterials is expected over the next few years.

1.3 Research Process

The ultimate objective of the work is to make progress towards an optical switch that can provide improvements over current optical switches. In progress towards this goal, several other objectives will be achieved. These objectives make up the research

plan, which has several aspects to it. The first aspect is creating a model that can represent the behavior of any material that fits the assumptions. A primary goal is the computational speed of this model. For this purpose, a numerical model based on the two-temperature model and the non-linear effective medium is used. For the second part, an optimization scheme can be attached to that model, which would allow for the efficient discovery of optimized designs. The third feature is fabrication, which primarily uses physical vapor deposition. The fourth part is measurement, with both linear and non-linear measurements needed. For the linear measurements, the technique of spectroscopic ellipsometry was used, and for the non-linear measurements, the Z-scan technique was used. The final aspect is an uncertainty analysis, where the results of the measurements will be directly compared to the model.

1.4 Limitations and Challenges

The research methodology is extensive, but there were some limitations to the scope of the work. Firstly, the difficulty in fabricating samples led to only one material system being studied instead of the original three that were planned. This difficulty had several causes: first, the fabrication system went down several times and had to be repaired; second, there were other higher priority users of the fabrication system; and third, public health considerations led to delays from low staffing and supply chain issues. Still, interesting results were obtained with one material system. The amount of optimized samples that could be produced was also limited.

Another limitation was that of computational power, which precluded running the most complex, but most accurate, version of the optimization scheme used in this work. To address this, a simpler version of the optimization scheme was used which was able to run much faster. By correlating some limited results of the more complex scheme to the simpler scheme, and using a full propagated uncertainty analysis of the

measurements, confidence in the optimization results was still achieved.

The last limitation was that of measurement system availability. The Z-scan system had very limited availability for most of the project period, since the advanced high power laser systems broke down frequently. This limited the amount of non-linear measurements that could be done early in the project, but near the end of the project, a new laser system was installed, which had no issues. So this limitation did not impact the measurement of the final designs.

1.5 Document Overview

Chapter II provides the theoretical background, covering extensively linear and non-linear properties of hyperbolic metamaterials. Chapter III describes the methodology of the work, with respect to fabrication, modeling, and measurement. Chapter IV contains the results for the project for the test samples, which were not optimized. Their fabrication results, linear results and non-linear results are presented. Chapter V contains the results of the project for the final optimized samples, starting with the optimized designs, the fabrication results, the linear and non-linear results, and lastly the uncertainty analysis. Chapter VI concludes the work by summarizing it, and offering many possibilities for future work.

II. Theoretical Background

2.1 Chapter Overview

In this chapter, the basics of hyperbolic metamaterials are discussed. After, an understanding of non-linear hyperbolic metamaterials is given, both their properties and applications. In this section, the theory of the two temperature model and the non-linear effective medium are covered. Then, the basics of plasmonics, specifically for field enhancement, is reviewed. Lastly, an overview of computer-optimized design for metamaterials, with a focus on genetic algorithms, is presented.

2.2 Basics of Hyperbolic Metamaterials

2.2.1 General Linear Optical Properties.

First, the general form of the linear optical properties of a material is needed. The electromagnetic field's interaction with any material is governed by certain macroscopic properties, both its permittivity, ε , and its permeability, μ . For this work, assume no magnetic interaction, thus $\mu = \mu_0$. Note that the permittivity defines the dielectric properties of the material and may be complex in general. For isotropic materials, there is only one value for ε , but generally, the dielectric properties of every material can be represented by a dielectric tensor, which will be written as

$$\overleftrightarrow{\varepsilon} = \begin{bmatrix} \varepsilon_{xx} & \varepsilon_{xy} & \varepsilon_{xz} \\ \varepsilon_{yx} & \varepsilon_{yy} & \varepsilon_{yz} \\ \varepsilon_{zx} & \varepsilon_{zy} & \varepsilon_{zz} \end{bmatrix}, \quad (1)$$

where x, y, z define an arbitrary rectangular coordinate system.

Theoretically, each of these directional permittivities may be different, which leads to a large number of variables in any material characterization. However, the num-

ber of variables can be reduced by applying symmetry to the material, with more symmetry leading to a material with fewer variables to determine. There are several categories of anisotropic materials that are grouped by their symmetries, and two important categories are uniaxial and biaxial materials. Uniaxial materials have a single axis that governs the anisotropy, which is known as the optic axis of the material. Rotating around this axis does not change the behavior of the material, so this is a symmetry that reduces the number of variables to characterize. Assuming the optic axis is aligned with the z-axis, a general dielectric tensor for uniaxial materials is

$$\overleftrightarrow{\varepsilon} = \begin{bmatrix} \varepsilon_t & 0 & 0 \\ 0 & \varepsilon_t & 0 \\ 0 & 0 & \varepsilon_z \end{bmatrix}, \quad (2)$$

where ε_t is in the directions perpendicular to optic axis, while ε_z is in the direction of the optic axis. Note that the coordinate system in which the dielectric tensor is diagonal may not align with the laboratory coordinate system. However, for uniaxial materials, the laboratory coordinate system may always be rotated into the diagonal system. Another convention uses ε_O instead of ε_t to represent the “ordinary” transmission which is not affected by the anisotropy, and uses ε_E instead of ε_z to represent the “extraordinary” transmission, which is affected by the anisotropy. In any case, using symmetry, there are now only two variables needed rather than nine needed in the general case to characterize the material.

The above discussion uses the permittivity to define the optical properties, but there are other ways to quantify the optical properties. One common way is the index of refraction. It was stated before that the permittivity can be complex in general, so the index of refraction can also be complex. If so, the real part of the index of refraction is called n , while the imaginary part is called k . The imaginary part of the

index of refraction is related to the absorption of the material. The equations that convert from permittivity to refractive index are in Eqs. (3) and (4), noting ε_1 is the real component of the permittivity and ε_2 is the imaginary component.

$$n = \sqrt{\frac{|\varepsilon| + \varepsilon_1}{2}}, \quad (3)$$

$$k = \sqrt{\frac{|\varepsilon| - \varepsilon_1}{2}}, \quad (4)$$

where $|\varepsilon| = \sqrt{\varepsilon_1^2 + \varepsilon_2^2}$. Another way to describe the optical properties is the electric susceptibility. The electric susceptibility is defined as the proportionality constant that relates an electric field \mathbf{E} to an induced polarization density \mathbf{P} , with an equation of the form of

$$\mathbf{P} = \varepsilon_0 \chi_E \mathbf{E}, \quad (5)$$

where ε_0 is the vacuum permittivity and χ_E is the electric susceptibility. There is also a simple relation between permittivity and the susceptibility, which is

$$\chi_E = \varepsilon - 1 \quad (6)$$

Now that an understanding of the general optical properties of materials is achieved, hyperbolic metamaterials can be looked at specifically.

2.2.2 Definition of Hyperbolic Metamaterials.

Before defining hyperbolic metamaterials, a definition of metamaterials is needed. There is not a unique and universally accepted definition [46], but in this work, the definition of metamaterials is materials with some structure smaller than the wavelength of interest, that leads to special effective properties of the metamaterial. For hyperbolic metamaterials, the effective property is hyperbolic dispersion. All real ma-

materials have some level of dispersion, which is simply the change in optical properties, such as refractive index, with wavelength/frequency. The dispersion relation is the equation that describes this relationship. The dispersion relation is usually put in terms of wavenumber k and angular frequency ω . In a vacuum, the dispersion relation is $\omega = ck$, where c is the speed of light. This is a linear dispersion relation, which means in 3D, the isofrequency surfaces are spherical, described by $k_x^2 + k_y^2 + k_z^2 = \frac{\omega^2}{c^2}$, where k_x represents the wavenumber in x direction and so on.

If instead of an isotropic medium like a vacuum, an anisotropic uniaxial medium is used, the isofrequency surfaces are described by

$$\frac{k_x^2 + k_y^2}{\varepsilon_O} + \frac{k_z^2}{\varepsilon_E} = \frac{\omega^2}{c^2} \quad (7)$$

This equation would still describe a sphere if $\varepsilon_E = \varepsilon_O$, and if they are slightly different, it will be an ellipsoid. However, if there is very strong anisotropic behavior, to the point where $\varepsilon_E \cdot \varepsilon_O < 0$, then the equation describes an hyperboloid. This condition occurs when either $\varepsilon_E < 0$ and $\varepsilon_O > 0$ or $\varepsilon_E > 0$ and $\varepsilon_O < 0$. The first case is referred to as a type I hyperbolic metamaterial and the second case is a type II hyperbolic metamaterial. Therefore it can be seen that the name hyperbolic metamaterial comes from the shape of the isofrequency surface. This can be seen visually in Figure 1.

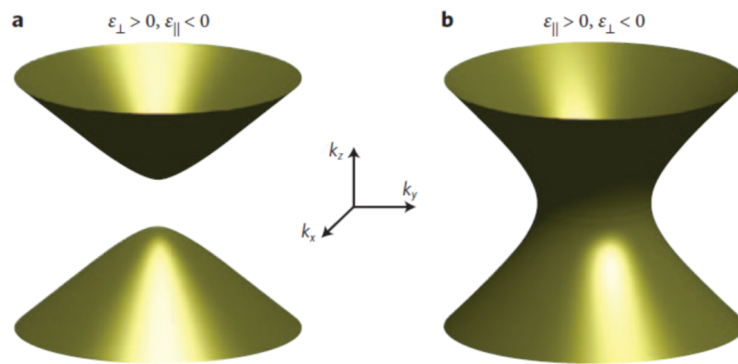


Figure 1. Diagram of Hyperbolic Isofrequency Surfaces. The hyperboloid shape of the surface is clearly shown. Part a. of the figure shows a type I hyperbolic metamaterial, while part b. shows a type II hyperbolic metamaterial. Adapted from source [6].

The consequences of this special dispersion are profound. One consequence is that density of states is changed from natural materials. The density of states is defined as the number of states available for each level of energy, and is represented in terms of a probability density function. There are many different forms of density of states, but in this case, there is a photonic density of states (PDOS). One way to find the PDOS is to look at the volume enclosed between two isofrequency surfaces that are separated by some frequency $d\omega$. From Figure 1, it can be seen that the volume enclosed by an arbitrary hyperboloid is infinite, since the “cones” of the hyperboloid continue to positive and negative infinity. Therefore the volume between two hyperboloids must also be unbounded. So theoretically, hyperbolic metamaterials should have an infinite PDOS. In reality, there is not actually an infinite PDOS, but it can still be much higher than natural materials, up to an order of magnitude increase [7].

What is the use for this large PDOS? Fermi’s golden rule states that the decay rate of excited states is proportional to the density of states. Therefore a larger PDOS should correspond to increased emission rates. Moreover, the exact value of the PDOS should be capable of being adjusted by changing the properties of the metamaterial, which makes effective emission engineering a possibility.

Another feature that is not unique to hyperbolic metamaterials, but does relate to them, is the epsilon-near-zero (ENZ) point. The definition of an ENZ point is simply the wavelength/frequency where the permittivity is near to zero. Since hyperbolic behavior occurs when one direction has permittivity less than zero and other has permittivity greater than zero, ENZ points naturally occur at the transition from normal (elliptical) dispersion to hyperbolic dispersion or vice versa. At this point, there are several useful properties. First, note that in this section only linear effects are considered. In a later section, non-linear effects will be discussed, but it is clear that for ENZ points, the linear effects will be small. This allows the non-linear effects

to be more easily detected. Another property is that the phase advance of the incident light is zero at the ENZ point. Generally, there is a phase shift when interacting with any natural material, which can lead to constructive or destructive interference, which impacts efficiency. ENZ points can remove this complication.

2.2.3 Layered Hyperbolic Metamaterials.

There are many ways to achieve this hyperbolic dispersion in metamaterials, including metal wire grids in a dielectric medium [6], graphene sheets [15], and alternating layers of dielectric and metal. Note that all the dimensions must be smaller than the wavelength of interest. For example, for metamaterials in the visible light regime, the dimensions should be less than 300 nanometers. In this work, the method of alternating layers of dielectric and metal is the main focus.

The most common method for analysis of layered hyperbolic metamaterials is the Maxwell-Garnett effective medium approximation (EMA). The derivation of this approximation is fairly simple, since only electrostatic concepts are used. This derivation follows source [5]. For the derivation, the fact that $\mathbf{D} = \varepsilon\mathbf{E}$ is needed, where \mathbf{D} is the electric displacement field. First, consider the component parallel to the layered interfaces, which is the ordinary direction. It is known from electrostatics that the tangential component of the electric field is continuous at an interface, which implies that $\mathbf{E}^O = \mathbf{E}_m^O = \mathbf{E}_d^O$. From electrostatics, the displacement field in the ordinary direction, \mathbf{D}^O , can also be found as an average of the displacement field in the metal and dielectric regions. Thus,

$$\mathbf{D}^O = \rho\mathbf{D}_m^O + (1 - \rho)\mathbf{D}_d^O, \quad (8)$$

where ρ is the volume fraction of the metal, which depends on the layer thicknesses. Now using the relationship of \mathbf{D} to \mathbf{E} ,

$$\varepsilon_O \mathbf{E}^O = \rho \varepsilon_m \mathbf{E}_m^O + (1 - \rho) \varepsilon_d \mathbf{E}_d^O. \quad (9)$$

Canceling out the electric fields,

$$\varepsilon_O = \rho \varepsilon_m + (1 - \rho) \varepsilon_d. \quad (10)$$

Thus the permittivity in the ordinary direction of the effective medium can be found from the properties of the layers.

Now consider the direction perpendicular to interfaces, which is the extraordinary direction. It is known from electrostatics that the perpendicular component of the displacement field is continuous at an interface, which implies that $\mathbf{D}^E = \mathbf{D}_m^E = \mathbf{D}_d^E$. From electrostatics, the displacement field in the extraordinary direction, \mathbf{E}^E , can also be found as an average of the electric field in the metal and dielectric regions. Thus,

$$\mathbf{E}^E = \rho \mathbf{E}_m^E + (1 - \rho) \mathbf{E}_d^E, \quad (11)$$

where ρ is the volume fraction of the metal, which depends on the layer thicknesses. Now using the relationship of \mathbf{D} to \mathbf{E} ,

$$\frac{1}{\varepsilon_E} \mathbf{D}^E = \frac{\rho}{\varepsilon_m} \mathbf{D}_m^E + \frac{(1 - \rho)}{\varepsilon_d} \mathbf{D}_d^E. \quad (12)$$

Canceling out the displacement fields,

$$\frac{1}{\varepsilon_E} = \frac{\rho}{\varepsilon_m} + \frac{(1 - \rho)}{\varepsilon_d}. \quad (13)$$

Thus the permittivity in the extraordinary direction of the effective medium can be found from the properties of the layers. This formulation has been shown to be very

useful when plasmonic resonances are not a large factor [6]. A later section will consider plasmonic resonances. Note that the results received here are actually a specific case of the general Maxwell-Garnett EMA formula,

$$\varepsilon = \varepsilon_h \frac{\varepsilon_h + [v_p(1 - \rho) + \rho](\varepsilon_i - \varepsilon_h)}{\varepsilon_h + v_p(1 - \rho)(\varepsilon_i - \varepsilon_h)} \quad (14)$$

where v_p is the polarization factor, ρ is the inclusion fill fraction, ε_h is the host permittivity, and ε_i is the inclusion permittivity. If ρ is identified as the metal fraction, ε_h as ε_d , and ε_i as ε_m , then equations (10) and (13) can be recovered when v_p is set to 0 or 1, respectively. This formulation is important to understand, since some software uses the more general formulation.

The effective medium methods give the effective linear optical properties of the materials, and from this, it would be possible to use the Fresnel equations to calculate the reflection and transmission. However, there is another method that can directly calculate the reflection and transmission of any layered material without reference to an effective medium, and it is also used in this work. The method is known as the transfer matrix method. The field components on one side of an interface can be related to the field components on the other side by their Fresnel coefficients, while the field propagation through a material can be represented by a phase change and possibly a loss. By representing the input field as a 2 by 1 matrix, with “right-moving” and “left-moving” components, where those components represent the fields moving in the direction of the input field and field moving in the opposite direction. Also, the effect of the interface or the layer propagation can be represented by a 2 by 2 matrix. Therefore, it is possible to apply these matrices in sequence to determine how the field changes with the material. All of the matrices that represent the interfaces and layer thicknesses can be multiplied together to get the total transfer matrix of the system. When this is multiplied by the input field, the reflected field and transmitted

field will be received. Then the reflectance and transmittance could be found from those fields.

2.2.4 Material Systems for Hyperbolic Metamaterials.

There have been quite a few different material systems that have been used for hyperbolic metamaterials based on the multilayer structure, so reviewing their capabilities is beneficial. Some examples of material systems are Ag/Al₂O₃, Ag/LiF, Ag/TiO₂, Ag/Ge, Au/Al₂O₃ and Au/TiO₂ [6]. So it can be seen that silver and gold are the most common metals used in hyperbolic metamaterials, while the possible dielectrics vary more. However, they have a limited range of effectivity, since these materials become hyperbolic in the low visible wavelengths, and the losses become too high to be effective in long visible and near IR wavelengths. For these wavelengths, alternate materials are often used as the metal, such as transition metal nitrides, or conducting oxides. Some examples are titanium nitride or indium tin oxide [7]. In this work, the focus was on ITO. For even longer wavelengths, an all-dielectric structure with specialized high-index dielectrics in place of the metal is sometimes used. One example of this specialized dielectric is silicon carbide [6]. Another way is to use doped semiconductors as the metal, since they have metal-like behavior in the mid-IR range [11].

2.3 Non-Linear Hyperbolic Metamaterials

2.3.1 Non-Linear Optical Properties and Symmetry.

The discussion in the previous section on hyperbolic metamaterials only dealt with the linear optical properties. Using only linear properties implies that there is a purely linear relationship between polarization and the strength of the applied field. This case was seen in Eq. 5 in the last section. For most natural materials,

this holds, however, for some natural materials and many metamaterials, there is a non-linear relationship between the polarization and the strength of the applied field. This relationship can be described by the non-linear optical properties. Therefore the more general form of Eq. 5 is

$$\mathbf{P} = \varepsilon_0 [\chi^{(1)}\mathbf{E} + \chi^{(2)}\mathbf{E}^2 + \chi^{(3)}\mathbf{E}^3 + \dots], \quad (15)$$

where the values $\chi^{(2)}$ and $\chi^{(3)}$ are the second and third order electric susceptibilities. Note that $\chi^{(1)}$ is the linear susceptibility and is a matrix for the hyperbolic metamaterials. Another way to represent a matrix is a rank-two tensor. Therefore $\chi^{(2)}$ and $\chi^{(3)}$ are actually rank-three and rank-four tensors, respectively, rather than matrices. This makes representation of the properties much more complicated, and it also means that there are more variables to consider when determining the properties. Therefore, symmetry will become even more important, so next, the application of symmetry for the non-linear properties is dealt with to simplify the susceptibility tensors.

In the last section, it was seen that hyperbolic metamaterials have uniaxial anisotropic behavior by definition. This implies a certain level of symmetry that reduces the number of independent variables in the dielectric tensor from nine to two. This same idea can be applied to the higher rank tensors that describe the second-order and third-order non-linear optical properties.

However, simply saying the materials are uniaxial does not give enough information about the symmetry of these materials to determine the form of the second-order dielectric tensor. Therefore it is necessary to consider real symmetry operations. It is a known fact of non-linear optics that centrosymmetric systems do not have a second-order non-linear response [47]. To see this, note that $\mathbf{P}^{(2)} = \varepsilon_0\chi^{(2)}\mathbf{E}^2$. Now assume the applied field is negative, then the polarization will also change sign. This is because

centrosymmetry is inversion symmetry. So it is also true that $-\mathbf{P}^{(2)} = \varepsilon_0\chi^{(2)}(-\mathbf{E})^2$. This implies that $\mathbf{P}^{(2)} = -\mathbf{P}^{(2)}$, which can only be true if $\mathbf{P}^{(2)} = 0$. Therefore inversion symmetry is the most critical to check for when designing hyperbolic metamaterials.

To label the individual symmetries and symmetry groups, Hermann-Mauguin notation, otherwise known as international notation, is used. Figure 2 illustrates one possible design of the multilayer hyperbolic metamaterials. Note that the diagram is not to scale, so one could think of this design as a small patch of volume of the metamaterial, since the horizontal extent of the metamaterial will necessarily be much larger than the vertical extent. From this, the top face is assumed to be a square, and no substrate is considered.

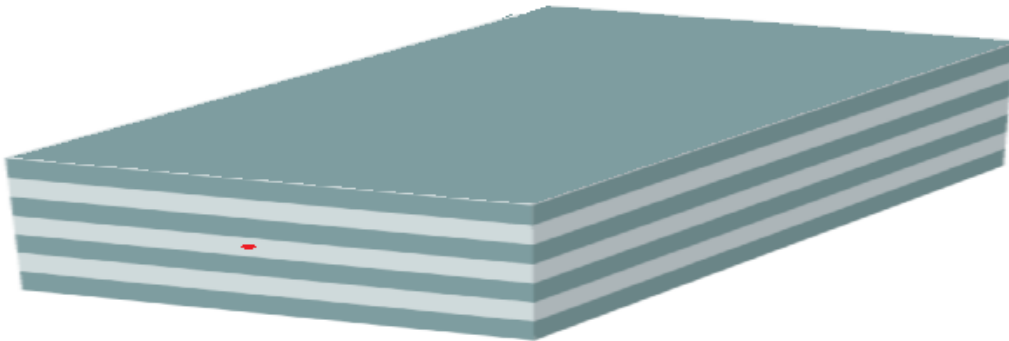


Figure 2. Example of Centrosymmetric Layered Material. The dark layer can be thought of as the metal, with the lighter layer as the dielectric. The red dot signifies the center.

Now the symmetries present in that design are described. Clearly, the z -axis, which is normal to the top surface has a 4-fold rotation axis. There are also three mirror planes in each of the xy , xz , and yz planes. The only point group with all these elements is called $4/mmm$. The $4/m$ represents the 4 fold rotation axis in the z direction, and the mirror plane perpendicular to it. The two other m elements represent the other two mirror planes. This point group is centrosymmetric, and source [47] verifies that this point group leads to zero second-order behavior. Now consider a different design shown in Figure 3.

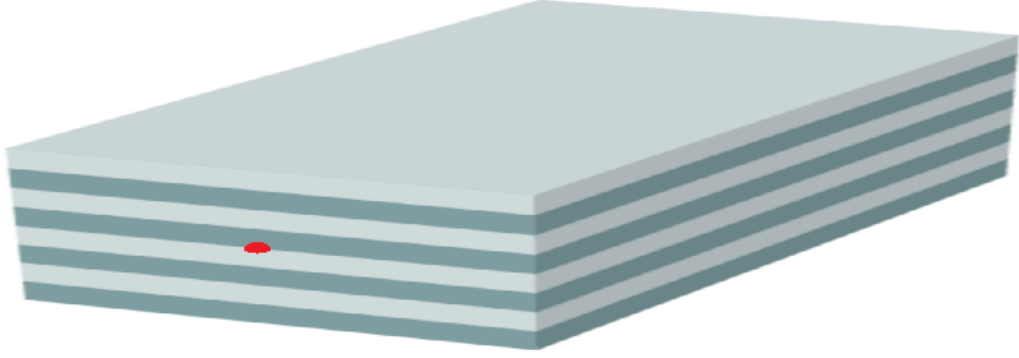


Figure 3. Example of Non-centrosymmetric Layered Material. The dark layer can be thought of as the metal, with the lighter layer as the dielectric. The red dot signifies the center.

This design differs only in that there is no mirror plane parallel with the xy -plane, perpendicular to the z -axis. Thus instead of the operation $4/m$, it is just 4, the 4-fold rotation. The other two mirror planes still exist, so the point group is now $4mm$. There is no longer full inversion symmetry, thus there should be second-order behavior. There are up to 81 independent elements of the rank-3 tensor for the second-order linear effects, but using the point group $4mm$, Table 1, adapted from source [47] gives the seven remaining non-zero elements and shows that there are only four independent elements. Note that the elements of the second order dielectric tensor are described by three indices, so the table actually lists the indices of the elements that are non-zero.

Table 1. Non-zero Elements of the $\chi^{(2)}$ Tensor. There are seven non-zero elements and four independent elements.

$xzx = yzy$
$xxz = yyz$
$zxx = zyy$
zzz

This table makes sense in terms of what is known about hyperbolic metamateri-

als. Theoretically, there is no difference between the x and y direction in a uniaxial material, since they both are “ordinary,” so it makes sense that these elements are related. One more check is that the point groups found do correspond to the uniaxial behavior in the linear regime. Since the point groups are already found, tables from source [47] can be used to determine the independent elements of the third order susceptibility tensor. Table 2 shows the elements, and note that four indices are needed to describe an element.

Table 2. Non-zero Elements of the $\chi^{(3)}$ Tensor. There are 21 non-zero elements and 11 independent elements.

$xxxx = yyyy$
$yyzz = xxzz$
$zzyy = zzxx$
$zyyz = zxxz$
$yzzy = xzzx$
$yzyz = xzzx$
$zyzy = zxxz$
$xyxy = yxyx$
$xyxy = yxyx$
$xyyx = yxyx$
$zzzz$

Another note to consider in terms of symmetry is that even with the centrosymmetric design, there will still be some second-order behavior, because at the surface and other interfaces, the hyperbolic metamaterial will be locally non-centrosymmetric. However, the contribution from these sources to the second-order non-linearity will be small compared to a fully non-centrosymmetric material, so it can be assumed that centrosymmetric materials have no second-order behavior. Now that the symmetry

of the hyperbolic metamaterials is known, the next step is to calculate the optical properties.

2.3.2 Deriving Non-linear Properties of Crystals.

There is a known approximation for finding the non-linear properties from the linear properties which is known as Miller's rule. It gives insight into the origin of non-linear properties, so the derivation is given here. To derive Miller's rule, from the derivation in [47], consider the Lorentz oscillator model [48]. The classic Lorentz oscillator model represents an atom as a harmonic oscillator, and is effective in modeling linear properties. For Miller's rule, this idea is extended by treating the atom as an anharmonic oscillator. Note that for the derivation, the material is assumed to be non-centrosymmetric, as discussed above. Assume an anharmonic oscillator with restoring force,

$$\mathbf{F}_{\text{restoring}} = -m\omega_0^2\mathbf{x} - m\alpha\mathbf{x}^2, \quad (16)$$

where the first term on the right-hand side is well known harmonic oscillator term, with m as the mass, \mathbf{x} as the position, and ω_0 as the natural frequency. The second term is the anharmonic term, where α is the anharmonic coefficient. Note that the second term is proportional to the square of the displacement, so this is a second-order non-linear system. Assume the applied field is a mix of two frequencies, so that $\mathbf{E} = E_1e^{-i\omega_1t} + E_2e^{-i\omega_2t}$. There does not exist a general solution to this system, so a perturbation method is used, where λ is the strength of the perturbation. Then the equation of motion becomes

$$\frac{d^2\mathbf{x}}{dt^2} + \omega_0\mathbf{x} + \alpha\mathbf{x}^2 = -\lambda\frac{q}{m}\mathbf{E}, \quad (17)$$

where q is the electron charge and m is the electron mass. Consider a solution to this equation of the form of

$$\mathbf{x} = \lambda \mathbf{x}^{(1)} + \lambda^2 \mathbf{x}^{(2)} + \lambda^3 \mathbf{x}^{(3)} + \dots \quad (18)$$

Here assume that the perturbation is small enough that only the first two terms are significant. So plugging the first two terms back into the equation of motion gives

$$\frac{d^2}{dt^2} [\lambda \mathbf{x}^{(1)} + \lambda^2 \mathbf{x}^{(2)}] + \omega_0 [\lambda \mathbf{x}^{(1)} + \lambda^2 \mathbf{x}^{(2)}] + \alpha [\lambda \mathbf{x}^{(1)} + \lambda^2 \mathbf{x}^{(2)}]^2 = -\lambda \frac{q}{m} \mathbf{E}. \quad (19)$$

For this to work as a solution for any value of λ , all the terms with a certain power of λ must satisfy the equation of motion separately. So there are two equations, (20) and (21), for λ and λ^2 . The terms proportional to λ^3 or higher are assumed to be negligible.

$$\frac{d^2}{dt^2} \mathbf{x}^{(1)} + \omega_0 \mathbf{x}^{(1)} = -\frac{q}{m} \mathbf{E} \quad (20)$$

$$\frac{d^2}{dt^2} \mathbf{x}^{(2)} + \omega_0 \mathbf{x}^{(2)} + \alpha [\mathbf{x}^{(1)}]^2 = 0 \quad (21)$$

Here it can be seen that the first equation is simply the formula for a harmonic Lorentz oscillator, which has a known steady state solution for the given applied field,

$$\mathbf{x}^{(1)} = x^{(1)}(\omega_1) e^{-i\omega_1 t} + x^{(1)}(\omega_2) e^{-i\omega_2 t}, \quad (22)$$

where the amplitudes have the form $x^{(1)}(\omega_j) = -\frac{q}{m} \frac{E_j}{\omega_0^2 - \omega_j^2}$. Now this first order solution is substituted back into Eq. (21), which can now be solved for $\mathbf{x}^{(2)}$. In an arbitrary second order process, where ω_3 is some sum or difference of ω_1 and ω_2 , the amplitude

of the solution is

$$\mathbf{x}^{(2)}(\omega_3) = -\left(\frac{q}{m}\right)^2 \frac{2\alpha E_1 E_2}{(\omega_0^2 - \omega_3^2)(\omega_0^2 - \omega_1^2)(\omega_0^2 - \omega_2^2)}. \quad (23)$$

Now the goal is to represent this solution in terms of susceptibility. It is known that the linear contribution to the polarization is given by

$$P^{(1)}(\omega_j) = -Nqx^{(1)}(\omega_j), \quad (24)$$

where N is the number density of atoms. Then using the relationship of polarization to susceptibility and the field that is known by Eq. (15), and the definition of the linear amplitude, the equation for the linear susceptibility is

$$\chi^{(1)}(\omega_j) = \frac{Nq^2}{\varepsilon_0 m(\omega_0^2 - \omega_j^2)}. \quad (25)$$

Doing the same process for the second order non-linear susceptibility, the equation is

$$\chi^{(2)}(\omega_3, \omega_1, \omega_2) = \frac{Nq^3\alpha}{\varepsilon_0 m^2(\omega_0^2 - \omega_3^2)(\omega_0^2 - \omega_1^2)(\omega_0^2 - \omega_2^2)}. \quad (26)$$

Now, Eq. (25) and (26) can be combined to write the second-order susceptibility in terms of the first order,

$$\chi^{(2)}(\omega_3; \omega_1; \omega_2) = \frac{\varepsilon_0^2 m \alpha}{N^2 q^3} \chi^{(1)}(\omega_3) \chi^{(1)}(\omega_1) \chi^{(1)}(\omega_2). \quad (27)$$

Thus the goal of representing the non-linear properties in terms of the linear properties has been achieved. However, the value of α needs to be determined in order to actually use this formula practically. To that end, what Miller actually described when he formulated Miller's rule was the observation that the ratio $\chi^{(2)}/\chi^{(1)}(\omega_3)\chi^{(1)}(\omega_1)\chi^{(1)}(\omega_2)$ was nearly constant for all materials he observed. This implies that the coefficient

$\varepsilon_0^2 m \alpha / N^2 q^3$ is nearly constant. This actually makes sense, since q , m , and ε_0 are physical constants, and for solids, the atomic number density N does not vary much from 10^{22} particles/cm³. The non-linear coefficient α is nearly constant, since the expectation is that the linear and non-linear contributions to the restoring force (Eq. (15)) would be equal at approximately the size of the atom. At that distance, say $d = 10$ angstroms, $m\omega_0^2 d = m\alpha d^2$, thus $\alpha = \frac{\omega^2}{d}$. A very similar derivation to the above can be done for the third order non-linear susceptibility, with the result,

$$\chi^{(3)}(\omega_4; \omega_1; \omega_2; \omega_3) = \frac{\varepsilon_0^3 m \beta}{N^3 q^4} \chi^{(1)}(\omega_4) \chi^{(1)}(\omega_1) \chi^{(1)}(\omega_2) \chi^{(1)}(\omega_3), \quad (28)$$

where β is constant similar to α , so $\beta = \frac{\omega^2}{d^2}$. The problem with this equation is that it has only been shown to be accurate for ionic crystals and certain glasses, while there have been demonstrated problems when using it with plasmonic materials, such as metals. Therefore a different method is required to understand the non-linear optical response of metals.

2.3.3 Deriving Non-Linear Properties of Metals.

There are several ways to understand the non-linear response in metal, but one important factor to keep in mind is that for almost all non-linear applications, the source is a high power pulsed laser, rather than a “standard” continuous wave laser. In this scenario, the most common way to model the response of a metal is called the two temperature model. The differential equations that describe the simplest version of the model are [49]

$$C_e \frac{\partial T_e(t)}{\partial t} = -G(T_e - T_l) + P(t), \quad (29)$$

$$C_l \frac{\partial T_l(t)}{\partial t} = G(T_e - T_l), \quad (30)$$

where C_e is the electron heat capacity, G is the electron phonon coupling constant, $P(t)$ is the source term, and C_l is the lattice heat capacity. The simplest way to represent the source is a Gaussian pulse with a specified energy and pulse width. There are many other ways to make this model more accurate, such as accounting for conduction in the lattice, ballistic movement of electrons, and heat transfer to the environment. Now solving this system of differential equations numerically will give $T_e(t)$ and $T_l(t)$, a time-resolved electron temperature and lattice temperature. This simple model does not account for any interfaces in the material, but they could be accounted in a more complicated formulation. A more complicated version that includes heat conduction and the effects of a substrate is defined by the system of differential equations [50],

$$C_e \frac{\partial T_e(z, t)}{\partial t} = k_e \nabla^2 T_e - G(T_e - T_l) + P(t), \quad (31)$$

$$C_l \frac{\partial T_l(z, t)}{\partial t} = k_l \nabla^2 T_l + G(T_e - T_l) + G_2(T_l - T_a), \quad (32)$$

$$C_s \frac{\partial T_s(z, t)}{\partial t} = k_s \nabla^2 T_s + G_3(T_s - T_a), \quad (33)$$

where the subscript e refers to the electrons, l refers to the lattice, s refers to the substrate, a refers to the ambient environment; k represents the thermal conductivity, and G_2 or G_3 represent the coupling of the lattice or the substrate to the ambient environment. There are also boundary conditions that need to be applied to ensure correct transfer of heat to the lattice. These boundary conditions at the metal-substrate boundary are

$$-k_e \frac{\partial T_e}{\partial z} = C_{es}(T_e - T_s), \quad (34)$$

$$-k_l \frac{\partial T_l}{\partial z} = C_{ls}(T_l - T_s), \quad (35)$$

$$-k_s \frac{\partial T_s}{\partial z} = C_{es}(T_e - T_s) + C_{ls}(T_l - T_s), \quad (36)$$

where C_{es}, C_{ls} are the interface conductivities. So solving this model would require values for the interface conductivities and the ambient coupling constants, which are difficult to find for metals other than gold or silver. However, they could be theoretically be measured. This expanded model has been tested for gold and silver, so it should work for other metals, but the expanded model was not ultimately used in this work due to the difficulty of determining all the needed factors. Instead, a different two temperature formulation known as the delayed two temperature model from [1] was used,

$$C_e \frac{\partial T_e(t)}{\partial t} = -G(T_e - T_l) + \frac{N}{2\tau_{ee}}, \quad (37)$$

$$C_l \frac{\partial T_l(t)}{\partial t} = G(T_e - T_l) + \frac{N}{2\tau_{ep}}, \quad (38)$$

$$N \frac{\partial N(t)}{\partial t} = -\frac{N}{2\tau_{ee}} - \frac{N}{2\tau_{ep}} + P(t), \quad (39)$$

where N is the non-thermal energy density stored in the electrons, τ_{ee} is the electron-electron relaxation time, τ_{ep} is the electron-phonon relaxation time, and all other variables are defined the same way as the other two-temperature model formulations. This is referred to as the delayed two-temperature model since the input power is

not put directly into the electron temperature equation, but is rather transferred to both the electrons and lattice over time through the relaxation times. This is a more realistic depiction of the physics of the scenario, but it does require more parameters to be calculated. Next, the process of the deriving each of the parameters will be discussed.

First, the electron-phonon coupling constant G is defined as

$$G = 0.562n_e \frac{k_B^2 \Theta_D^2 v_F}{L_f T_l \epsilon_F} \quad (40)$$

where n_e is the free electron density, k_B is Boltzmann's constant, Θ_D is the Debye temperature, v_F is the Fermi velocity, L_f is the mean free path, and ϵ_F is the Fermi energy. All of these values can be found for ITO from various sources [1]. First, n_e is set to 10^{27} electrons/m³. Next, Θ_D equals 1000 K, and L_f is 8.3 nm. Lastly, the Fermi velocity is $v_F = 1 * 10^6$ m/s and the Fermi energy is $\epsilon_F = 1$ eV.

Next, the relaxation times are needed. First, the electron-electron relaxation time is defined as

$$\tau_{ee} = C \left\{ \frac{\omega^2}{4\pi^2 \omega_p} \left[1 + \left(\frac{2\pi k_B T_e}{\hbar \omega} \right)^2 \right] \right\}^{-1}, \quad (41)$$

where ω is the frequency, ω_p is the plasma frequency from the Drude model at room temperature, and C is a scaling constant that is used to maintain the physical relationship that $\gamma = \frac{1}{\tau_{ee}} + \frac{1}{\tau_{ep}}$, where γ is the Drude damping factor at room temperature. The Drude model parameters are ω_p and γ , and they are defined differently at an elevated electron temperature than at room temperature, which will be discussed later. Now the electron phonon relaxation time is

$$\tau_{ep} = 2 \frac{C_e}{G}, \quad (42)$$

where C_e is the electron heat capacity. That quantity C_e is defined as

$$C_e = \frac{3\pi^2 n_e k_b T_e}{\sqrt{36T_F^2 + 4\pi^4 T_e^2}}, \quad (43)$$

where T_F is the Fermi temperature and all other parameters have been defined above. For ITO, the Fermi temperature is about 10,000 K. The lattice heat capacity C_l is treated as a constant, and for ITO, the value $2.6 * 10^6$ J/(m³*K) is used. Next, the equation for the absorbed power density $P(t)$, which is what provides the energy to the system.

$$P(t) = (1 - R - T)I_0\alpha \exp \left[-2 \left(\frac{t}{t_p} \right)^2 \right], \quad (44)$$

where R is the reflectance, T is the transmittance, I_0 is input intensity in units of W/m^2 , α is the linear absorption coefficient in units of m^{-1} , t_p is the pulse duration in seconds for its full width half maximum value, and t is the time. With all those parameters defined for ITO, the time-dependent electron temperature can be determined by solving the system of differential equations. The next step is to use the electron temperature to calculate the non-linear properties. To do this, the free electron model of metals can be used. First, the electron temperature is directly related to the chemical potential μ (also called the Fermi level) by the equation

$$\mu(T_e) \approx \epsilon_F \left[1 - \frac{\pi^2}{12} \left(\frac{T_e}{T_F} \right)^2 \right]. \quad (45)$$

Note this formula is only valid when $T_e \ll T_F$, since this comes from the Sommerfeld expansion representation of the integral of the Fermi-Dirac distribution, which is what applies to electrons. More terms of this expansion could be included, but are not necessary for theory used in this work. Since T_e rises with input intensity, this puts an effective cap on the intensity that can be accurately modeled. However, that intensity cap is high enough to still see strong non-linear behavior. After obtaining

the elevated chemical potential, the next step is to calculate the resultant change in plasma frequency. Then with the elevated plasma frequency, it is possible to find the modified complex permittivity using the Drude model,

$$\varepsilon_{mod} = \varepsilon_{\infty} - \frac{\omega_{p_{mod}}^2}{\omega^2 + i\omega\gamma_{mod}}, \quad (46)$$

where ε_{∞} , $\omega_{p_{mod}}$, and γ_{mod} are the Drude model parameters at the elevated temperature. Then using equations (47) and (48), a refractive index n_{mod} and absorption coefficient α_{mod} can be calculated. Therefore it is possible to calculate the effective nonlinear refractive index n_2 and nonlinear absorption coefficient β

$$n_2 = \frac{n_{mod} - n_0}{I_0}, \quad (47)$$

$$\beta = \frac{\alpha_{mod} - \alpha_0}{I_0}, \quad (48)$$

where I_0 is the input intensity, n_0 and α_0 are the linear properties, and n_{mod} and α_{mod} are the electron-temperature-based values. This entire process can be repeated at any wavelength of interest in order to calculate spectral non-linear properties.

Physically, this theory describes the origin of the effective non-linear response. The samples in this work are designed to be linearly transmissive, so every metal layer in an HMM should be exposed to the high energy from the input source. This energy excites electrons in those layers, creating a temporary change in the electron density. These electrons thermalize (or equilibrate) amongst themselves during the electron-electron relaxation time. By the Drude free electron model, this changes the properties of the material, which gives an effective non-linear response. When applying this energy, the isofrequency surface will be warped in the direction of application, either bending outward or inward, depending on the wavelength and base material. Thus, all of these effects could be considered in frequency space rather than the permittivity space on

which this work focuses.

2.3.4 Non-linear Effective Medium.

For linear optical properties of metamaterials, a common approach is that of effective medium theory as in discussed in section 2.2.3. As discussed there, in the linear regime, a specific formulation of the Maxwell-Garnett EMA is used for layered hyperbolic metamaterials. The theory behind the Maxwell-Garnett EMA has no inherent reason why it should not hold for the non-linear formulation as well. The derivation for the parallel (TM) component with respect to the surface normal proceeds exactly as the linear Maxwell-Garnett EMA, except using the non-linear polarization defined in equation (15), for first and third order only. For the derivation, the fact that $\mathbf{D} = \varepsilon\mathbf{E} + \varepsilon_0\chi^{(3)}\mathbf{E}^3$ is needed, where \mathbf{D} is the electric displacement field. First, consider the component parallel to the layered interfaces, which is the ordinary direction. It is known from electrostatics that the tangential component of the electric field is continuous at an interface, which implies that $\mathbf{E}^O = \mathbf{E}_m^O = \mathbf{E}_d^O$. Of course, this implies that the squares of the fields are equal as well. From electrostatics, the displacement field in the ordinary direction, \mathbf{D}^O , can also be found as an average of the displacement field in the metal and dielectric regions. Thus,

$$\mathbf{D}^O = \rho\mathbf{D}_m^O + (1 - \rho)\mathbf{D}_d^O, \quad (49)$$

where ρ is the volume fraction of the metal, which depends on the layer thicknesses. Now using the relationship of \mathbf{D} to \mathbf{E} ,

$$\varepsilon_O\mathbf{E}_O + \varepsilon_{O_0}\chi^{(3)}\mathbf{E}^{O^3} = \rho\varepsilon_m\mathbf{E}_m^O + \rho\varepsilon_{m_0}\chi_m^{(3)}\mathbf{E}_m^{O^3} + (1 - \rho)\varepsilon_d\mathbf{E}_d^O + (1 - \rho)\varepsilon_{d_0}\chi_d^{(3)}\mathbf{E}_d^{O^3}. \quad (50)$$

Canceling out the electric fields,

$$\varepsilon^O + \varepsilon_0 \chi_O^{(3)} \mathbf{E}^{O2} = \rho \varepsilon_m + \rho \varepsilon_0 \chi_m^{(3)} \mathbf{E}_m^{O2} + (1 - \rho) \varepsilon_d + (1 - \rho) \varepsilon_0 \chi_d^{(3)} \mathbf{E}_d^{O2}. \quad (51)$$

Then using the result from the linear Maxwell-Garnett EMA, $\varepsilon_O = \rho \varepsilon_m + (1 - \rho) \varepsilon_d$,

$$\varepsilon^O + \varepsilon_0 \chi_O^{(3)} \mathbf{E}^{O2} = \varepsilon^O + \rho \varepsilon_0 \chi_m^{(3)} \mathbf{E}_m^{O2} + (1 - \rho) \varepsilon_0 \chi_d^{(3)} \mathbf{E}_d^{O2}. \quad (52)$$

Next the ε^O terms cancel out, giving

$$\varepsilon_0 \chi_O^{(3)} \mathbf{E}^{O2} = \rho \varepsilon_0 \chi_m^{(3)} \mathbf{E}_m^{O2} + (1 - \rho) \varepsilon_0 \chi_d^{(3)} \mathbf{E}_d^{O2}. \quad (53)$$

Lastly, ε_0 and the remaining electric fields can be canceled out leaving

$$\chi_O^{(3)} = \rho \chi_m^{(3)} + (1 - \rho) \chi_d^{(3)} \quad (54)$$

In the equation, ρ is the metal fraction, $\chi_m^{(3)}$ is the third order susceptibility of the metal, and $\chi_d^{(3)}$ is the third order susceptibility of the dielectric. Note that it is possible to convert the nonlinear refractive index and nonlinear absorption into $\chi^{(3)}$ form and vice versa. This ordinary direction formulation works for TM with respect to surface normal, while the extraordinary direction would correspond to TE polarization. The formulation for TE polarization is more complicated, as the derivation includes local field corrections. Since this work only considers TM polarization due to the angle enhancement present there, the TE formula will not be discussed. Refer to [51] for information on it.

From this equation, it can be seen that the non-linear optical properties of the dielectric layer are required. However, from the two-temperature model, only the non-linear optical properties of the metal layer were obtained. The dielectric non-linear

properties can generally be found in the literature or through measurement. With those, it would be possible to generate the full non-linear properties of the hyperbolic metamaterials.

2.3.5 Second-Order Non-Linear Processes.

Non-linear materials can do many things that linear materials cannot. The classic example of a non-linear optical process is second-harmonic generation (SHG). Suppose a laser beam with electric field strength $\mathbf{E} = E_0 e^{-i\omega t}$ is incident on a second-order non-linear material. Then, by Eq. (55), the second-order polarization has a different form,

$$\mathbf{P}^{(2)} = \epsilon \chi^{(2)} \mathbf{E}^2 = \epsilon \chi^{(2)} E_0^2 e^{-i2\omega t}. \quad (55)$$

Therefore the second-order polarization is at 2ω rather than ω , and this polarization can lead to radiation at that 2ω frequency. Since the frequency 2ω is the second-harmonic if ω is considered the fundamental, the name second-harmonic generation is appropriate. In the photon picture, two photons of frequency ω are absorbed, and one photon of frequency 2ω is emitted. Thus energy is conserved for this process.

Second-harmonic generation is the simplest non-linear process, but many other non-linear processes are possible, which is a distinct advantage of non-linear materials that allows for many applications. SHG is actually a special case of a more general process, which is sum-frequency generation. In essence, there are two inputs of different frequency fields, and the output is a field at sum of the two frequencies. In the photon picture, a photon of frequency ω_1 and a photon of frequency ω_2 are absorbed, and a photon of frequency $\omega_1 + \omega_2$ is emitted. Difference-frequency generation is similar, but the output in that case is at frequency $\omega_1 - \omega_2$. This does differ in the photon picture, since first a photon of frequency ω_1 is absorbed, then two

photons of frequencies ω_2 and $\omega_1 - \omega_2$ are emitted. If a non-linear material is placed in a optically resonant cavity, it is possible to get larger field values at the difference frequencies. This is known as optical parametric oscillation. For this, usually one of the frequencies, either ω_2 or $\omega_3 = \omega_1 - \omega_2$ is preferred, so the preferred frequency is referred to as the signal frequency while the irrelevant frequency is called the idler frequency. For difference-frequency generation, since it involves two-photon emission, it does not actually require two inputs to happen. It is possible to provide only ω_1 as an input, and the spontaneous emission will still occur, emitting signal and idler photons. This is known as spontaneous parametric down-conversion (SPDC), and it has important applications in quantum optics [23].

2.3.6 Third-Order Non-linear Processes and Optical Switching.

There are also analogous third-order non-linear processes, which are critical for optical switching applications. The collective term for these is called four wave mixing. In essence, the sums or differences of a combination of three frequencies can be achieved, so as before, the simplest case would be third harmonic generation. There is another important process that depends on the third-order non-linear properties, which is the intensity dependent refractive index. To derive this effect, assume an incident field of $\mathbf{E} = E_0 \cos \omega t$. Then Eq. (56) shows the form of the third-order non-linear polarization, using trigonometric identities,

$$\mathbf{P}^{(3)} = \varepsilon \chi^{(3)} \mathbf{E}^3 = \varepsilon \chi^{(3)} E_0^3 \cos^3 \omega t = \varepsilon \chi^{(3)} E_0^3 \left[\frac{1}{4} \cos 3\omega t + \frac{3}{4} \cos \omega t \right]. \quad (56)$$

Thus it can be seen there is not just a contribution at 3ω , but also at the fundamental frequency ω . This implies that $\chi^{(3)}$ contributes to the refraction experienced at ω , so the material can be thought to have an intensity-dependent refractive index, which is the n_2 described in a previous section. This same concept can apply to fifth order and

all higher all odd order effects, where they have some dependence on the fundamental frequency. This idea is important for the Z-scan measurement technique which will be described in Chapter 3, and for optical bistability, so it is important to go into more detail now.

Optical bistability is a property of a device that allows for two different stable transmission states, dependent on the power of the input. In the same way, multistability would describe more than two possible stable transmission states. Then this material is placed within a cavity, which allows a change in transmission at the given laser frequency. Since the bistability arises from the material within the cavity, this is referred to as intrinsic bistability. If the source of the bistability is external, such as a mirror in an interferometer, this is known as extrinsic bistability. For a bistable system, this allows storage of binary information with one transmission state representing zero or “off” and the other representing one or “on.” Figure 4 shows generalized behavior of the power in versus power out for a system with intrinsic bistability.

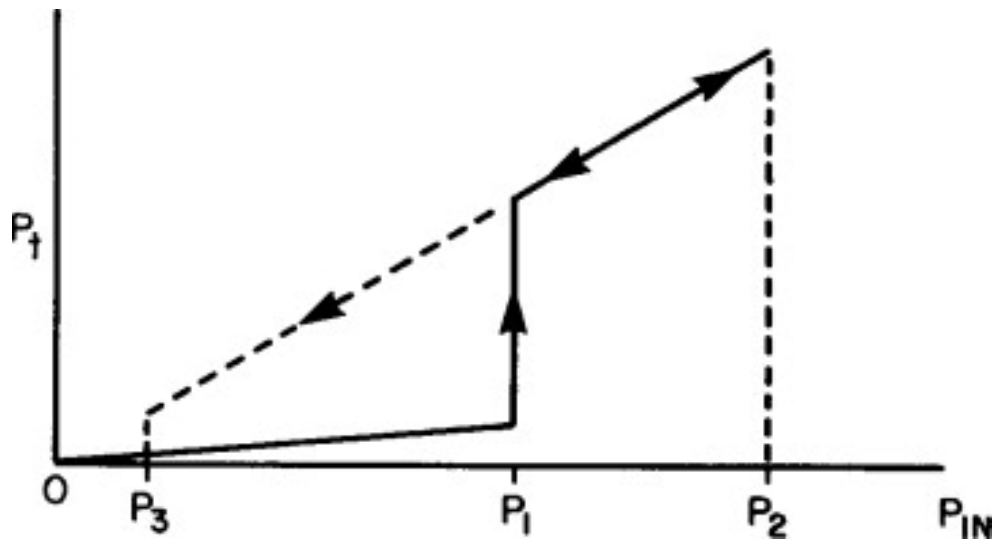


Figure 4. Generic Hysteresis Curve for Intrinsic Optical Bistability. P_{in} is the power in, while P_{\uparrow} is the power out. Modified from Source: [3]

In the figure, P_1 is the actual switching power, P_2 is the upper threshold power,

and P_3 is lower threshold power. The process, first following the solid line, is to increase the input power to the switching power. Then the system switches from the first stable state, which is the off state, to the other stable state, which is the on state. Then it is possible to increase the input power up to P_2 , and the system will remain in the on state. Once the system is in the on state, it is possible to reduce the input power down to P_3 and remain in the on state, following the dashed line. In the on state, after reducing below P_3 , the system returns to the off state. Since the output power depends on the past state of the system, these are referred to as hysteresis curves.

This special behavior is only possible because of the dependence of the effective properties on the intensity, which sets up feedback loops. For most materials, a large enough non-linear refractive index to be practical only occurs near material resonances. This is a problem, since using material resonances makes the system difficult if not impossible to optimize for both a low switching intensity and a low switching time. To correct this, a non-resonant material is preferred, and one example is a hyperbolic metamaterial. Since hyperbolic metamaterials exhibit an intensity-dependent refractive index and absorption coefficient, they could be used as optically bistable materials. A few studies have been conducted on this possibility, but there does not appear to have extensive work on the topic. One study [4] computationally modeled some possibilities for hyperbolic metamaterials, but it only considered silver as the metal. It was also purely computational and did not support any of its assertions with measurement. That deficiency was addressed in this project. However, the study did reveal that taking advantage of the topological transition from elliptical dispersion to hyperbolic dispersion, which occurs at the ENZ point, can greatly increase potential optical switching of hyperbolic metamaterials.

Here, there needs to be a note of disambiguation with regards to the term switch-

ing. Later in this document, a phenomenon where the sign of the non-linear absorption coefficient changes from positive to negative occurs. This is a “switching” from one type of behavior to a different type of behavior, but that specific behavior is **not** required for optical switching in general. An optical switch could theoretically be made from any material with an intensity dependent refractive index or absorption coefficient if the input power could be high enough, and the switching time and switching width were of no consequence. In reality, these things do matter, so the special behavior of these optimized hyperbolic metamaterials actually is valuable in increasing the switching width and having more tunability.

One important factor for all non-linear processes is efficiency, and there are several variables that can impact this. One such variable is that of phase matching. Since multiple waves are involved in most non-linear processes, if their phases do not match up, there will be destructive interference, severely reducing efficiency. The specific tests performed in this work use only one frequency, so there is not frequency mixing, but the same materials developed in this work could be used for frequency mixing applications. For non-anisotropic natural materials, it is often very difficult to achieve phase matching, since the dispersion of the material is different for one wave than it is for other. This problem can be much more easily addressed in anisotropic materials, since the angle can be adjusted to change the dispersion, and metamaterials make this even better since they can have higher anisotropy than natural materials. Hyperbolic metamaterials also have ENZ points, and as stated before, there is no phase advance at these points. Thus the phase matching conditions are automatically satisfied there. The other factors that impact efficiency are the incident power, of course the non-linear susceptibility, and also the interaction length. The interaction length is where there is a problem, since most hyperbolic metamaterials include metals, which absorb, limiting the interaction length, so applications where long propagation lengths are

required are not possible with the specific material system used in this work. However, other material systems with lower losses could overcome this difficulty. There are still many possible applications in the fields of nanophotonics where the interaction lengths are short, or through the use of all-dielectric systems this interaction length could be increased. The next sections account for specific cases where the efficiency can be greatly increased.

2.3.7 Basics of Plasmons and Surface Plasmons.

Plasmons can be thought of as oscillations of electron density in a metal, which is a plasma oscillation, hence the name plasmon. The plasma frequency is the frequency of oscillations of these plasmons, which is critical to the properties of the metal. In the case of hyperbolic metamaterials, the most important types of plasmons are the surface plasmons. Surface plasmons are confined to a surface, and occur at the interface between a dielectric and metal. They do not have to occur at planar interfaces, but can occur at the surfaces of metal nanoparticles embedded in a dielectric as well. At planar interfaces, they are usually referred to as surface plasmon polaritons (SPP), while on the surface of nanoparticles, they are referred to as localized surface plasmons (LSP). The main difference is that LSPs do not have translational invariance, so they cannot be described as easily mathematically. This leads to the conclusion that SPPs can be described by a continuous dispersion relation, but LSPs are rather described by a discrete dispersion relation, and depend much more on resonances. Both the SPPs and LSPs will be impacted by the absorption of the metal, and their decay lengths can be easily found using the skin depth formula.

2.3.8 Field Enhancement.

The most relevant property of plasmonic materials to this work is the idea of field enhancement. As seen in the last section, the second-order non-linear effects are proportional to the square of the electric field. So if the effective field becomes stronger, the non-linear effects will become much stronger. Both SPPs and LSPs can serve for field enhancement, but in general, LSPs on nanoparticles can take advantages of resonances to obtain much higher field enhancement [35]. Also, it is easier to couple the LSPs to the propagating field than SPPs, which usually require some kind of coupling grating. If the nanoparticles are spherical, they can be fully described using the well-known Mie theory [52]. Note that if the nanoparticles are close together, where LSPs from one particle interact with another, their coupling will need to be taken into account. Nanoparticle field enhancement can increase the local field up to 1000x [35]. In this work, nanoparticle field enhancement was not used, but rather a more simple angle-based field enhancement, which generally can increase the field up to about 5x. The reason that nanoparticles were not used is that this made fabrication and modeling much more tractable in the limited duration of the project. However, this more modest field enhancement in a simple layered structure will still be very noticeable in the results, which will be presented in Chapter IV. The theory of the angular field enhancement is now discussed, which follows from the field continuity at the interface between the air and material.

$$E_{\text{mat}}^{\perp} = \frac{E_{\text{air}}^{\perp}}{\epsilon_{\text{mat}}}, \quad (57)$$

where E_{mat}^{\perp} is the electric field in the material oriented normal to the interface, E_{air}^{\perp} is the incident electric field oriented normal to the interface, and ϵ_{mat} is the complex permittivity of the material. This implies that a smaller ϵ of the material gives greater field enhancement, which is generally the case near to the ENZ point. Also, since

this applies to the normal components of the fields, this factor will be zero at zero degrees incident, but will generally increase as the obliqueness of the angle increases. There is a limiting factor, that of Fresnel reflections that increase when the incident angle increases, so the optimal angle is less than 90 degrees. The linear reflection and transmission behavior can be accounted for using a transfer matrix method, which is a common method for multi-layer stacks [53].

2.4 Computer Optimized Design of Metamaterials

2.4.1 Optimization Algorithms.

There are several possible algorithms that can be used to optimize metamaterial designs, and each one has strengths and weaknesses. The first class of algorithms actually uses the gradient or approximates the gradient to find the minimum or maximum of a function, so it is calculus based mathematical optimization. Some examples of these algorithms are Newton’s method, or the gradient descent method. However, for the design problems of metamaterials the “function” in question is not as clear. Generally, a figure of merit (FOM) is chosen to act as the variable that is maximized or minimized. Then the FOM is represented in terms of changeable parameters of the design, which for non-plasmonic layered hyperbolic metamaterials are ε_m , d_m , ε_d , and d_d . The remaining problem is that this function for design problems is not guaranteed to be differentiable at every point, which makes calculus-based optimization fail. This means that it is often impossible to have a fully convergent method that guarantees global optimization for these problems.

However, a different class of algorithms, known as the heuristic algorithms, can in practice obtain minima and maxima, so if correct starting points are used, the ideal optimization can be achieved even with the non-differentiable function. There are many types of heuristic optimization algorithms, so not all can be covered here.

Two relevant algorithms will be discussed in detail, the genetic algorithm and the particle swarm algorithm. The genetic algorithm is part of a class of evolutionary algorithms that are inspired by the natural process of evolution. Every genetic algorithm has a fitness function and genomic representation of the design variables. The fitness function serves to distinguish between candidate solutions, while the genomic representation is needed to incorporate the breeding and mutation processes. These processes are inspired by biology, so mutation involves a change in a design variable, while breeding involves mixing of two “parent” candidate solutions to become one “child” solution. The genetic algorithm begins with a large set of randomly generated candidate solutions, normally referred to as the population, which have random values for the design variables. Then the following steps describe the algorithm.

1. The fitness function is evaluated for each member of the population.
2. A portion of the population is probabilistically selected to breed the next generation, with higher fitness members more likely to be selected.
3. A member of the next generation is created using a crossover process between two members of the selected part of the original generation. The new member also undergoes mutation.
4. Step 3 is repeated until the full size of the next generation is reached.
5. Repeat the process for each generation until a certain fitness is achieved or the maximum number of generations is reached.

The advantage of the genetic algorithm is that it can often be quick in determining the optimization, but there is often the problem of local maxima or minima. It is very difficult for complex design problems to determine if a local extreme or the global

extreme was reached. Thus the population size needs to be large enough to account for some members becoming stuck in local extrema.

Another heuristic algorithm is the particle swarm algorithm. This works by having a large set of randomly distributed candidate solutions called particles, which have random values of the design variables. Note this is essentially a random point in n -dimensional space, where n is the number of design variables. The following steps then describe the algorithm.

1. The FOM is calculated for each particle.
2. The position of the particle with the highest FOM is set as the swarm best, if it is greater than the previous swarm best.
3. Each individual particle sets its position as its particle best, if its current FOM is greater than its previous particle best.
4. Each particle is given an effective “velocity” both towards the swarm best and its particle best and is moved with that velocity for a set amount of time. This means the input parameters that define the particle will change to become more similar to the input parameters that define the particle best and swarm best.
5. After the amount of time has elapsed, repeat the process from step 1 until either a certain level of FOM is reached, or the maximum number of iterations is reached.

The advantages of the particle swarm algorithm are that it is much simpler than the genetic algorithm and it more naturally works with continuous variables. However, the disadvantage is that larger population sizes are needed, which can take more computational time.

2.5 Summary

In summary, the basics of the properties of linear and non-linear materials was covered, specifically, the symmetry, linear and non-linear effective medium theory, and the derivations of the non-linear properties. Then plasmonic metamaterials with information on field enhancement methods was discussed, and lastly computer design optimization was briefly explained. Next, the methodology of the work is presented.

III. Methodology

3.1 Chapter Overview

In this chapter, an overview of the methodology of the work is given. First, the fabrication methods are discussed. Next, the different methods of experimental verification are reviewed, specifically verification of fabrication quality, linear properties, and non-linear response. Lastly, the full computational modeling scheme is shown, including the modeling of the linear and non-linear properties, as well as the optimization.

3.2 Fabrication with Physical Vapor Deposition

The general method that will be employed is physical vapor deposition (PVD). The PVD methods are characterized by turning whatever is supposed to be deposited into a vapor and then condensing it back into a solid. PVD methods are routinely used for production of thin films, which is what is needed to make layered hyperbolic metamaterials. There are several different ways to produce the vapor needed for PVD. The first way that PVD can work is sputtering, specifically magnetron sputtering [54]. Magnetron sputtering uses a cascade process of ionization of inert gas such as Ar and a magnet to increase ion density and energy at the surface of the target material, causing ejection of material from the ionized bombardment that will deposit the target source material onto the substrate. The advantages of sputtering are that it works more easily on high melting point and conducting materials where other methods are difficult, and adheres better than other methods [55, 56].

The basic design of the metamaterials is comprised of alternating layers of metal and dielectric, on either a glass or silicon substrate depending on the intended application. When designing for transmissive measurements, the glass substrate was used,

but for when designing for reflective measurements, the silicon substrate was used. The materials used for the samples were indium tin oxide (ITO) as the metal and silica (SiO_2) as the dielectric, though there were intermediate samples fabricated with titanium nitride (TiN) as the metal and hafnium dioxide (HfO_2) as the dielectric. These TiN/ HfO_2 samples were not optimized and had fabrication errors, so they will not be discussed further in this document, but future work could be to optimize for that material system and fix the fabrication errors. Figure 5 shows a diagram of the fabrication setup.

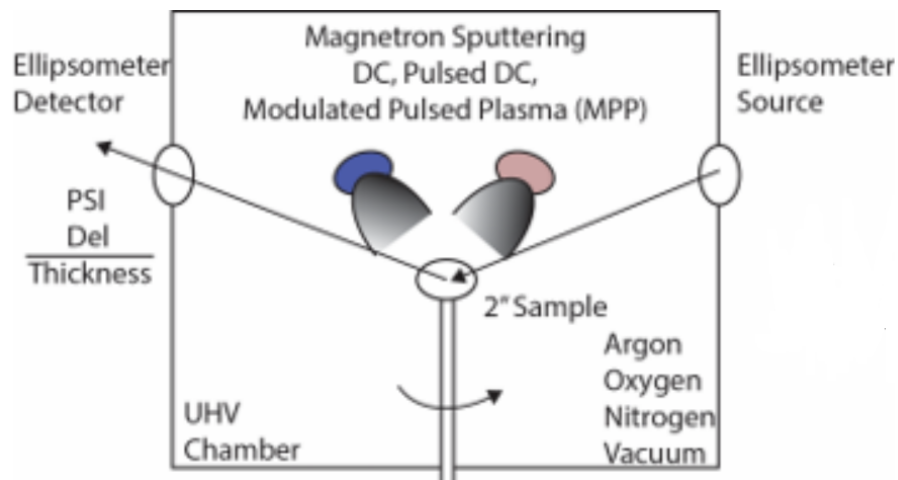


Figure 5. Diagram of Fabrication System. Two targets are shown in the chamber since that is what is used in this project, but up to four targets are possible. Different gases can be used in the chamber to obtain different deposition results. The in-situ ellipsometry allows for real time monitoring of the deposition.

The more detailed process for the ITO/ SiO_2 samples is now discussed. The magnetron sputtering requires a specific power supply to operate. The power supply can also accept a setting of “reverse time” in microseconds which is used to “discharge” the target material. For the SiO_2 reactive sputtering, a Si target was used with oxygen present in deposition chamber. This oxygen could remain the same throughout the deposition, since the ITO layer was not impacted by the presence of oxygen. For the SiO_2 sputtering, the 120 W power setting was used, with 80 kHz pulse rate and $4.5 \mu\text{s}$ reverse time; which results in pulsed DC magnetron sputter. The sputtering

process could also be operated in a constant 120 W mode, which would be DC magnetron sputtering, but with SiO₂ and reactive sputtering, the Si target material would have oxidized and an excessively high voltage would have been required by the power supply causing the system to shut off. The reverse voltage prevents this process by discharging the target, preventing significant charge build up, allowing sputtering to continue. The ITO deposition used DC magnetron sputtering at 60 W. For the initial test samples, depositions were done at room temperature, but for the final samples, the temperature of the substrate was heated to 400 degrees Celsius for the deposition of the ITO layers. This improved the consistency of fabrication of the samples.

Another feature of the fabrication is that in-situ ellipsometric data was taken with the J.A. Woollam® M-2000 ellipsometer and analyzed with CompleteEase software, so the layer formation could be tracked in real time. The incorporation of the ellipsometer into the deposition chamber is depicted in Figure 5. It can be used to define when layer thickness targets have been reached, but in this case, a timed deposition was used for simplicity. More details of the ellipsometry will be provided in section 3.3.2. Some of the earlier samples did actually use the ellipsometry model defined deposition thicknesses, but the final optimized samples all used timed deposition. Basically, since the deposition rate of the system was known, it was possible to set the overall time for each layer that would achieve the desired thickness.

However, there was one issue with this. When new deposition targets were used, the deposition rate actually changed from the standard rate, which caused the samples to have inaccurate layer thicknesses. This occurs because brand new targets are flat, while used targets develop a ring where material has been removed, so for used targets, there is much more surface area than for brand new targets. This causes the deposition rate to be higher. For some samples, this resulted in different layers in the same sample having different thicknesses, which is undesired. Eventually, the

new targets were “broken in,” and the deposition rate stabilized, so after that point, usable samples were fabricated. One result which shows the undesired effect will be presented in section 5.5.

Two different batches of samples will be discussed in this work, one test batch that was not optimized, but served as data for the verification of models and methods, and the second batch, which contains the optimized samples. The results from first batch will be covered in Chapter IV, while the results from the final optimized batch will be covered in Chapter V.

Table 3. Unoptimized Test Designs. The thickness of the layers in the metamaterial and the number of dielectric-metal pairs is provided. The metallic component is ITO and the dielectric is SiO₂.

Metal Layer Thickness (nm)	Dielectric Layer Thickness (nm)	Number of Periods
10	25	6
10	40	6
20	20	6
10	25	8
10	40	8
20	20	8
10	25	10
10	40	10
20	20	10

So nine samples in total were fabricated according to the designs of Table 3. Next the recipes for the optimized design are shown. The process of optimization will be described in section 3.5, while the computational results from the optimizer will be shown in section 5.2, but the recipes are shown here in Table 4 to allow for comparison to the unoptimized test designs.

Table 4. Optimized Designs. The thickness of the layers in the metamaterial and the number of dielectric-metal pairs is provided. The metallic component is ITO and the dielectric is SiO₂.

Metal Layer Thickness (nm)	Dielectric Layer Thickness (nm)	Number of Periods
52	95	12
52	105	12

Note that metal layers are in general thicker for the optimal designs than for the test samples, which was chosen because it increased consistency in layer thickness fabrication. Also, 12 periods were used instead of six, eight, or ten, since optimization revealed that a greater number of periods led to better performance. Fabrication limits led to capping the maximum number of periods at 12 for this work, but future work could be to increase that number. There were multiple copies of each recipe produced, specifically three each, giving six total growths. Next, the experimental methods of the work are covered.

3.3 Experimental Verification

3.3.1 Fabrication Quality with Microscopy.

There are several ways to address fabrication quality. One way is using atomic force microscopy (AFM) to examine the surface roughness of the deposition. A low surface roughness generally corresponds to a high quality fabrication. Another way is using electron microscopy, such as tunneling electron microscopy (TEM) or scanning electron microscopy (SEM) to acquire images of the metamaterial. These images are used for a visual confirmation of quality and the confirmation that proposed layer thicknesses were actually achieved. Figure 6 shows an example TEM image of a hyperbolic metamaterial.

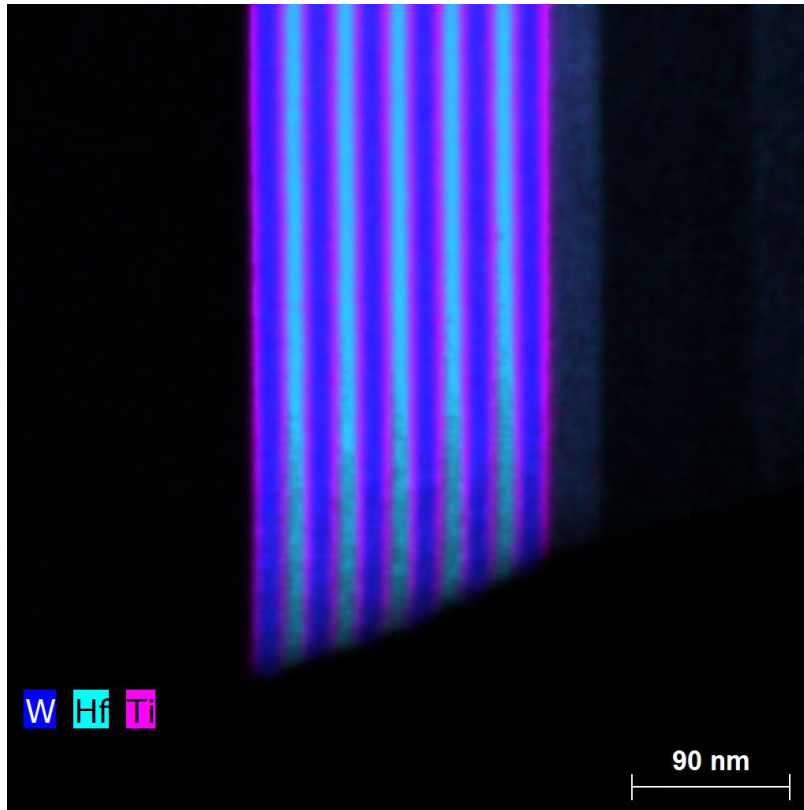


Figure 6. Example TEM of a Layered Metamaterial. In this case, it is a tungsten-hafnium-titanium stack. Taken by Cynthia Bowers at AFRL/RX. Used with permission. The included length scale would allow for determination of layer thicknesses, and the different elements in the stack can be observed through the applied spectroscopic data.

From Figure 6, it is possible to derive layer thickness using the included length scale and image analysis software. Also, the system has included spectroscopy data, so it is also possible to check the composition of the deposited materials. For these reasons, TEM imagery was used to confirm the correct composition as well as the layer thicknesses for representative samples fabricated during this project. The results of this imagery for different samples will be presented in sections 4.2 and 5.3.

3.3.2 Linear Measurements with Spectral Ellipsometry.

Now that the fabrication quality has been addressed, the optical properties of the hyperbolic metamaterial need to be measured. To analyze the linear optical constants,

the technique of ellipsometry will be used. Ellipsometry is a measurement technique that uses polarized light to characterize samples, such as thin films, bulk materials, and layered structures. It measures the relative phase change in polarization states of light reflected off (or transmitted through) the sample's surface. These measurements describe how samples modify the polarization state at each angle of incidence [57].

To understand what happens to the polarization state, it is important to know basic properties of reflection. It is known that the total reflection coefficients are the ratio of the amplitude of the reflected wave to the amplitude of the incident wave at different polarizations. For thin films, they are defined as

$$\mathbf{R}^p = \frac{r_{12}^p + r_{23}^p e^{-i2\beta}}{1 + r_{12}^p r_{23}^p e^{-i2\beta}} \quad (58)$$

$$\mathbf{R}^s = \frac{r_{12}^s + r_{23}^s e^{-i2\beta}}{1 + r_{12}^s r_{23}^s e^{-i2\beta}} \quad (59)$$

where the r with a subscript is the Fresnel reflection coefficient between the specified mediums, and β is the film phase thickness. The superscript p refers to the polarized wave in the plane (parallel polarization) and the superscript s refers to the polarized wave perpendicular to the plane of incidence (senkrecht polarization). The amplitude of both parallel and perpendicular components may be altered due to reflection of the sample. Eqs. (58) and (59) represent the ratios of the reflected wave amplitude to the incident wave amplitude for both parallel and perpendicular components. Similar equations can be written for any arbitrary number of layers.

These reflection coefficients are related to the amplitude ratio, Ψ which is a value of interest from the experiment. First, define the complex quantity ρ to be the complex ratio of total reflection coefficients, R^p and R^s , such that $\rho = \frac{R^p}{R^s}$. Then $\rho = \tan(\Psi)$, and is clearly a measure of how much light is p-polarized versus s-polarized. Another value of interest is the total phase difference, Δ . The phase difference between both

the parallel and perpendicular components of the incoming wave is referred to as δ_1 while the phase difference in the reflected wave is referred to as δ_2 . To account for both of those, Δ is used and defined as $\Delta = \delta_1 - \delta_2$. Delta can change in phase difference upon reflection off the sample [57]. The process of ellipsometric measurement from light source to detector is shown in Figure 7 from [58].

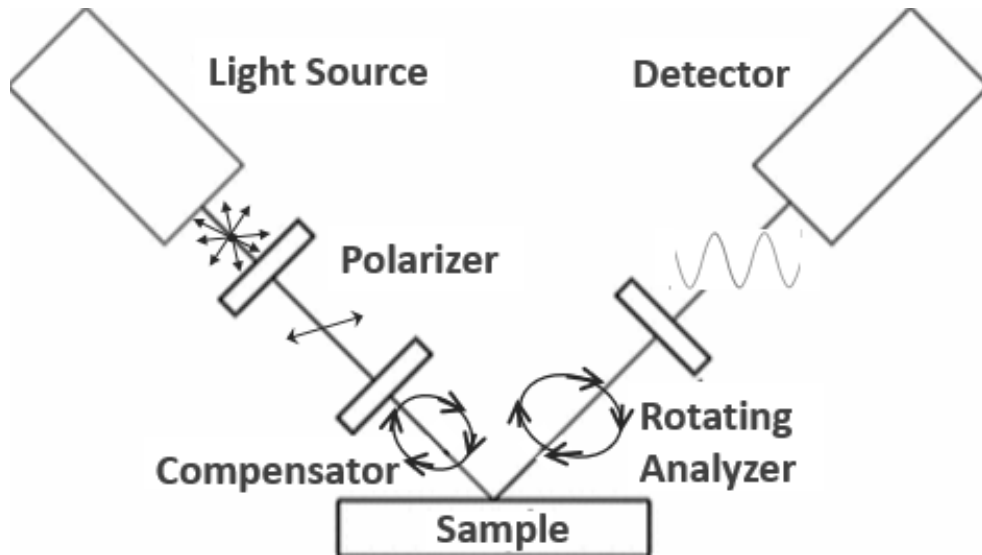


Figure 7. Diagram of the Ellipsometry Process. The polarizer and compensator produce circularly polarized light incident on the sample, and then the detector determines the precise polarization state of the reflection off the sample.

Returning to Figure 7, the reflection off the sample can generate a phase shift and/or attenuate one or both of the passing wave components. The reflection off the sample will not generally produce a light beam linearly or circularly polarized, rather something elliptically polarized. These various shifts of the phases are influenced by the optical properties of the samples, such as the thickness of layers, material composition, temperature, and orientation. The reflected signal of the different polarization states will be determined by the detector after passing through the analyzer. The spectral nature of the signal at the detector is analyzed using a spectrometer.

In general, the detected signal is a voltage sinusoid with a *DC* offset in the form:

$$V(t) = DC + \alpha \cdot \cos(2\omega t) + \beta \cdot \sin(2\omega t) \quad (60)$$

The ellipsometer measures this voltage with a photovoltaic detector, and does the fast Fourier transform (FFT) to find the two quantities α and β which are the Fourier coefficients of the signal. They can be written in terms of Ψ and Δ values, and the value P , the input polarizer angle with respect to the plane of incidence [58]

$$\alpha = \frac{\tan^2(\Psi) - \tan^2(P)}{\tan^2(\Psi) + \tan^2(P)}, \quad (61)$$

$$\beta = \frac{\tan^2(\Psi) \cos(\Delta) \tan(P)}{\tan^2(\Psi) + \tan^2(P)}. \quad (62)$$

Equations (61) and (62) can be inverted to obtain the ellipsometric parameters, Ψ and Δ , which are the terms used to characterize the sample [58]. This α and β measurement is repeated many times for the same P , usually between 10 and 100, to also calculate a measure of noise in the system. This noise in α and β can be converted to uncertainty in Ψ and Δ , thus there can be certainty that Ψ and Δ actually represent signal rather than noise. These Ψ and Δ measurements are essential, because the quantities combined with an assumed model are used to calculate the material properties, such as the optical constants and thickness. Note the calculated properties are as reliable as the model, meaning Ψ and Δ can be correct, but an incorrect model can make the calculated properties meaningless.

Once experimental data in the form of Ψ and Δ over the specified spectral range is obtained, then a model of the material is created in accompanying software. In the case of a J.A. Woollam® ellipsometer, the software WVASE32 or CompleteEASE [58] is used with the following process. Each layer of a layered material is modeled

separately. The software contains a database of materials with bulk optical constants that can be used for each layer. When creating a layer, a material and a layer thickness is chosen. Once a basic model is created, the next step is to fit the model to match the experimental data. This is accomplished by calculating the mean squared error (MSE) between the model's predictions and the experimental data, and then adjusting fit parameters to minimize the MSE. The formula for MSE is

$$MSE = \sqrt{\frac{1}{2N - M} \sum_{j=1}^N \left[\left(\frac{\psi_j^{mod} - \psi_j^{exp}}{\sigma_{\psi,j}^{exp}} \right)^2 + \left(\frac{\Delta_j^{mod} - \Delta_j^{exp}}{\sigma_{\Delta,j}^{exp}} \right)^2 \right]}, \quad (63)$$

where N is number of experimental data points, M is the number of fit parameters, and the rest of the equation calculates the differences between the model and experiment at each point and then divides by the standard deviation of the experimental measurements. Any of the optical constants or thicknesses of the layers can be selected as fit parameters, but the number of fit parameters should generally not exceed the number of layers. The minimization of the MSE through adjusting the fit parameters is an iterative process that can be repeated as many times as necessary to achieve a low MSE, though typically less than 100 iterations are needed if good starting points are chosen. Unfortunately, while there are good database entries for common materials such as silicon that give good starting points, the data on rarer materials is much less accurate. Even with that limitation, accurate model fits are achievable when the material is simple, such as a one layer material. For the hyperbolic metamaterials, using the Maxwell-Garnett EMA as a starting point in WVASE32 or CompleteEASE software allowed for accurate results, and these results will be shown in sections 4.3 and 5.4.

3.3.3 Non-Linear Measurements with Z-Scan.

With the linear measurements completed, the next step is to determine the non-linear properties. One common method for calculating the third-order non-linear susceptibility is the Z-scan technique [59, 60, 61, 62]. The Z-scan technique can measure both the non-linear refractive index and the non-linear absorption coefficient, which are related to the third-order non-linear susceptibility, as discussed in Chapter II. Figure 8 shows a diagram of the Z-scan setup.

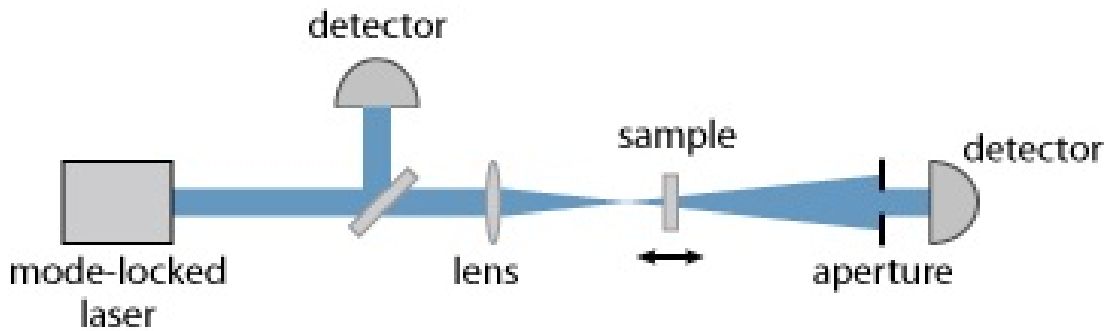


Figure 8. Diagram of Basic Z-scan Setup. The Z-scan method can be used to calculate the non-linear refractive index. In the diagram, it is in the closed configuration since the aperture is present.

First, the mode-locked or otherwise fluctuation-compensated laser goes through a lens that focuses the beam. Now, due to the sample having appreciable non-linear properties, the beam will be focused or defocused as it hits the sample. This occurs because the beam intensity is not constant in space, rather it is the case that the center of the beam has a greater intensity than the edges. Since the non-linear process depends on the strength of the applied field, the edges of the beam will be impacted differently than the center. This focusing is dependent on the position of the sample on the z axis, so by moving the sample along that line, the transmission at the detector will change. This is where the name Z-scan comes from. The aperture determines the configuration, which determines whether a measurement of the real or imaginary non-linear index is obtained. When the aperture is present, it is the

closed configuration, and large amounts of refraction occurs, thus measurements of the non-linear refractive index can be made more easily, but non-linear absorption also occurs. When the aperture is absent, it is the open configuration, and there the non-linear absorption coefficient alone can be measured. Thus analysis of closed aperture measurements generally requires accompanying open aperture measurements.

For the unoptimized test samples, Z-scan data was taken mostly at a wavelength 1.7 microns, but some data was taken at 2.1 microns. For the optimized samples, Z-scan data was taken at 1.78 and 1.835 microns with a peak intensity range of about 20-200 GW/cm². For this case, the laser used was a pulsed optical parametric oscillator (OPO) system with a repetition rate of 10 KHz and a pulse width of 150 fs, allowing for the high peak intensity necessary to observe non-linear effects. Amplified Ge detectors were used due to their sensitivity in the wavelength regions of interest. The final measurements are focused on non-linear absorption, so the open-aperture configuration of the Z-scan was primarily used, though some closed-aperture measurements were taken for reference.

Note that the optimized sample measurements were all taken using TM polarization in order to observe the angle-dependent field enhancement. To get angle-dependent data, the sample was placed on a rotating stage, so when referring to the diagram in Figure 8, the only difference for the oblique angle measurements is that the sample is rotated. The result of the Z-scan is a detector voltage for each Z-position, and there are different ways to show the data. In this work, normalized transmission is generally used. The real transmission can be calculated easily with Z-scan using the detector voltage with no sample compared to the detector voltage with a sample, and then this real transmission value can be normalized to the value far away from the focus, where the incident intensity is much lower and linear effects dominate. This means that any divergence from a transmission of one in the normalized transmission

plots shows some non-linear effect.

Usually, a simulation of the Z-scan setup is run and simulated transmission values are obtained which are fit to the Z-scan values. Since the simulation takes in the actual non-linear properties as inputs, it is then possible to determine the best fit non-linear properties, in a similar manner to the linear ellipsometry. This was done for the unoptimized test samples, and thus the values of non-linear properties were found, which are presented in Section 4.5. However, for the optimized samples, this was not possible because the properties of the hyperbolic metamaterials were outside of bounds of applicability for the simulation code. The simulation code that was available could account for relatively small changes to the normalized transmission, generally less than a 20% change. But due to the field enhancement in the optimized samples, the change in normalized transmission can be higher than 400%. So for those cases, the normalized transmission plots were provided, but the actual values of the non-linear properties could not be determined. Future work could be to improve the Z-scan simulation approach in order to obtain those values.

3.4 Modeling Linear and Non-linear Hyperbolic Metamaterials

For the linear properties of the hyperbolic metamaterials, generally, the Maxwell-Garnett EMA was used if a permittivity was needed, while the transfer matrix method was used if reflection and transmission coefficient were needed. There are quick running codes implemented in MATLAB[®] that use the transfer matrix method to calculate reflection and transmission, which will eliminate any possible discrepancy from using an effective medium approximation.

First, the metal layer of the hyperbolic metamaterials was modeled using the delayed two-temperature model as shown in Equations (38) through (47), with the implementation in MATLAB[®]. To solve the system of differential equations, the

MATLAB® stiff ordinary differential equation solver “ode15s” was used. To verify that the model was correctly implemented, recreation of the results from source [1] is performed. The exact same material properties and input powers were used to make the comparison. Figure 9 shows the two temperature results from the current implementation and Figure 10 shows the two temperature results from the source.

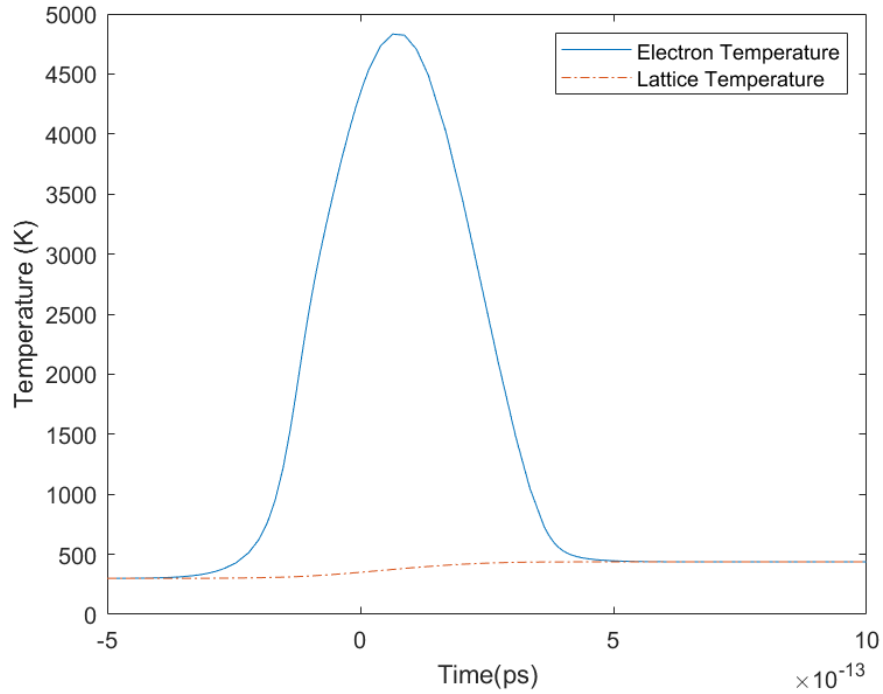


Figure 9. Electron and Lattice Temperature Plot of an 310 nm ITO Film. Both temperatures start out at room temperature, and then a pulse with intensity 66 GW/cm^2 and duration 150 fs is applied, centered at $t = 0$. The electron temperature rises quickly, but then transfers energy to the lattice and then the lattice and electron temperatures equalize. Off the left side of the figure, both temperatures will return to the room temperature.

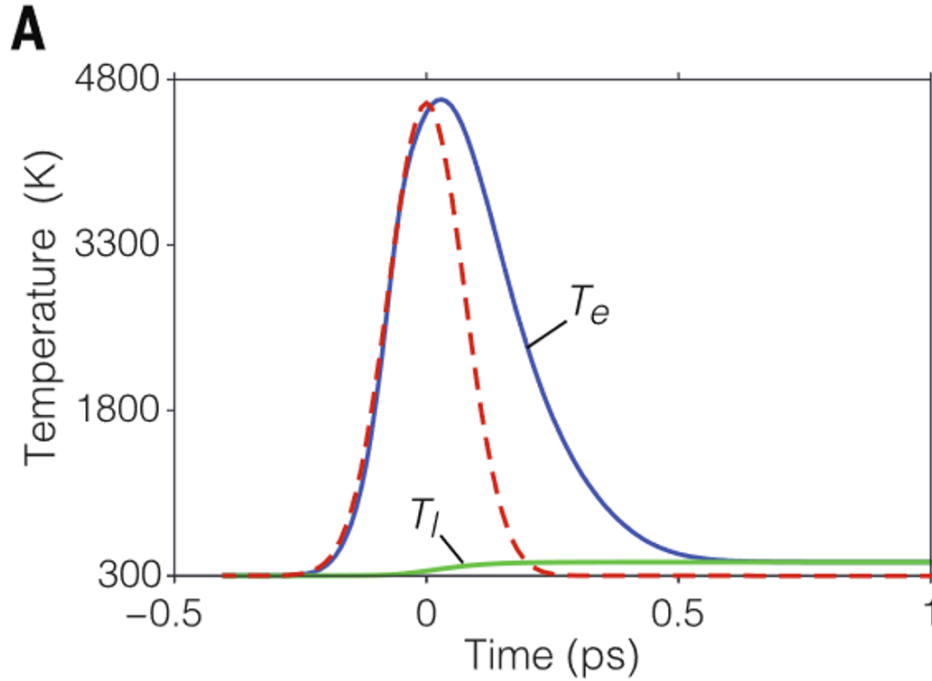


Figure 10. Electron and Lattice Temperature Plot of an 310 nm ITO Film from source [1]. Reprinted with permission.

This is good verification, but the ultimate goal is to calculate the non-linear properties, not just the electron temperature. Therefore, another comparison to source [1] is made, but this time for comparison of the non-linear refractive index. To accurately calculate the non-linear refractive index, the field enhancement discussed in section 2.3.8 was incorporated into the two temperature model. This works by effectively increasing the power applied for oblique incidence angles. A critical note here is that the field enhancement is applied to ITO only for this comparison, but for the actual optimization described in sections 3.5 and 5.2, the field enhancement is applied to the hyperbolic metamaterial as a whole. Figure 11 is the result from the current implementation, while Figure 12 is the result from source [1].

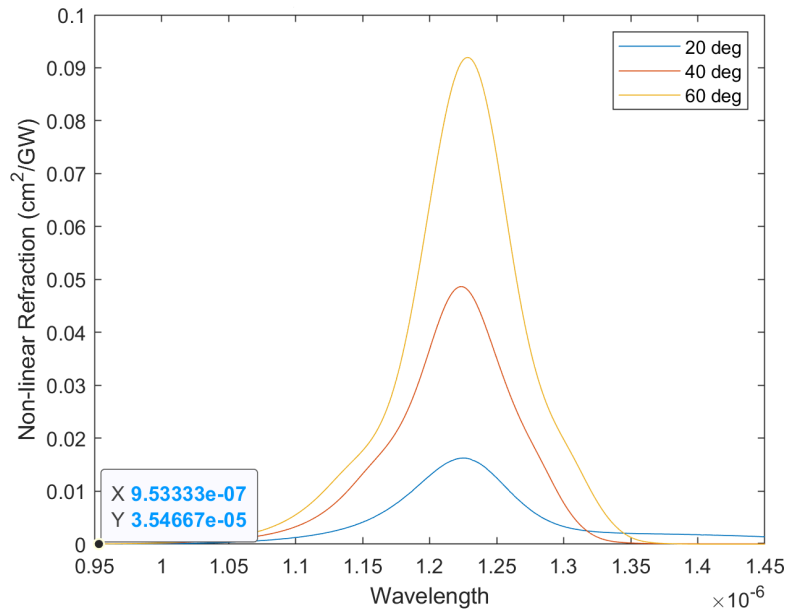


Figure 11. Non-linear Refraction Plot Showing Angle Enhancement. The input pulse and ITO film properties for this plot is the same as used to create Figures 9 and 10. The ENZ point for this film is around 1.24 microns, and a large enhancement that increases with angle is seen at that wavelength. The data tip near the bottom of the plot is for comparison to the value in Figure 12.

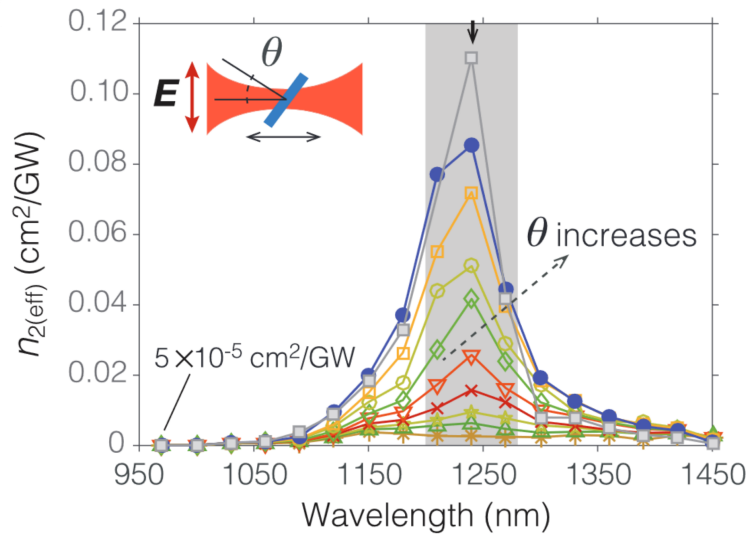


Figure 12. Non-linear Refractive Index Plot Showing Angle Enhancement from source [1]. Reprinted with permission.

From Figures 11 and 12, there is clearly a large enhancement of non-linear proper-

ties near the ENZ point that increases with angle. Figure 13 shows that the optimal angle will be limited by Fresnel reflections by plotting the resultant n_2 from the two-temperature model for different incidence angles.

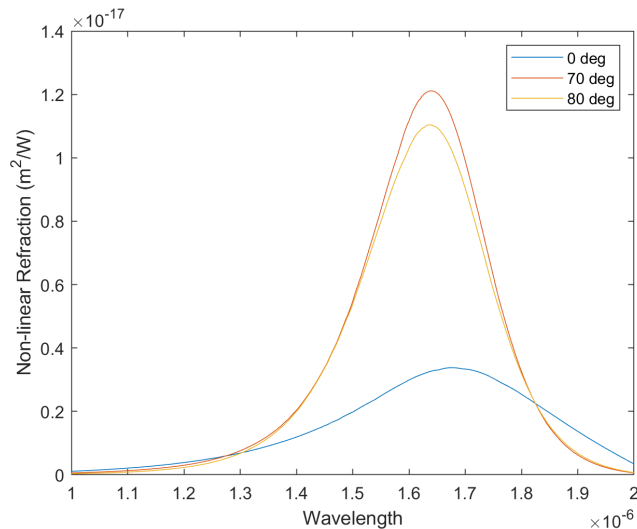


Figure 13. Non-linear Refractive Index Plot Showing Angle Enhancement. The ITO has an ENZ point near 1.7 microns The 80 degree curve is actually lower than the 70 degree curve, which demonstrates that the Fresnel reflections start to dominate between 70 and 80 degree for these ITO properties.

This gives the properties of the metal layer, but to get the actual non-linear properties of the hyperbolic metamaterial, the non-linear effective medium, equation 54 from section 2.3.4, must be used. Recall that this formula requires the non-linear properties of the metal and dielectric components. For that dielectric component, values from the literature for SiO_2 were initially used [63], and they were later confirmed with measurement. The final values used were $n_2 = 2.5 * 10^{-20} \text{ m}^2/\text{W}$ and $\beta = 9.7 * 10^{-15} \text{ m}/\text{W}$.

3.5 Optimizing Hyperbolic Metamaterials

To get all possible information about the materials, including their switching properties, the modeled materials with their linear and non-linear properties were placed

into a full field simulation in the software *Lumerical*, and then the this simulation was used in an optimization scheme.

In this work, multi-objective optimization is used. This means that there are two separate functions that determine the performance of the design, the details of which will be described later. In that case, there will always be trade-offs between the two functions, basically, it is not possible to get the most optimal point for each function separately. Instead, the optimization obtains what are called Pareto optimal points, or just Pareto points. These are the points that define a region where moving from that region will result in a decrease in one of the objective functions. In this work, there are two objective functions, so the Pareto region is a line in output space. The output or function space is the evaluation of the objective functions, while the input or parameter space is input variables to the objective function. There is a one-to-one correspondence between the members of input space and members of the output space.

This leads to a modeling framework for a genetic optimization algorithm as follows:

1. For a specific number of population members, design geometries are randomly generated.*
2. The linear and non-linear properties of each of those geometries are derived using the Maxwell-Garnett EMA, the TTM, and the non-linear effective medium.*
3. These properties and geometries are inserted into *Lumerical*, and the electric fields are calculated for a range of intensities.
4. The electric input and output fields, before and after the sample, are used to calculate the intensity dependent transmission, which can be analyzed to evaluate the objective functions.

5. The population then evolves according to the genetic algorithm, and the process returns to step 2 and repeats until the max number of generations is reached.*

For actual optimization, the full modeling framework takes too long to run for interrogation of the entire design space, so instead of running the full modeling scheme, a partial scheme was used separately to optimize for properties that corresponded to any desired behavior. This partial scheme consists of the starred steps in the above modeling process. This correspondence was verified by running the full modeling framework for a limited population size, and observing that optimal points were the same as the partial scheme. Figures 14 and 15 show the comparison of optimal points in parameter space between the MATLAB® scheme and the *Lumerical* scheme. Figure 14 is an optimization for a hyperbolic metamaterial with an ENZ point near 1.7 microns, and Figure 15 is an optimization for a hyperbolic metamaterial with an ENZ point near 2.5 microns. This was done to demonstrate the correlation is not dependent on a specific set of material properties, but is more general.

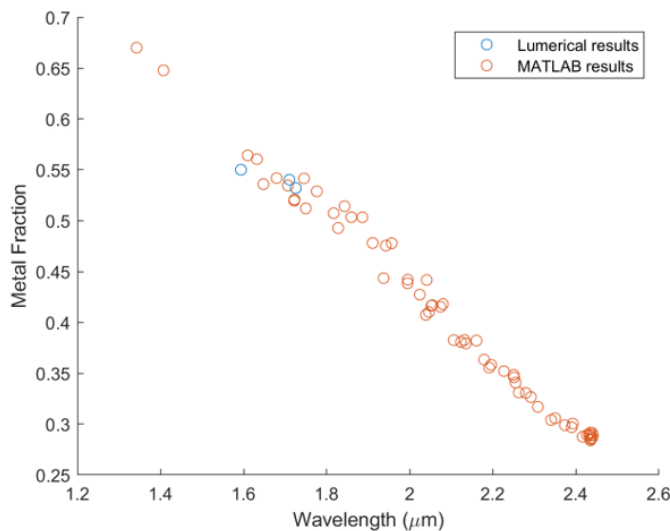


Figure 14. Pareto Plot in input space showing results from *Lumerical* and MATLAB® schemes. There is overlap near the ENZ point of the structure, which in this case is near 1.7 microns. The *Lumerical* scheme by necessity had fewer population members and generations.

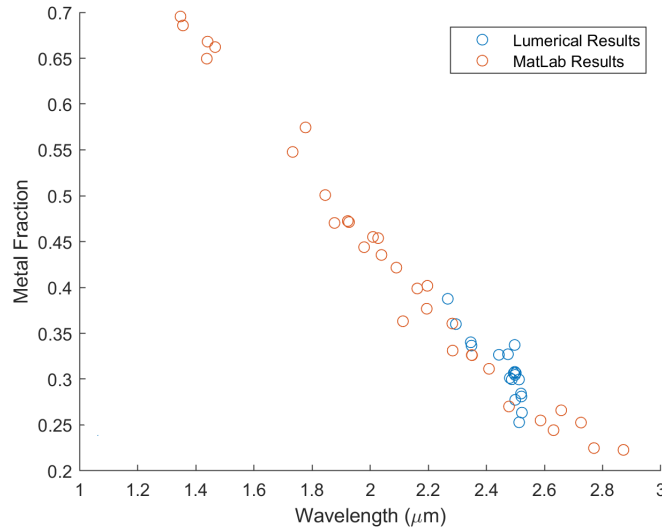


Figure 15. Pareto Plot in input space showing results from *Lumerical* and MATLAB[®] schemes. There is overlap near the ENZ point of the structure, which in this case is near 2.5 microns. The *Lumerical* scheme by necessity had fewer population members and generations.

Note that this older version of the MATLAB[®] scheme had an error where the angle enhancement was incorrectly applied, so the optimal points were spread out in wavelength, but in the most updated scheme, which will show results in section 3.6 and 5.2, the optimal points are much more clustered around the ENZ point, which would give even more correlation between the two schemes. This gives confidence that the running the MATLAB scheme alone gives results that are optimal, especially near the ENZ point.

In general, the genetic algorithm works by starting with a random population, and applying biology-inspired processes such as mutation, crossover, and inheritance to generate the next generation that is improved in terms of the objective function or functions. For all the optimizations in section 3.6, a standard of 5000 generations with 150 population members was adopted, but this could be greatly increased with more computational resources and time. This amount of generations and population members is not possible with the full *Lumerical*-based scheme.

There are many variables that go into the design, and each of them can be set as a fixed value during the optimization, or set as design variables and modified during the optimization. The possible variables are the thickness of the metal layer, the thickness of the dielectric layer, the angle of incidence, the wavelength of operation, the input polarization, the input beam intensity, the input beam pulse duration, and the number of periods in the metamaterial stack. For optimization in section 3.6, the first four variables listed are chosen as optimization variables, while the last four are chosen to be fixed. This was mostly a matter of convenience rather than necessity, and it is possible to have all eight as optimization variables with some code modifications.

For all the following results in section 3.6, the values of the fixed variables will be listed here. The input polarization is set to TM polarization for every case, since that polarization gives the angle enhancement. The input beam intensity is set to 6.6×10^{14} W/m², which is strong enough to see nonlinear properties, but not too high as to lead to a higher electron temperature than Fermi temperature. The input pulse duration was set to 150 fs, which is a realistic value for a high power laser system. The number of metamaterial periods was set to eight, since that was used as a fabrication goal my previous work [64], and it fulfills the condition for accuracy of at least six periods found in [65].

For the optimization input variables, they were free to vary over a set range. For the metal and dielectric layer thicknesses, the ranges were set from 20 nm to 100 nm. Lower than 20-nm thick layers can be more difficult to fabricate and have non-trivial quantum effects, while greater than 100-nm thick layers could cause a violation of the effective medium assumption. The angle of incidence was allowed to vary from 0 to 89 degrees. The wavelength was allowed to vary from 1 to 2 microns, which guarantees that any features will be at max of size $\lambda/10$. Here, a note is required; in this work, the devices are only optimized for operation at a single wavelength. However, many

devices are required to work in a certain wavelength band. It is possible to modify the code to optimize for performance over a set wavelength band, rather than find the optimal single wavelength, but the current approach gives more information about the best possibilities in the design space.

Note that this scheme can be used for many different applications by selecting different optimization output variables [66], and some information on what can be achieved with that will now be presented. For these tests of the optimization capability, values for the linear properties of ITO from literature were used.

3.6 Computational Tests of Optimization Scheme

Note that most of the information in this section was published as a conference proceedings paper [66].

For the first test, the goal is to have the largest possible non-linear refractive index, while limiting both linear and non-linear absorption. Thus n_2 is maximized while the quantity $\kappa + \beta I_0$ is minimized. There are many applications where absorption is undesirable, such as frequency conversion. Thus determining how low absorption can be while still maintaining strong non-linear properties is very useful. Note that in the upcoming input space plots, only the input variables of layer thicknesses and wavelength are shown, without showing the optimal angle. In general, the optimal incident angle is the same for every member of the population, so a plot for it is unnecessary. Also, instead of the specific layer thicknesses, ρ is used, which is defined as

$$\rho = \frac{th_m}{th_m + th_d}, \quad (64)$$

where th_m is the thickness of the metal layer and th_d is the thickness of the dielectric layer, which makes ρ the metal fraction. This is the key parameter for effective

medium theory as seen in section 2.1, so it makes sense to use it when examining designs. Figures 16 and 17 show the Pareto points in input and output space respectively.

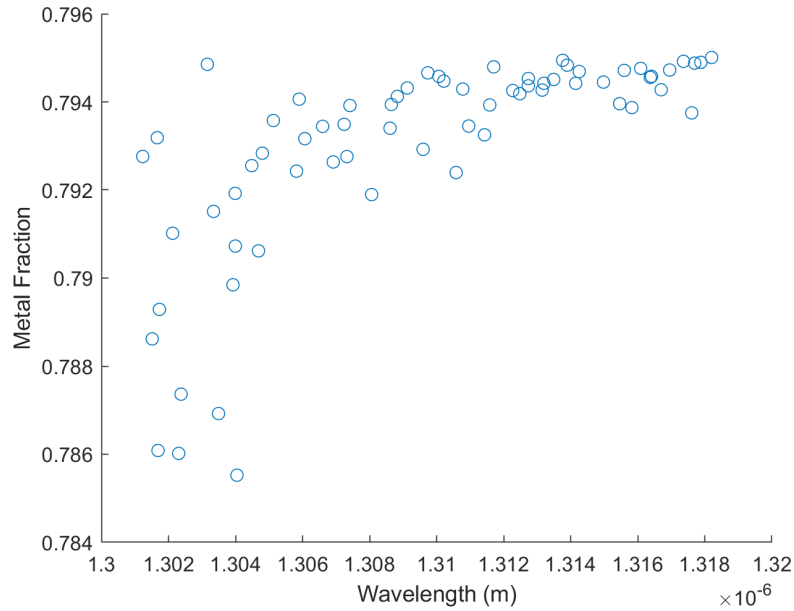


Figure 16. Refractive Device Pareto Points in Input Space. The optimal metal fraction seems to be around 0.792, while the optimal wavelength is around 1.31 microns. The optimal angle (not shown) is around 65 degrees.

Figure 16 shows that the best inputs are tightly clustered around a certain wavelength and metal fraction. This makes sense, since the device will perform the best near the ENZ point, due to the field enhancement there. For an ITO film, the ENZ point is near 1.24 microns, but for a 80% ITO 20% SiO₂ metamaterial, the ENZ point is near 1.31 microns, which is exactly where the optimal behavior is found.

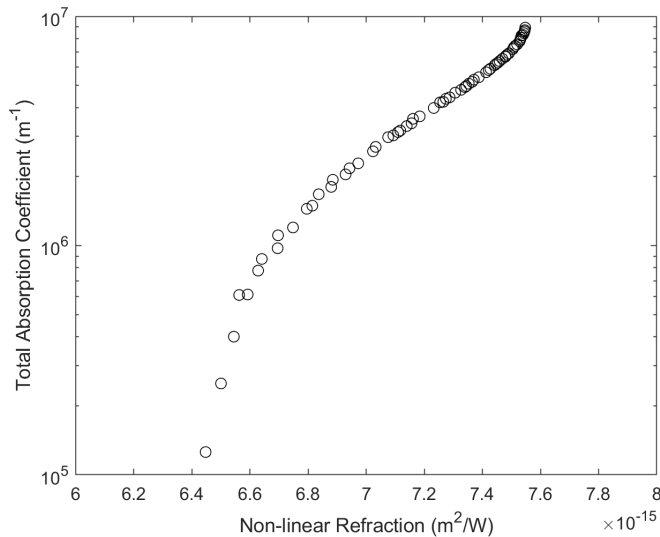


Figure 17. Refractive Device Pareto Points in Output Space. Note that the total absorption coefficient on the y-axis is plotted using a logarithmic scale.

Figure 17 shows that the hyperbolic metamaterial can have strong non-linear refraction, up to $7.6 \times 10^{-15} \text{ m}^2/\text{W}$, while still capable of having a attenuation coefficient that is much smaller than is typical for metals of near 1000 cm^{-1} . It is possible that with other material systems than ITO/SiO₂, strong nonlinear refraction could be obtained with very low attenuation, which is something that should be explored in the future. The output plot also demonstrates how it possible to use the Pareto front to determine a design for a specific application. For example, if there is an application that requires an attenuation coefficient less than $1 \times 10^6 \text{ 1/m}$, the Pareto point that corresponds with that on the output plot is near the bottom of the curve. And then since there is a one-to-one correspondence between the input and output points, the input variables that correspond to that point can be found. So it is simple to find the design parameters needed to get that desired performance, and then fabrication to those parameters is also easier since it is a 1D design. The next example illustrates a more complicated application.

For the second test, the goal is develop an optimized optical switch. For an

optical switch, two measures of performance are the switching intensity, which is the incident intensity to trigger the switching behavior, and the switching width, which could be described as the difference in transmission between the OFF and ON state of the switch. In general, the desire would be for the switching intensity to be as low as possible, while the switching width as large as possible. The problem that arises is that the model does not directly calculate these quantities. However, the model does calculate some quantities that should correlate to the desired switching metrics. Therefore, the optimizer will be set to maximize the nonlinear refraction and maximize the derivative of linear transmission. With a stronger non-linear refraction, clearly the non-linear behavior which is required for optical switching will occur at a lower input intensity, thus lowering the switching intensity. If the derivative of transmission is maximized, then the result is a system that changes transmission more strongly, which corresponds to a larger switching width. This relationship will be discussed in more detail in Chapter V. Figures 18 and 19 show the Pareto points in input and output space respectively.

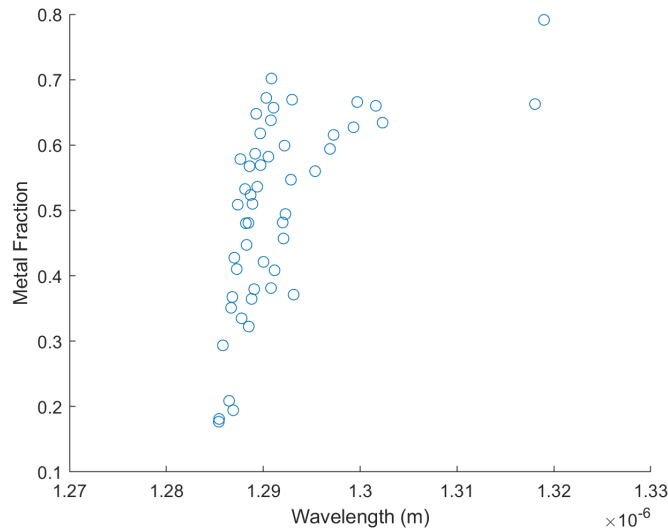


Figure 18. Optical Switch Pareto Points in Input Space. As before, ρ is used instead of the individual layer thicknesses. The optimal metal fraction varies from 0.2 to 0.7. The optimal wavelength varies from around 1.28 to 1.32. The optimal angle is around 50 degrees in this case.

Figure 18 shows that a wider range of metal fractions is possible to achieve Pareto optimal performance in this optical switch optimization as compared to the refractive device optimization. However, it is still the case that the best behavior is obtained near the ENZ point. The optimal angle is lower than the previous case, which arises from the Fresnel effects in linear transmission at larger incidence angles, which was not as strong of a factor in the previous optimization.

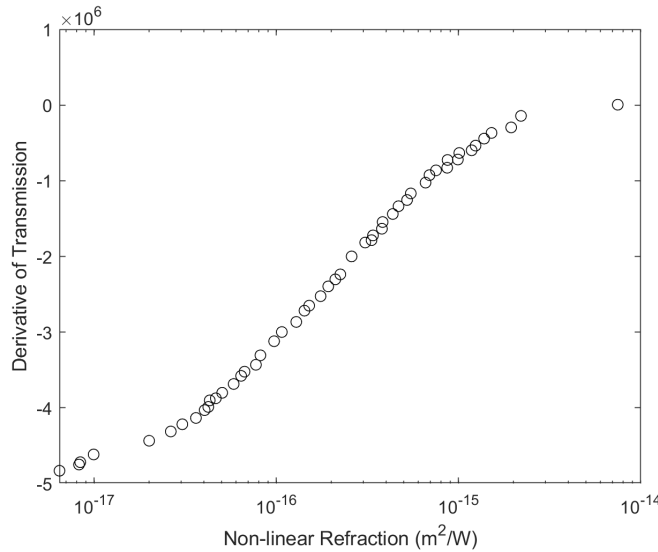


Figure 19. Optical Switch Pareto Points in Output Space. Note that the nonlinear refraction on the x-axis is plotted using a logarithmic scale.

Figure 19 demonstrates how wide the design space actually can be, even for a 1D system. It is possible to obtain extremely high nonlinear refraction, while having a differential transmission near 0, or it is possible to obtain a lower nonlinear refraction, while having a strong differential transmission. Note that the differential transmission is negative because in general, at short wavelengths the layered metamaterial has dielectric like behavior with a high transmission, and then past the ENZ point, it transitions to metal like behavior with a low transmission. Thus the transmission in general decreases with increasing wavelength. Through these two optimization tests, the potential of the optimization code has been demonstrated. It will next be used

to derive optimized samples that were actually fabricated in section 5.2.

3.7 Summary

In summary, the methodology of the work was presented. First, fabrication methods were discussed, and all successfully fabricated designs were listed. Next, the measurement methodology, for fabrication quality, linear properties, and non-linear properties was covered. Then the full modeling and attached optimization scheme were shown, with demonstrations of the optimization possibilities. In the next chapter, the results for the unoptimized test samples are presented.

IV. Initial Test Results

4.1 Chapter Overview

In this chapter, the results of unoptimized designs are covered, first looking at the fabrication quality, then the linear results, and lastly the non-linear results. Note that most of this chapter was published as a conference proceedings paper [64].

4.2 Fabrication Results

To confirm that the desired designs listed in Table 1 in section 3.1 were achieved, TEM images of the samples were taken. Figure 20 shows a TEM image of one of the samples.

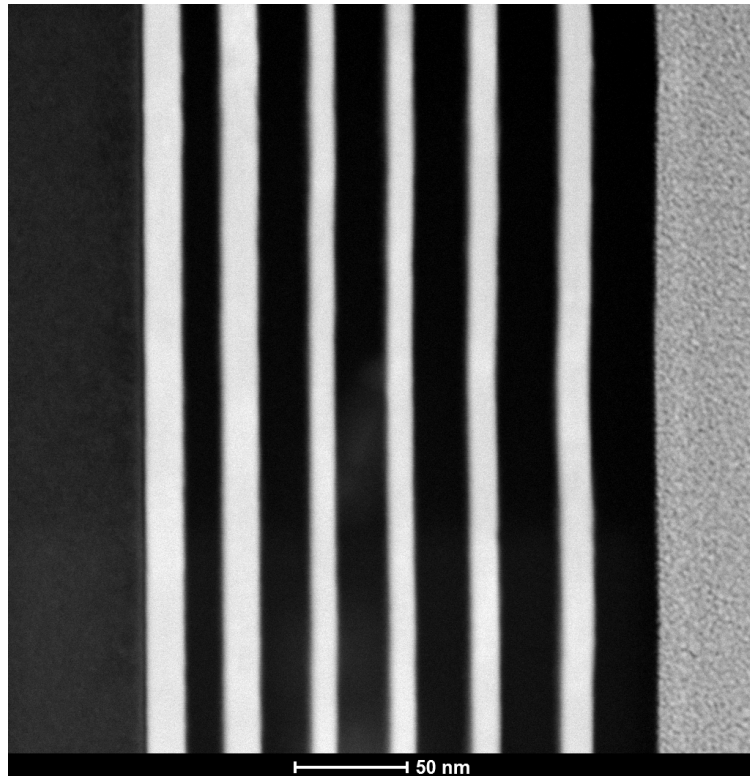


Figure 20. TEM of Unoptimized Layered ITO/SiO₂ Metamaterial. It was designed for 6 periods with metal and dielectric layers of 20 nm thickness. The gray material on the right is a platinum layer used in the imaging process, but was not there for the measurements of optical properties. Taken by Cynthia Bowers at AFRL/RX.

Figure 20 shows that the general desired structure was achieved, but the layers are not all exactly at the designed thickness. Later the real metal fractions are derived from this image and the TEM images of the other test samples. The thickness discrepancy should be observable in the measurements of the linear optical properties, and those results will be discussed in the next section.

4.3 Linear Measurement Results

First, ellipsometry was used on special samples which are simply single layers of one of the constituents of the full metamaterial. This allows for a much more accurate effective medium model. The results of these measurements, with error bars from the fitting process, are shown in Figure 21.

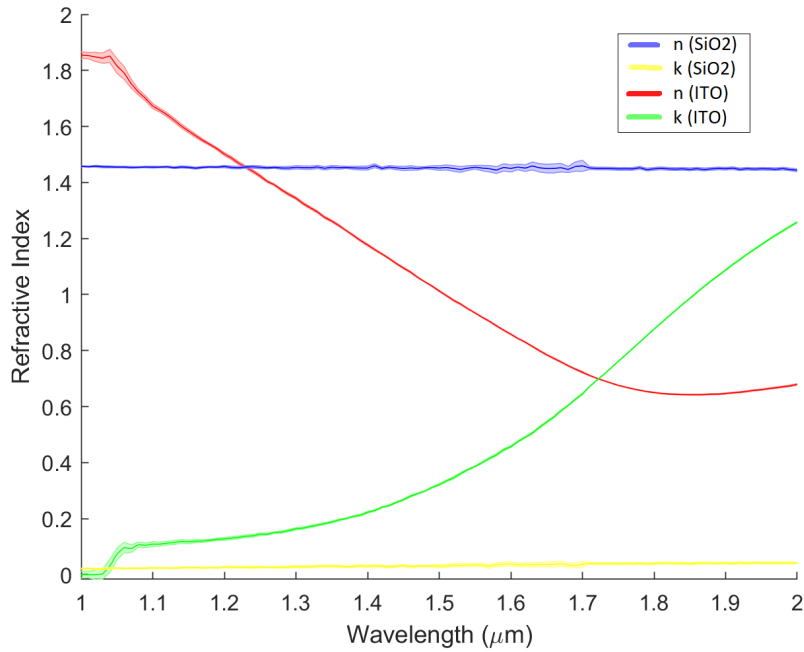


Figure 21. Complex Refractive Index for the Constituents of the Layered Metamaterial. There are error bars in this plot that come out of the ellipsometric measurement process, refer to section 3.2.2 for information.

From Figure 21, it is clear that the ITO does indeed behave as a metal while SiO₂ does behave as dielectric. However, there is one discrepancy with the linear results

of ITO. The measured values of the ITO properties do not match up well with the values found in the literature. Figure 22 shows the difference between the book values and the measured values in terms of permittivity.

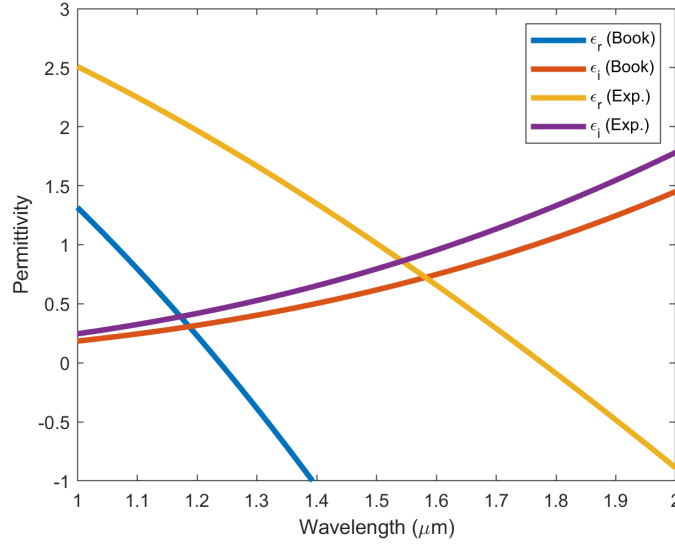


Figure 22. Comparison between Literature Values and Measured Values for ITO. There is a significant difference, and the ENZ point for ITO is shifted from around 1.25 microns to around 1.7 microns.

The reason for this discrepancy is not definitive, but the most likely cause is that the stoichiometric properties of the ITO used in this project were different than what is typically used in the literature. By that, what is meant is the ratio of indium to tin in the ITO in the samples. This discrepancy leads to different plasma frequencies when the properties are fit to a Drude model, which impacts all the models that use the plasma frequency. The literature plasma frequency is $4.73 * 10^{14} Hz$ and the plasma frequency derived from the measurements is $3.55 * 10^{14} Hz$. Even though the precise reason for the divergence was not known, the only option was to move forward using the measured ITO properties as the truth data. With these properties in hand, a model was created and compared to the ellipsometric values. Figure 23 shows a comparison of the model to the experimental values with a different number of periods

and Figure 24 shows a comparison of the model to the experimental values for the same metal fraction and number of unit cells, but different incidence angles.

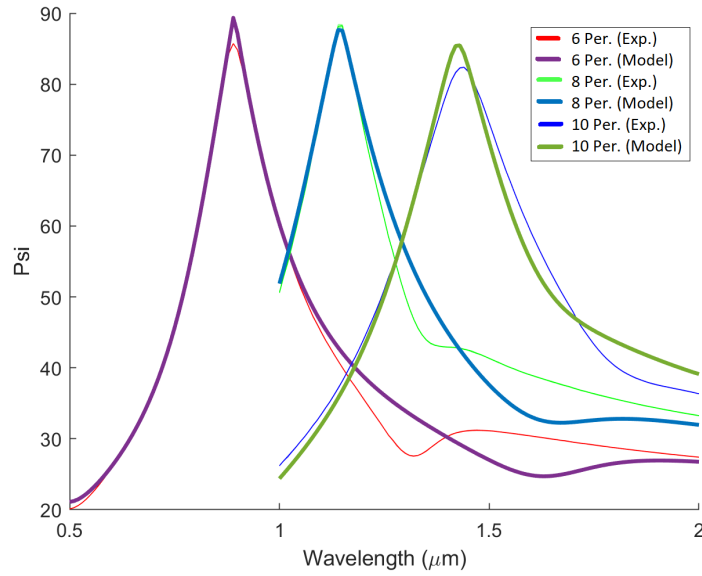


Figure 23. Comparison of Model and Experimental Ellipsometric Psi Data for ITO/SiO₂ Metamaterial for different numbers of unit cells. This experimental data was taken at 65° incidence, with 0.5 metal fraction design. The measurement matches up well with the EMA.

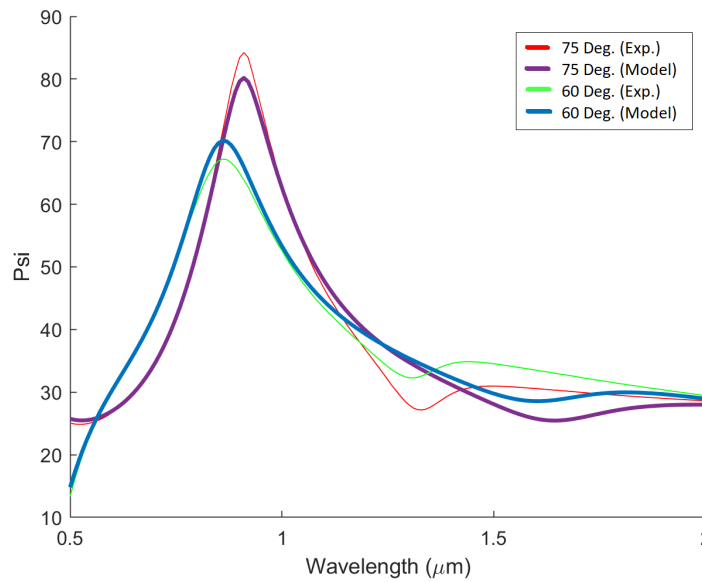


Figure 24. Comparison of Model and Experimental Ellipsometric Psi Data for ITO/SiO₂ Metamaterial for different incidence angles. This experimental data was taken for 6 periods, with 0.5 metal fraction design. The measurement matches up well with the EMA.

Another way to verify the effective medium model is to see if the fit parameters match up with the design parameters. Note that exactly the same model was used for each of the different numbers of periods, therefore the only difference between the models for different numbers of periods is the overall thickness of the sample. In determining the models, both the thickness of each of the three systems, along with the metal fraction, were selected as the fit parameters. The best fit values matched very closely with the thicknesses and metal fractions determined from the TEM images. Table 5 shows a comparison of the values from the TEM images and the values from the effective medium model.

Table 5. Comparison of Design, TEM, and Modeled Metal Fractions for each of the Three Different Designs.

Design Metal Fraction	TEM Metal Fraction	Modeled Metal Fraction
0.5	0.39	0.41
0.285	0.24	0.22
0.2	0.167	0.13

So it is the case that the actual metal fraction is lower than the design metal fraction, but the effective medium model is able to pick up on that and accurately represent the properties.

Another indication of accuracy is how the modeled overall thickness changed with the number of periods. The difference in the overall thickness follows closely with what is expected by the addition of more unit cells. For example, the TEM images showed that for the 0.5 metal fraction design, each period was about 35 nm. For the 6 periods system, the overall thickness was 209 nm, for 8 periods, 278 nm, and for 10 periods it was 352 nm. Thus the overall thickness is increasing by 35 nm for each period as expected.

For all these reasons, it is concluded that the effective medium model works well

for these metamaterial systems. Now that the model has been verified, Figure 25 shows the actual optical properties of one of the metamaterials.

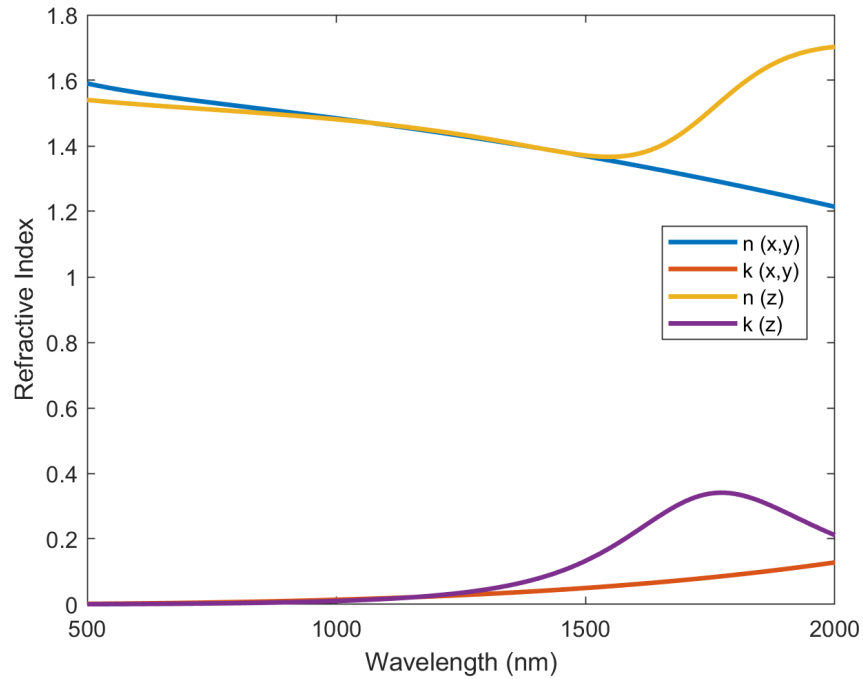


Figure 25. Extracted Linear Anisotropic Optical Properties for ITO/SiO₂ metamaterial with 0.5 metal fraction design. The ENZ point of this material is near 1.7 microns.

Figure 25 clearly demonstrates the anisotropic nature of these metamaterials, which happens primarily at longer wavelengths. Later in the project, more unoptimized samples were produced, however, there were issues with the metamaterial samples. Thus only the Drude model properties were confirmed using the ITO single layer samples which had been fabricated alongside the metamaterials. Figures 26 and 27 show the comparison of the Drude model (black lines) and ellipsometric data (red lines) for three incidence angles.

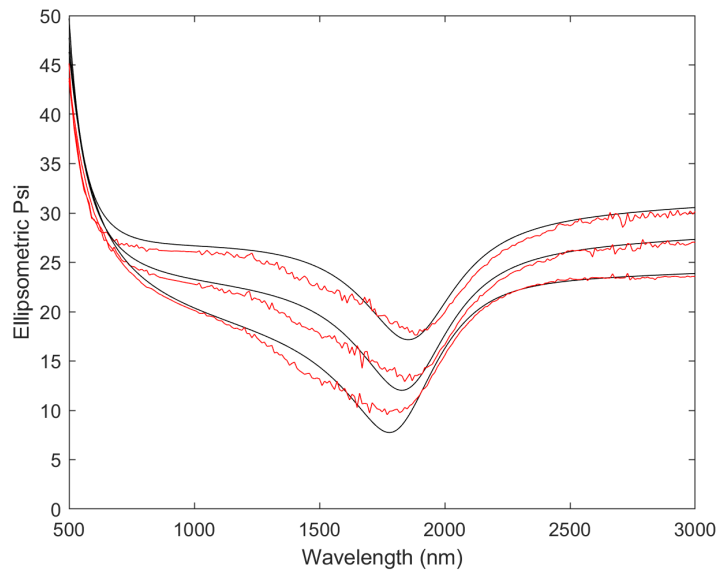


Figure 26. Comparison of ellipsometric Ψ between Drude model (black lines) and measurement (red lines) for an ITO film from October 2021. The data represents three incidence angles, 65, 70, and 75 degrees. There is good agreement.

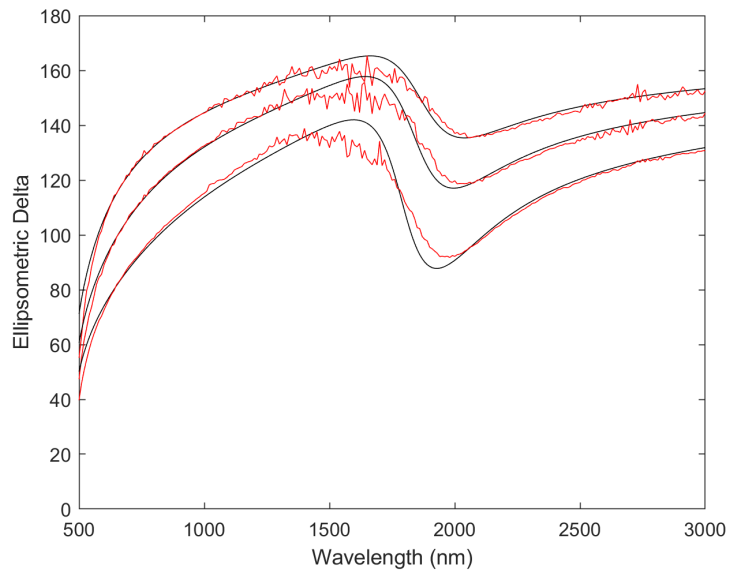


Figure 27. Comparison of ellipsometric Δ between Drude model (black lines) and measurement (red lines) for an ITO film from October 2021. The data represents three incidence angles, 65, 70, and 75 degrees. There is good agreement.

When doing these measurements to confirm the fit to the Drude model, it was realized that the Drude model parameters did not match the Drude parameters de-

rived from the first samples. Figure 28 shows the comparison to the ITO from the first measurements, in January 2021, to the ITO measured in October 2021, as well as the book values.

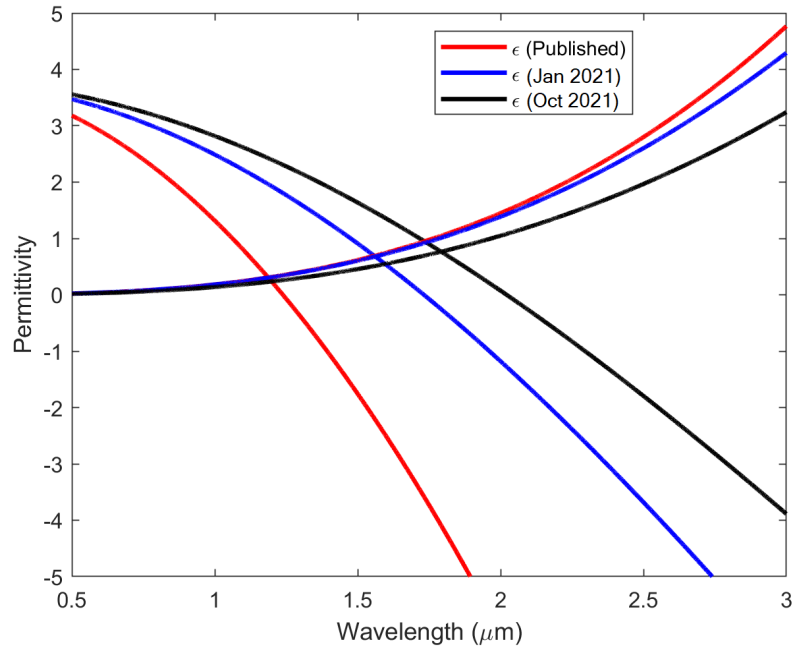


Figure 28. Updated Comparison between Literature Values and Different Measured Values for ITO. There is a significant difference, and the ENZ point for ITO is shifted from around 1.7 microns in the Jan. 21 fabrication to around 2.1 microns in the Oct. 21 fabrication.

At the time of fabrication, it was thought that this change was due to the ITO layers for this fabrication being deposited at 400 degrees Celsius rather than at room temperature as the previous samples were. However, later it was discovered that this was not the reason, and actually the reason was likely due to the deposition target being old and possibly depositing ITO contaminated with copper. Next, the non-linear measurements are presented.

4.4 Non-linear Measurement Results

The Z-scan technique was used to determine the non-linear properties at the wavelength of 1700 nm. This wavelength was chosen since it is an anisotropic region, where the metamaterial could have more applications. Figure 29 shows both open-aperture and closed-aperture data, with the dots as the experimental data, and solid line as the best fit properties.

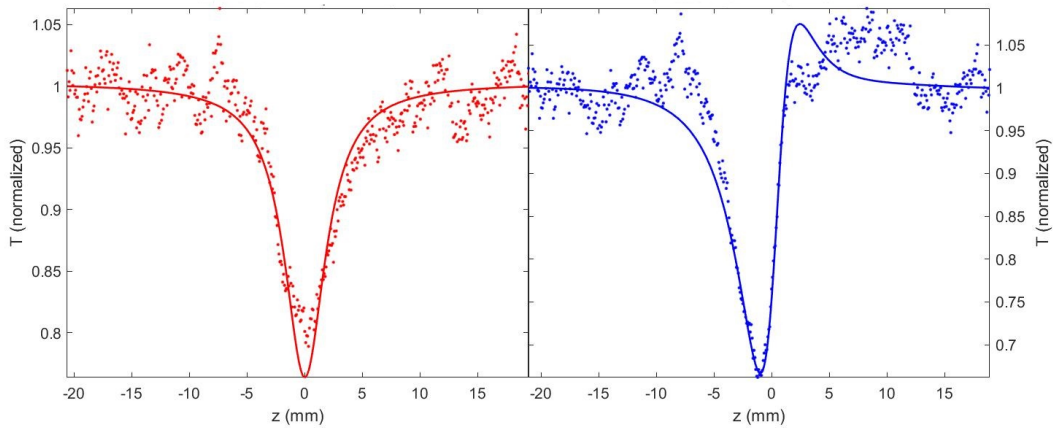


Figure 29. Open-Aperture and Closed-Aperture Z-scans of ITO/SiO₂ Metamaterial with 0.5 design metal fraction and 8 periods. The plot in red on the left is the open-aperture, and the plot in blue on the right is the closed-aperture.

From Figure 29, there is good agreement between the experimental data and the fitted properties. This fitting process was repeated for each of the samples, and similar results were found for each. There were some differences, but they were not consistent. It was expected that the results would change in a consistent fashion for the samples, but the fabrication issues made that difficult to be sure of. The fabrication TEM images make it clear that the layer thicknesses are not necessarily as consistent as was desired. However, it was possible to determine generally what the values of the non-linear properties are. Thus the non-linear properties determined

are $n_2 = 1 * 10^{14} \text{ cm}^2/\text{W}$, and $\beta = 2 * 10^{10} \text{ cm}/\text{W}$. These non-linear properties are stronger than those of many commonly used crystals and glasses. This demonstrates that these metamaterials, which are relatively easy to fabricate, have the potential to replace current systems for some applications. To confirm that the code to calculate the non-linear properties works, and to test if there is any special change in properties with intensity, similar measurements to those of Figure 29 were conducted at multiple powers. Figure 30 shows the open-aperture results of these Z-scans.

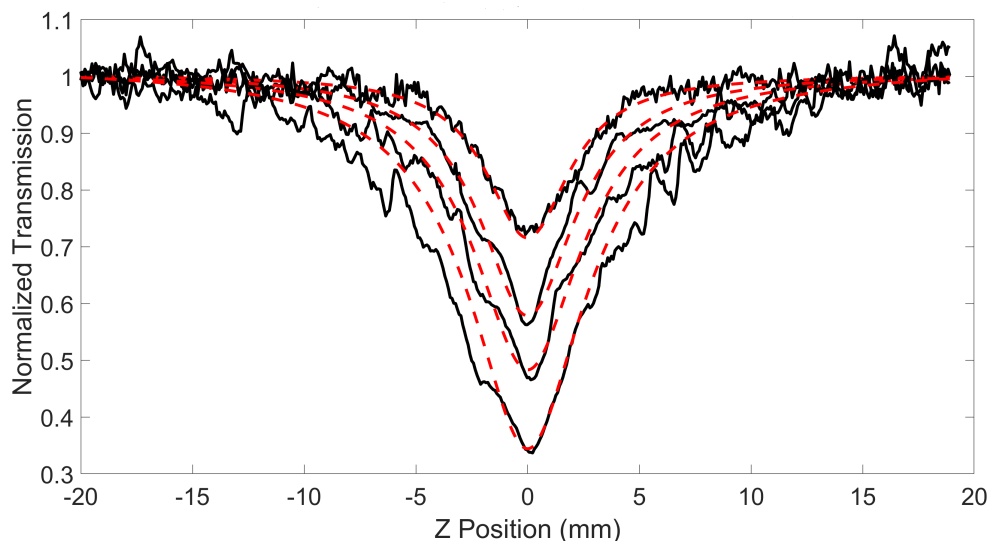


Figure 30. Open and Closed Aperture Z-scans of ITO/SiO₂ Metamaterial for Different Input Powers. The input power increases for the lower curves on the plot, since a higher power leads to stronger non-linear effects. The agreement becomes less strong as the higher powers are used.

There were many more Z-scan measurements of later samples, like the samples discussed at the end of the last section, but there were many issues with these measurements. The first issue is that original laser system went down, so a different laser system had to be used. Unfortunately, this laser had extreme power stability issues, even issues that were too great to account for with a reference detector. Also, the polarizer that was supposed to ensure TM polarization was highly inefficient due to alignment issues and may have been contributed to the power stability issues. In

addition, there were the probable fabrication issue where the samples may have been contaminated with copper. Lastly, analysis was made difficult due to the dominance of the substrate effect. Figure 31 illustrates the dominance of the substrate in open-aperture measurements.

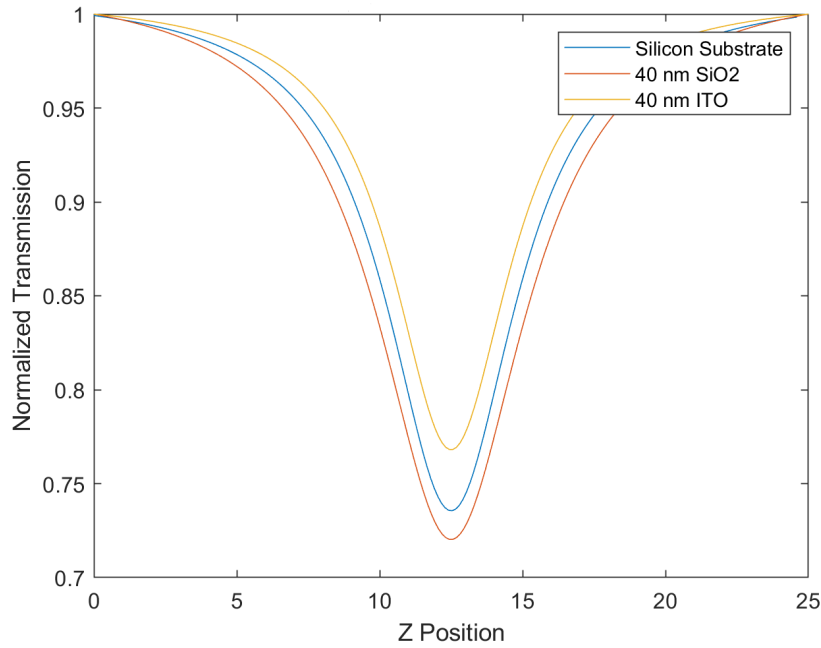


Figure 31. Average Open Aperture Z-Scans for Metamaterials Deposited on Silicon Substrate. These are representative Z-scans from the Z-scan simulation code rather than measurements, which allows to see that there was a small difference between the blank substrate and the substrate with the HMM applied. This difference was very difficult to analyze when the noise in the measurements was so high.

To fix the issue of substrate dominance, a fused silica substrate was used for the final fabricated samples. This substrate should have a very small open aperture response, which will be confirmed in section 5.5. All of the other measurement and fabrication issues were also resolved for the final optimized samples.

4.5 Summary

Results of the initial fabrication were presented, specifically the unoptimized test samples. Then the results that experimentally verified the proposed characterization methodology and provided the properties of the samples were examined, in both linear and non-linear respects. The results for optimized samples are given in the next chapter.

V. Final Results

5.1 Chapter Overview

In this chapter, the results of the final optimized designs are covered, first looking at the fabrication quality, then the linear results, and then the non-linear results. Lastly, an uncertainty analysis was performed which enables comparison of model to measurement. Note that this chapter generally contains the results that are contained within a journal article which is currently submitted to *Optical Materials Express* and is awaiting peer review.

5.2 Optimization Results

The basics of the optimization scheme were covered in section 3.5 with some examples in section 3.6. Here the settings of the scheme for the final optimization is discussed. For the final designs, the desired fitness functions are the switching intensity and the switching width. The switching intensity is defined here as the input intensity where the sign of the non-linear absorption changes, which is different than most definitions of the switching intensity. Most definitions in the literature are from all-optical switching applications where the material has already been placed in a tuned cavity, but this definition is for a specific HMM in free space. The definition used in this work makes sense for the special behavior of the HMMs as compared to other materials.

The other property optimized for here is the switching width, which is defined as the difference in transmission between the lowest transmission state and the highest transmission state. However, there is one issue that can arise with this in practice, since in some cases higher-order effects, such as fifth-order effects, can cause the modeled switching width to be lower than the actual third-order effects predict. To

avoid this, the maximum input intensity in the model was capped at the largest intensity used in the measurements, 200 GW/cm^2 , below where fifth-order effects started to appear. This allows for fair comparison between model and measurement, which will be discussed in section 5.7. These two properties are chosen as the outputs, but the inputs that are optimized over are the design geometries.

The design geometries are simply a pair of metal layer and dielectric layer thicknesses, with a random number of periods. Of course, there are bounds on design space that represent fabrication limits. The number of periods is allowed to vary from 6 to 12 and the layer thicknesses are allowed to vary from 40 to 200 nm, as less than 6 periods or 40 nm makes the effective medium properties less accurate and more than 12 periods or 200 nm leads to long fabrication times.

The two properties that were chosen to optimize for, which in this scheme means maximized, are the absolute value of the non-linear absorption coefficient and the absolute value of the derivative of linear transmission. Reference [4] found a correlation between the absolute value of the derivative of linear transmission and the switching capabilities of HMMs, and it is clear that a stronger absorption coefficient will correspond to a lower intensity where this switching behavior can be observed. The results of this optimization are shown in the next section. The absolute values need to be used for each parameter since these values can theoretically be positive or negative, to avoid how taking the maximum of positive and negative values would lead to ignoring the negatives.

So the outputs, or objective functions, were chosen to be the absolute value of the non-linear absorption and the absolute value of the derivative of the linear transmission. The inputs are simply the constituent material properties, the geometry, and the wavelength. The actual optimal designs were found using the optimization scheme discussed in section 3.5 with the above inputs and outputs. Figures 32 and

33 shows the results of the optimization.

For the final runs with the genetic algorithm, 200 population members with 1000 maximum generations were used to investigate the entire design space. Since there are two objective functions, the optimal designs make up a 2D Pareto front, which is a curve. Each population member is represented by a dot, and there is a one-to-one correspondence between specific design parameters and results. There are not necessarily 200 points on each Pareto plot, since some points are the same.

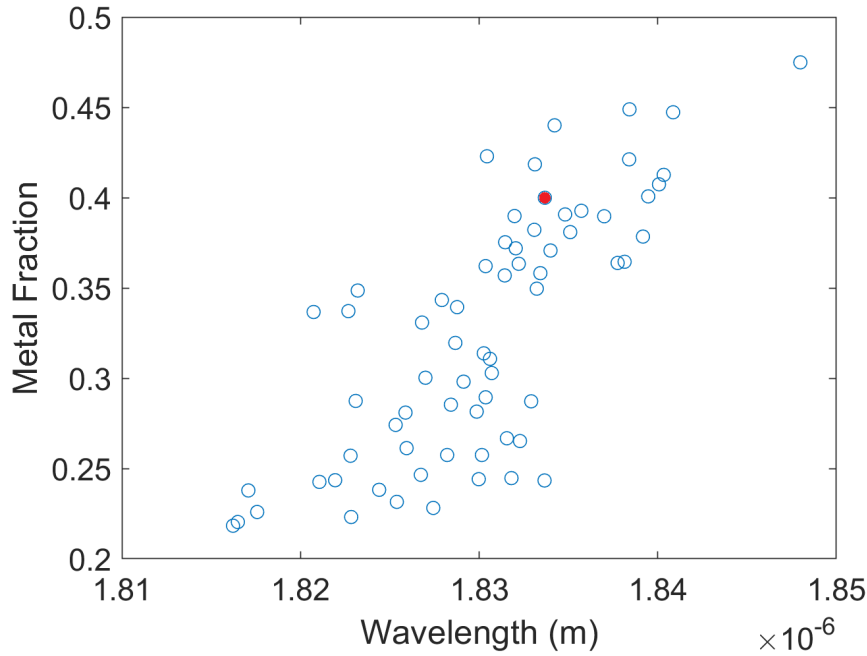


Figure 32. Pareto Front in Input Parameter Space for Optimized Designs. The input plot appears to be more scattered than the previous presented plots, however, this is simply because the optimal points are grouped closely together, so randomness in the genetic algorithm plays a large role. Note that the optimal wavelength for a 40% metal fraction geometry is around 1.835 microns from the parameter space plot, and that 40% metal design corresponds to a derivative of transmission of $-0.5 * 10^5$ and a non-linear absorption of $0.4 * 10^{-9} m/W$ on the function space plot. The chosen Pareto point for fabrication is highlighted in red.

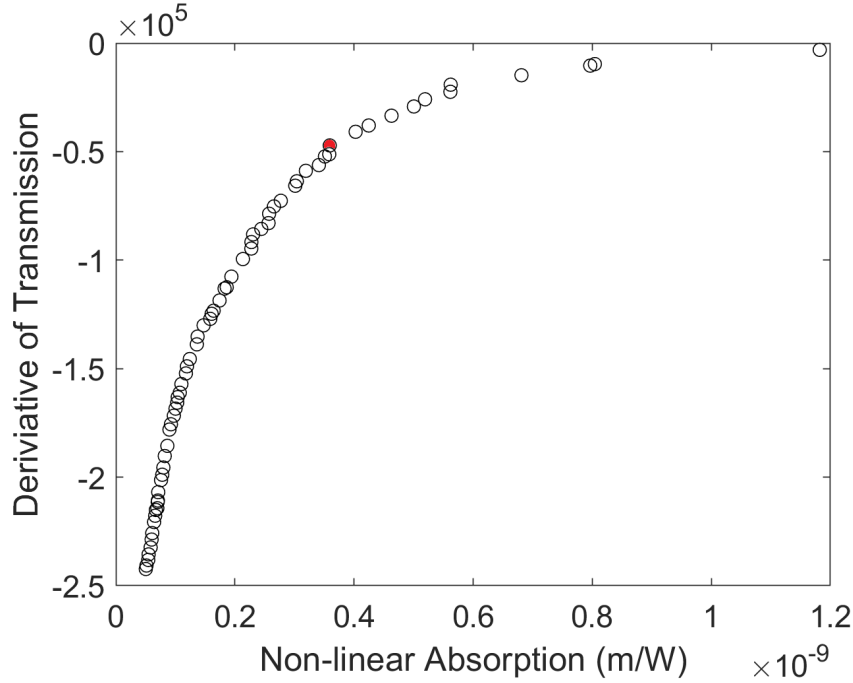


Figure 33. Pareto Front in Output Function Space for Optimized Designs. For the output plot, the absolute values were used for the optimization, but here the actual values are shown on the axes. The output space plot shows a trade-off that can be made between the derivative of transmission and the maximal non-linear absorption. This corresponds to a trade-off between the switching intensity and switching width. The 40% metal design corresponds to a derivative of transmission of -0.5×10^5 and a non-linear absorption of $0.4 \times 10^{-9} m/W$ on the function space plot. The chosen Pareto point for fabrication is highlighted in red.

Note any of the points on the input plot could be considered optimal designs, but for this work, the design recipe of a 40.7% metal fraction was chosen, corresponding to the red dot in Figure 32, which is a 55-nm layer of ITO and 135-nm layer of SiO_2 . Since all of the Pareto points can be deemed optimal, this was chosen somewhat arbitrarily. It is clear that the optimal wavelength is near 1.835 microns for this geometry, but linear measurements showed that the ENZ point of the materials actually falls closer to 1.78 microns, which will be shown from ellipsometry data in the next section. Thus, the optimal point for the special switching will actually occur off of the ENZ point, according to the model, which was verified by experiment and will be shown in section 5.5.

5.3 Fabrication Results

To verify that fabrication of the optimized designs was successful, transmission electron microscope (TEM) images of some of the samples were taken. Figure 34 shows a representative TEM image. From Figure 34, it can be seen that the layer deposition was successful, though there is some level of interface roughness that increases as more layers are deposited. Using image analysis software on the images with an included length scale, each individual layer thickness could be found. Then it is possible to calculate standard deviation in layer thickness, and this was found to be about 2.35 nm. Since a 40.7% metal fraction was the design goal, this implies that the true metal fraction falls between 38.3% and 43.2% for one standard deviation and 36% and 45.8% for two standard deviations.

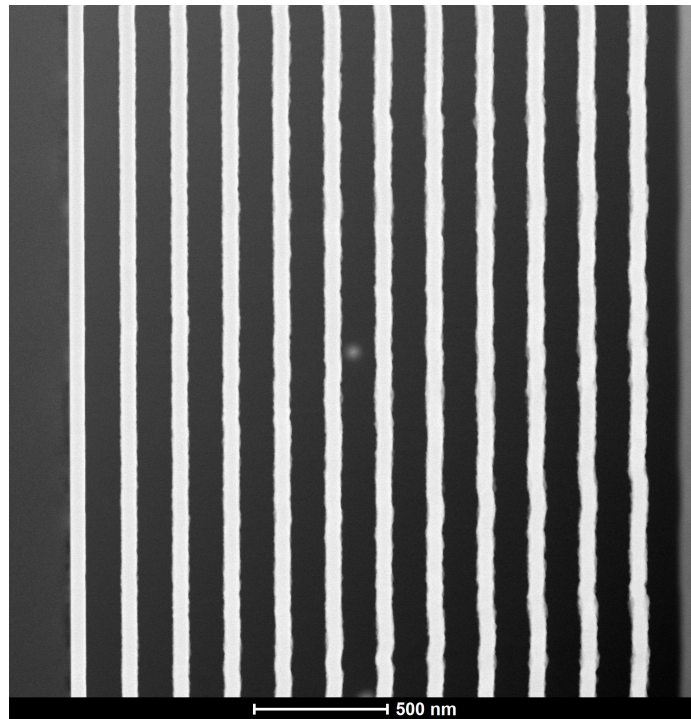


Figure 34. TEM image of a Representative Optimized Sample. The brighter layers are the ITO layers, and the darker layers are the SiO_2 . Note that the design for this image was 55 nm of ITO and 135 nm SiO_2 for a repetition of 12 periods, or 24 total layers on a silicon substrate. Later it will be shown that this geometry is in the range of optimal designs.

At this point, the discrepancy between the above designs and the proposed recipes that were listed in Table 4 needs to be covered. As discussed in section 3.2, there was a problem with the timed deposition, where the deposition rate changes as the targets were “broken in.” This led to the first fabricated samples to have varying layer thickness, but it also led the later samples to have larger layer thicknesses than the original design even through their layer thicknesses remained constant through the deposition. This effect will be shown in section 5.5. This turned out to be a benefit to the research, however. The original optimized designs were actually only optimal for the ITO measured in October 2021 (Figure 28) since that was the most recent data. As will be shown in the next section, the ITO actually deposited for these samples was very different. When the optimization was rerun with those ITO properties, optimization results were obtained that were presented in Section 5.2, and the metal fraction of the real samples, 40.7%, was actually one of the optimal points. Therefore, all the measurements in this chapter are indeed of optimally designed samples, even though they are not what the original optimal design was thought to be.

5.4 Linear Measurement Results

As before, ellipsometry was performed to verify the linear properties of the samples. For each of the samples, models in the ellipsometry software were fit to measured data in order to determine the accuracy of the Drude model and Maxwell-Garnett EMA. To do this, the mean-squared error (MSE) of the fits was calculated, with a lower MSE corresponding to a better fit. Refer back to section 3.3.2 for more information on the MSE if needed. For the final optimized samples, it was possible to confirm that the ITO layers did fit well to a Drude model, with a MSE of 4.7, which is in the range generally regarded as a successful fit [58, 67]. Figures 35 and 36 show the comparison of the Drude model (black lines) and ellipsometric data (red lines)

for three incidence angles.

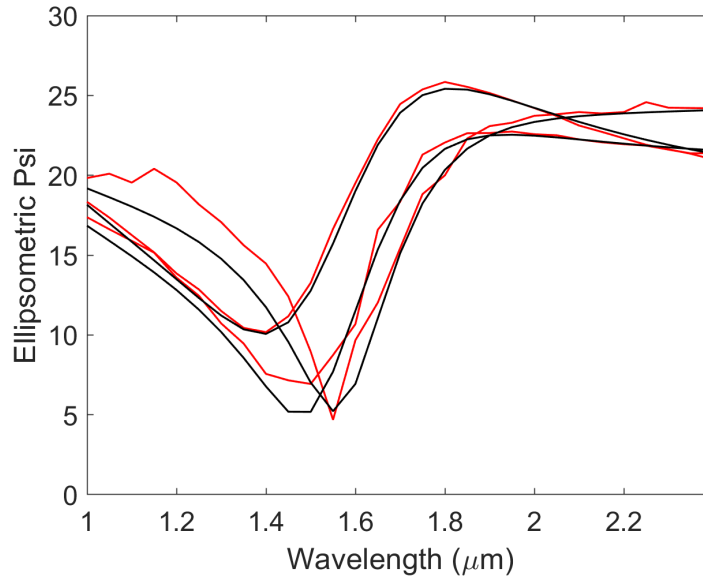


Figure 35. Comparison of ellipsometric Ψ between Drude model (black lines) and measurement (red lines) for an ITO film from January 2022. The data represents three incidence angles, 65, 70, and 75 degrees. The agreement is strong near the ENZ point of 1.7 microns, but diverges somewhat for small wavelengths.

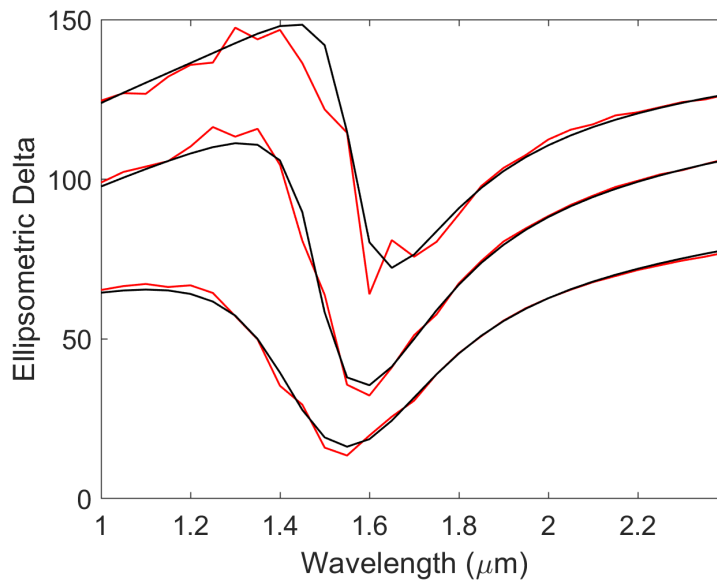


Figure 36. Comparison of ellipsometric Δ between Drude model (black lines) and measurement (red lines) for an ITO film from January 2022. The data represents three incidence angles, 65, 70, and 75 degrees. There is good agreement across the entire wavelength spectrum, which matches with the small MSE of 4.7.

When doing these measurements to confirm the fit to the Drude model, it was realized that the Drude model parameters did not match the Drude parameters derived from the first samples. Figure 37 shows the comparison to the ITO from the first measurements, in January 2021, to the ITO measured in October 2021, and the ITO measured in January 2022, as well as the book values.

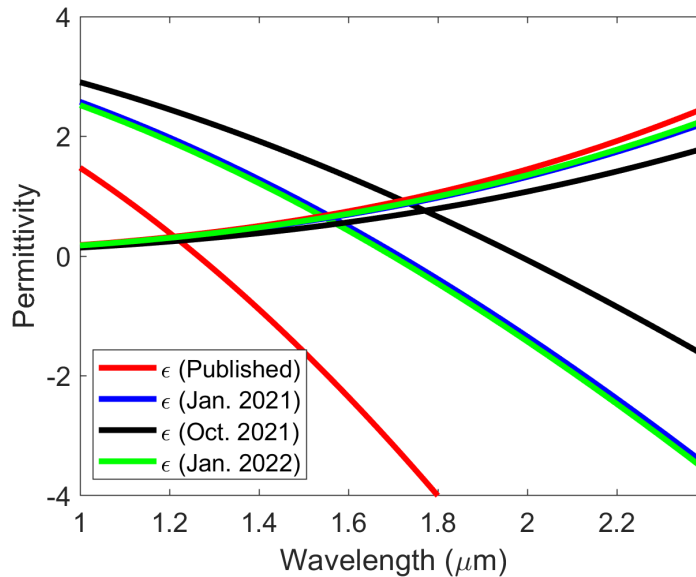


Figure 37. Final Comparison between Literature Values and Different Measured Values for ITO. There is a significant difference once again, and the ENZ point for ITO is shifted from around 2.1 microns in the Oct. 21 fabrication to around 1.7 microns in the Jan. 22 fabrication. However, there is good agreement between the two different January fabrications.

These results confirm the explanation mentioned in section 4.3, which is that new deposition targets were used in January 2021 and January 2022, and an old target was used in October 2022 that was possibly contaminated with copper. Next, the results of linear measurement of the hyperbolic metamaterials can be compared to the Maxwell-Garnett EMA. Overall, the Maxwell-Garnett EMA did work for modeling the linear properties of the fabricated HMMs, with a MSE of 20.7. This is higher than the ITO layers themselves, but it is still in an acceptable range. Figures 38 and 39 show this comparison. There was a mistake in the setup that caused the data only

to be taken out 1.7 microns. If data had been taken further out, the model could have performed better by having more data to fit.

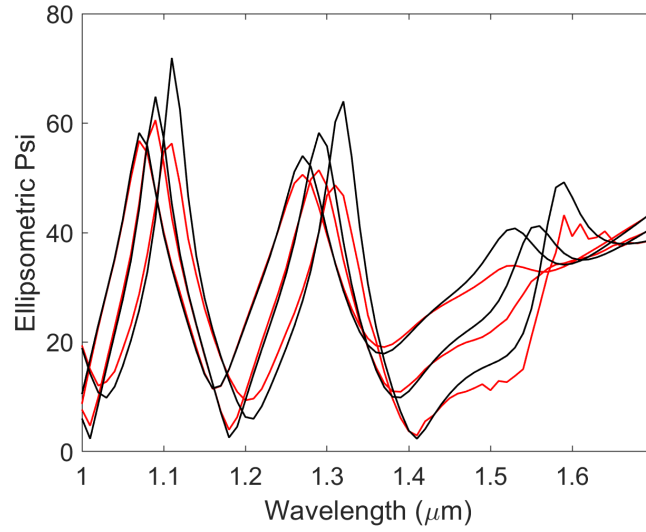


Figure 38. Comparison of Ellipsometric Δ between Maxwell-Garnett EMA (black lines) and measurement (red lines) for the Optimized Hyperbolic Metamaterial. The data represents three incidence angles, 65, 70, and 75 degrees. There is decent agreement, and it is clear that the EMA is capturing the correct trends in the hyperbolic metamaterial.

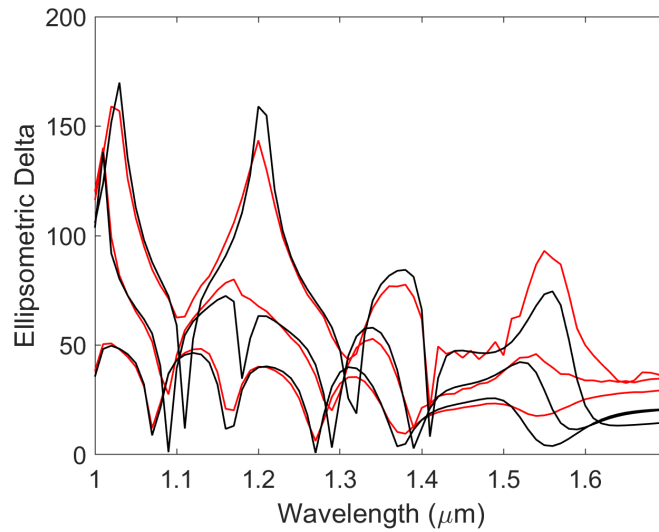


Figure 39. Comparison of Ellipsometric Δ Between Maxwell-Garnett EMA (black lines) and Measurement (red lines) for the Optimized Hyperbolic Metamaterial. The data represents three incidence angles, 65, 70, and 75 degrees. There is decent agreement, and it is clear that the EMA is capturing the correct trends in the hyperbolic metamaterial.

5.5 Non-Linear Measurement Results

The first non-linear measurements taken of the optimized samples were taken at too high an input intensity, so higher-order non-linear effects, that is fifth-order effects, were appearing in the results. On top of this, different behavior in the first three growths which had the same recipe was observed, which relates to the timed deposition problems discussed in Section 3.2. Figure 40 shows the first measurement results.

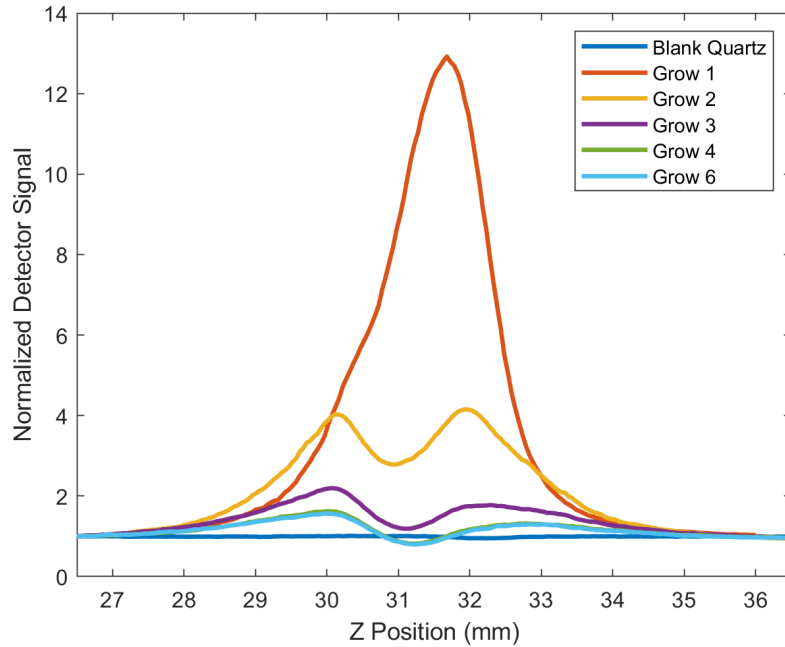


Figure 40. First Open-Aperture Z-scan Results for the Final Six Growths At Zero Degrees Incidence. Fifth-order effects can be seen in some growths.

The fifth-order effects can be seen in the results for growths 2, 3, 4, and 6. As discussed in the theoretical background, fifth-order effects also have a dependence on intensity at the fundamental frequency, and they do not necessarily have the same sign as the third-order effects. Therefore the shape seen in results is likely to be caused by these effects. Note that the results of growth 4 and 6 are the same, indicating that whatever issue impacted growths 1-3 was not an issue for growths 4-6. This is not

angle enhanced behavior, since this is at zero degrees, but is rather just a very high incident power. The later results with angle enhancement will be able to approach this kind of behavior with at least an order of magnitude less input intensity. To fix these issues, only growths 4, 5, and 6 were used for the final measurements and the input intensity was lowered significantly, by a factor of approximately 10-100. Then it was possible to observe only the linear and third-order effects. Figures 41 and 42 show the normalized transmission versus the Z-position for the open-aperture and closed-aperture Z-scans taken at a lower intensity.

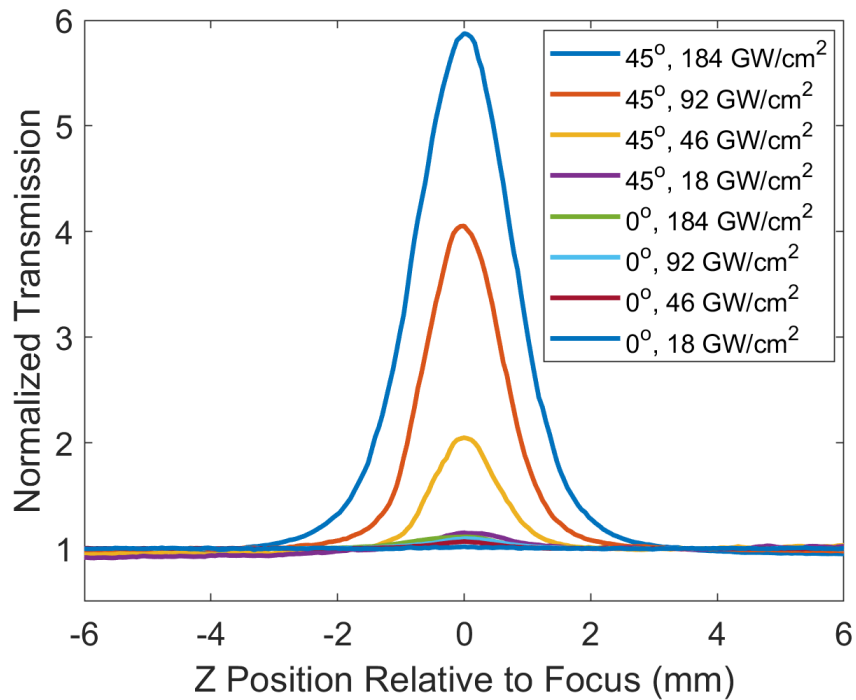


Figure 41. Open-aperture Measurements at 1.78 microns for Optimized Samples. This shows the strong field enhancement at an oblique angle for non-linear absorption. The magnitude of the results matches with reference [1], which was taken at a similar peak intensity. In general, the intensity increases as the Z position gets close to focus, which is set to 0.

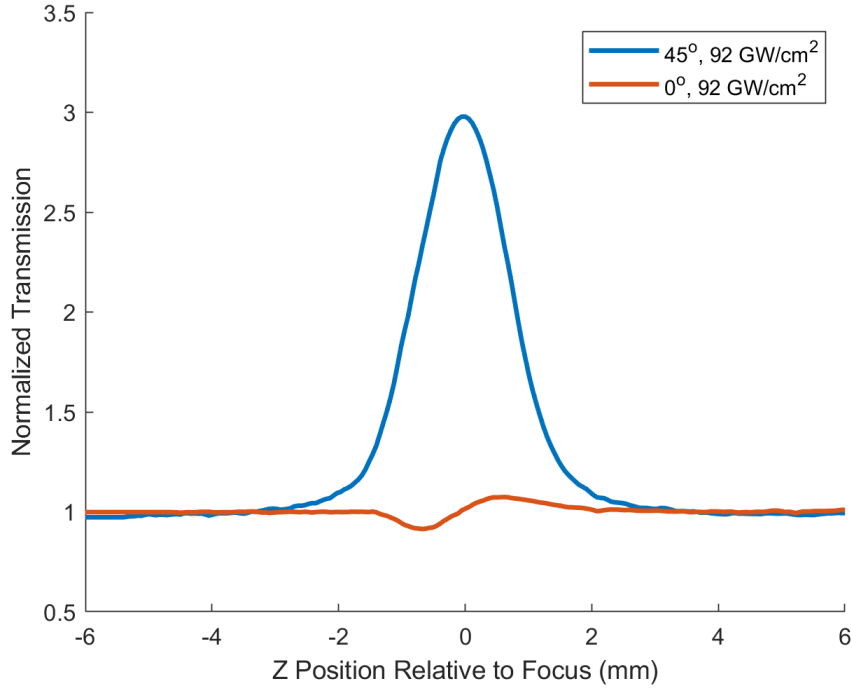


Figure 42. Closed-aperture Measurements at 1.78 microns for Optimized Samples. The signal at an oblique angle is dominated by non-linear absorption, while the signal at normal shows non-linear refraction. This matches with reference [1].

The first wavelength investigated was 1.78 microns, near the ENZ point of hyperbolic metamaterial. At this wavelength, the largest field enhancement of the material was observed as expected [1], but as stated in section 3.1, this is not the optimal wavelength to observe the actual switching behavior. This data serves as a valuable point of comparison for confirming the model predictions. The next wavelength measured was 1.835 microns, which is the optimal wavelength that came out of the optimization scheme, and these results are shown in Figures 43 and 44.

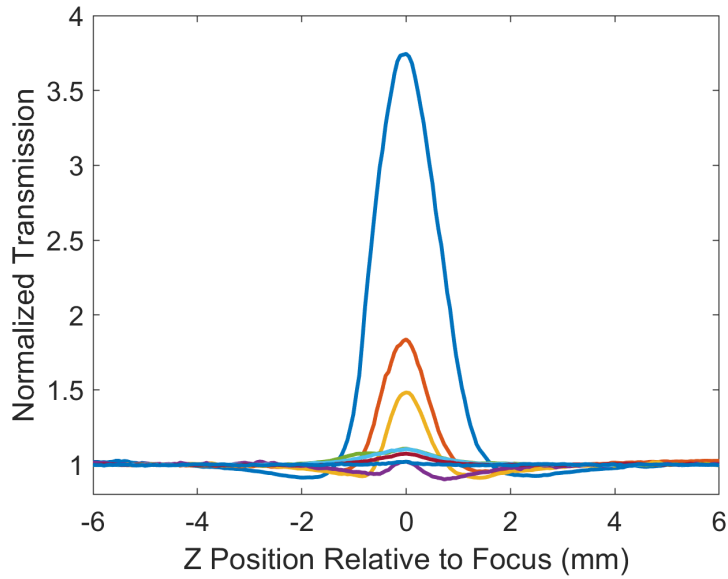


Figure 43. Open-aperture Measurements at 1.835 microns for Optimized Samples. There is non-linear absorption sign-changing in the 1.835 micron data, as seen when the normalized transmission becomes less than 1, then becomes greater than 1.

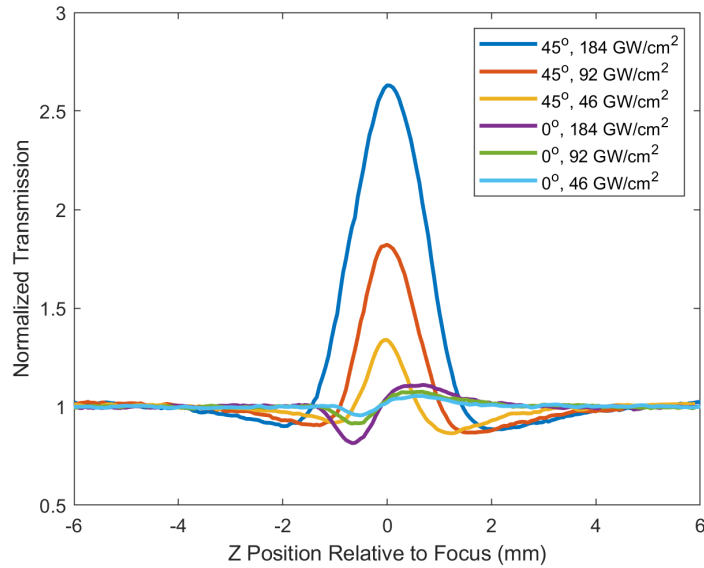


Figure 44. Closed-aperture Measurements at 1.835 microns for Optimized Samples. Again the signal at an oblique angle is dominated by non-linear absorption, while the signal at normal shows non-linear refraction. The special sign changing behavior is still observed at oblique incidence.

Figure 43 shows that at the design wavelength of 1.835 microns, behavior occurs

where the sign of the non-linear absorption coefficient changes from positive to negative. To rule out any confounding factors, Z-scan measurements of blank substrates were run, and nothing out of the ordinary was found. Also, multiple samples that were fabricated on different days were all found to have this sign-changing effect. Combined with the strong match of the modeled optimal wavelength to the wavelength where this special behavior is observed, where the model was only considering HMM behavior, it is likely that the HMM properties were the cause of this special behavior. To confirm this, Figure 45 shows the Z-scan fitting results of the substrate. It is possible to use the simulation code since the substrate does not have strong non-linear effects.

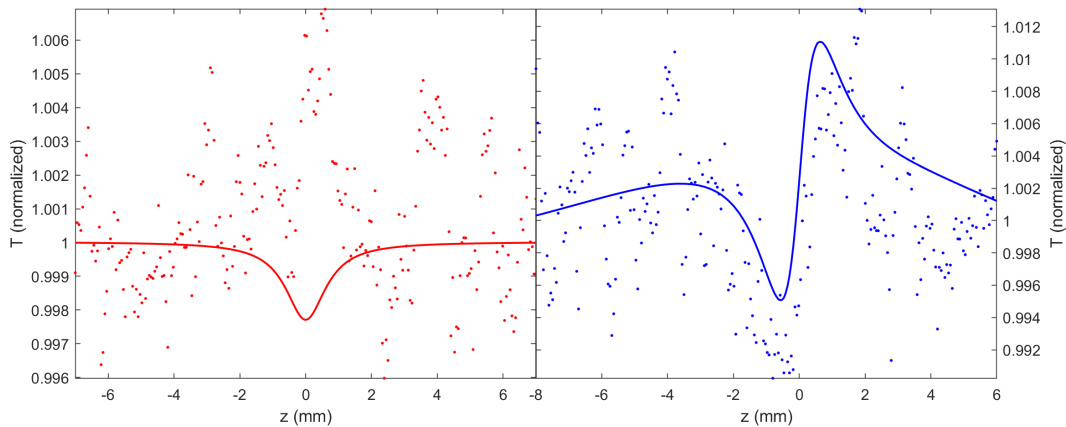


Figure 45. Data and Fit of Fused Silica Substrate Z-scan. This data was taken at zero degrees incidence, with an input intensity of 92 GW/cm^2 . The dots are the measured data, and the fit lines are represent the substrate properties that were used in modeling for the substrate. Clearly, the non-linear properties of the substrate are very small, since the normalized transmission does not even exceed 1.012 for either plot. The signal is small so noise in the measurement dominates.

So even with the same input intensity as the effects that lead to normalized transmission values of 4 for a HMM, there is no apparent non-linear signal from the substrate. Therefore, the substrate can be ruled out as a cause of any of the special effects.

The proposed explanation for the behavior is at 45 degrees and lower intensity the properties of the HMM are such that it would naturally exhibit saturable absorption, and for the behavior at higher intensity, the effective properties caused by the increase in electron density create a shift to reverse saturable absorption, which is then strengthened by the field enhancement. This is clearly a property of the HMM, since for isotropic materials, changing the input angle only could change field enhancement, and not the linear properties of the material. This was observed in literature [1]. The anisotropic nature of HMMs allows for special effective non-linear properties and an increased switching width due to control over the linear optical properties at each angle, remembering that the effective non-linear properties are simply the change from the linear properties. To verify that the trends in these results make sense, Figure 46 shows the relationship between angle-dependent transmission enhancement and peak intensity. The angle-dependent transmission enhancement is defined in equation (65).

$$TE = \frac{T_{45} - T_{45}^L}{T_0 - T_0^L}, \quad (65)$$

where T_0 represents the peak normalized transmission at 0 degrees, while T_{45} represents the peak normalized transmission at 45 degrees for the open-aperture Z-scans, which can be seen in Figures 41 and 43. This definition is used because it removes the influence of linear transmission, and it gives understanding of how much stronger the non-linear properties are at oblique angles compared to normal incidence. A value of ten would correspond to ten times stronger non-linear absorption at 45 degrees than at 0 degrees. These enhancement values should be proportional to the enhancement of the effective non-linear properties, since the linear effects have been subtracted out by subtracting 1 from each normalized transmission peak.

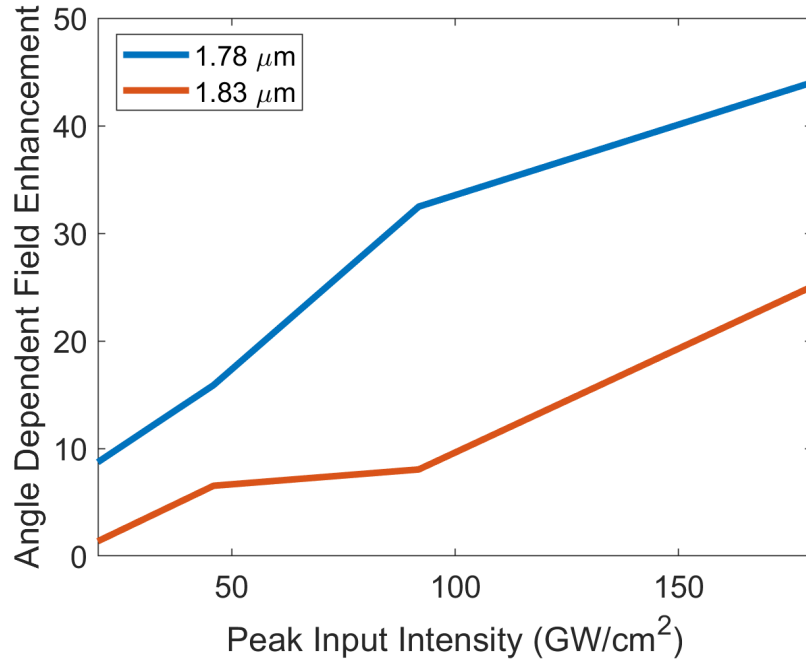


Figure 46. The Relationship of Transmission Enhancement at 45° with Peak Intensity. The maximum enhancement for 1.78 microns is 44, while for 1.835 microns it is 28.

The enhancement appears to be linear in intensity, but that cannot not necessarily be confirmed without more data points. The values shown here are similar to what has been reported in other works for ITO metal films [1]. This nearly linear relationship in Figure 46 makes sense, since the third order susceptibility, which gives rise to the non-linear part of the absorption coefficient in this case, is dependent on the incoming field squared, which is proportional to intensity.

5.6 Measurement-to-Model Comparisons

Once the novel behavior was confirmed with measurement, the next step is to confirm that the model is accurately capturing this behavior, accounting for measurement uncertainty. Figure 47 shows a visual explanation of the switching intensity and switching width.

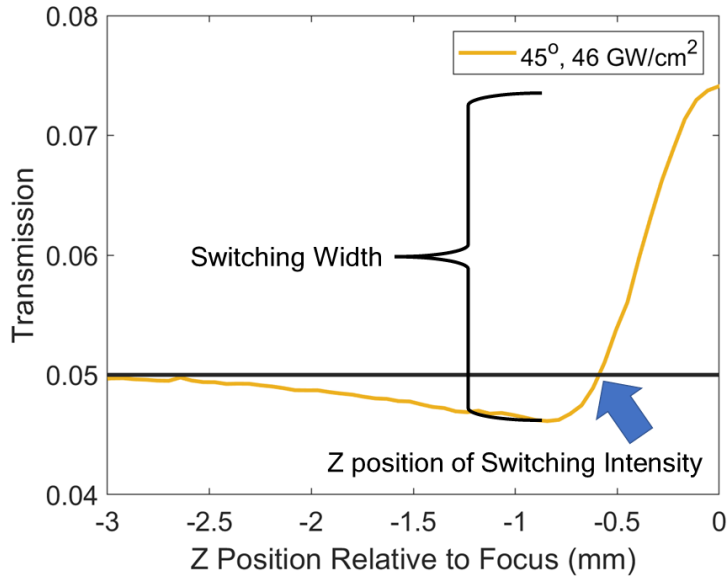


Figure 47. Visual Explanation of the Switching Width and Intensity. The data in the plot is one of the data sets from Figure 43, with the black line representing the linear transmission. Note that real transmission is plotted on the y-axis instead of normalized transmission, which is different than Figure 43. The switching width is simply the difference between the maximum and minimum transmission. The switching intensity is the intensity where the sign of the non-linear absorption coefficient changes from positive to negative. Knowing the z position of the switching intensity to some uncertainty allows for the calculation of the switching intensity.

The measurement uncertainty in the switching width was accounted for by calculating the variance in detector voltage for the Z-scan measurements. This value is small, generally the noise is less than 5%, but this uncertainty acts more as a noise floor, so with very small signals, the relative uncertainty can be higher. Note that this is calculated after removing the power fluctuations from the signal, as discussed in section 3.3.3. For all the uncertainty analysis, the partial derivatives of the defining equation are calculated, and are added in quadrature to derive an equation for the standard deviation of the quantity in question. The derivation process itself will not be shown, as it is not necessary for understanding of the method. Equation (66) defines the switching width, while equation (67) defines the switching width standard deviation.

$$SW = \frac{V_{max}}{V_{air}} - \frac{V_{min}}{V_{air}}, \quad (66)$$

$$\sigma_{SW} = SW \sqrt{2 \left(\frac{\sigma_{V_{air}}}{V_{air}} \right)^2 + \left(\frac{\sigma_{V_{max}}}{V_{max}} \right)^2 + \left(\frac{\sigma_{V_{min}}}{V_{min}} \right)^2}, \quad (67)$$

where V_{max} is the maximum detector voltage recorded for the sample, V_{min} is the minimum detector voltage for the sample, V_{air} is the detector voltage with no sample, and SW is the switching width. In this case, $\sigma_{V_{max}}$ and $\sigma_{V_{min}}$ are the same, since they come from the same measurement. Figure 48 shows the results of equations (66) and (67), along with the modeled values.

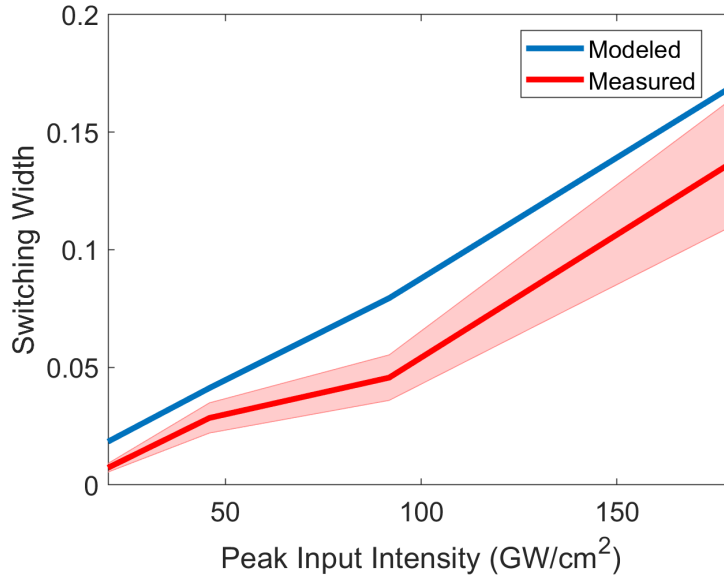


Figure 48. The Measured and Modeled Switching Width of the Sample, with Measurement Uncertainties. The solid line represents the modeled or measured values, while the lighter region represents one standard deviation. There is a systematic bias of the model to produce a larger switching width than the measurement, which is likely due to the modeled layer thickness parameters being slightly off from the real thicknesses due to fabrication error. Note that this is for only one standard deviation in the measurement, so for two standard deviations, which is well within the realm of possibility for the fabrication, there would be agreement. Also note that there is some error in the correlation of a specific measured switching width a specific intensity, which would widen the measurement uncertainty more if that was included.

For the switching intensity, the Z position can be found from the Z-scan data.

There is uncertainty in this location, since the Z-scan data is only sampled at some discrete Z positions. In this work, 100 linearly spaced points between the Z positions relative to focus of -6 to 6 mm was used. It is very much possible to get lower uncertainty in the Z position since the stage itself has a very repeatable position, but the since the error analysis was conducted after the measurement, the error improvement that could have been achieved from a greater resolution was not known at that time. Next, the actual intensity is needed, which can be calculated using Gaussian beam propagation. The beam waist of the laser, ω_0 , was measured using a knife edge to be 15.2 microns, with an uncertainty of 1 micron, and the Rayleigh length, Z_R , to be 536 microns, also with an uncertainty of 1 micron. Equation (68) shows the formula to calculate the beam radius at any Z position [68], while equation (69) shows the uncertainty equation.

$$\omega = \omega_0 \sqrt{1 + \frac{z^2}{Z_R^2}}, \quad (68)$$

$$\sigma_\omega = \sqrt{\omega \left[\left(\frac{\sigma_{\omega_0}}{\omega_0} \right)^2 - \left(\frac{\sigma_z * z}{Z_R^2 * \omega} \right)^2 + \left(\frac{\sigma_{Z_R} * z^2}{Z_R^3 * \omega} \right)^2 \right]}, \quad (69)$$

where ω is the beam radius at position z . The average power of the beam was measured using an Ophir® power meter, which can be configured to give the standard deviation in its measurements. This average power measurement was performed in the same location as the sample before each Z-scan measurement, since using the same location prevents any errors from losses in the optical train. To get a comparison to previous results that used peak power instead of average power, the calculation is for peak power. Using the properties of the laser, namely the repetition rate of 10 kHz and the pulse width of 150 fs, this can be converted into peak power, with an accompanying standard deviation. Note that the repetition rate and pulse width

are assumed to have no uncertainty, since their uncertainty should be very small compared to the other factors. Standard deviation for the power is simply the known standard deviation in the average power divided by the duty cycle, which is 1.5×10^{-9} . Equation (70) shows the calculation of the switching intensity, while equation (71) is the calculation of the standard deviation.

$$SI = \frac{P_{peak}}{\pi\omega^2}, \quad (70)$$

$$\sigma_{SI} = \frac{SI}{\pi} \sqrt{\left(\frac{\sigma_{P_{peak}}}{P_{peak}}\right)^2 + \left(\frac{2\sigma_{\omega}^2}{\omega}\right)^2}, \quad (71)$$

where P_{peak} is the peak power. Figure 49 shows the results of equations (68) through (71), along with the modeled values.

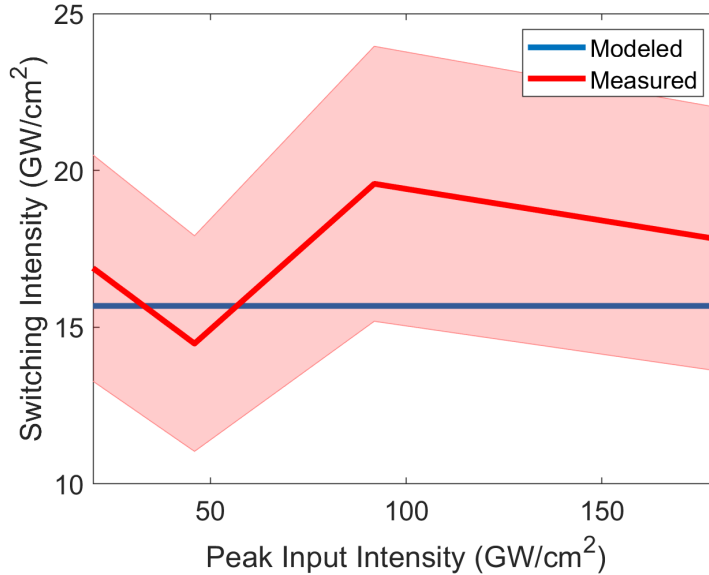


Figure 49. The Measured and Modeled Switching Intensity of the Sample, with Measurement Uncertainties. The solid line represents the modeled or measured values, while the lighter region represents one standard deviation. For the switching intensity, the uncertainty is larger, which is mainly due to the uncertainty in determining the actual z position of the intensity. This could be reduced in the future by using a finer sampling in the Z -scan measurement. Theoretically, the switching intensity should not change with input intensity, which is represented in the modeled values. Note that the model is within the bounds of the measurement uncertainty.

When considering the results of the comparisons in Figures 48 and 49, it is important to note that while all the measurement uncertainty has been accounted for, there is still the fact of imperfect fabrication, which is not in the models. In the model, perfectly flat layers, as well as consistent layer thickness, are used, therefore the remaining divergence between measurement and the model is attributed to fabrication challenges. However, the general behavior and trends in the HMMs are represented well. In the future, even better fabrication of these layered samples could lead to more accurate models.

The switching width and switching intensity measured and modeled in this work are similar to the few other results for non-linear HMMs. Source [4] used simulation to design HMMs for optical switching, and calculated switching widths ranging from 0.05 to 0.15, with switching intensities near 1 GW/cm². The current work requires a larger intensity, which is likely due to the fact that source [4] used a different material system with gold or silver as the metal layer and an operating wavelength in the visible. For a layered ITO/SiO₂ HMM, source [28] quotes a switching width defined as -5.17 dB for an input intensity of about 140 GW/cm² after converting from pulse fluence values. Converted into dB, the maximum switching width observed in this work is -6.2 dB at an input intensity of 180 GW/cm². So this work has demonstrated similar performance to source [28], which used the exact same material system ITO/SiO₂, and similar modeling techniques. That work was simulation only, so the measurement results which are unique to this work support the modeling conclusions of both groups. Overall, the close agreement gives confidence that the modeling results presented in this work are reasonable.

5.7 Summary

Results of the fabrication of the final optimized samples were presented. Then the results that experimentally verified the properties of the samples were examined, in both linear and non-linear respects. Lastly, comparisons between the model and measurement are made, with an uncertainty analysis. Next, an overall summary and some concepts for future work are given.

VI. Conclusion

6.1 Overall Summary

The research objective of the work was to make progress towards a hyperbolic-metamaterial-based optical switch that can provide improvements over current optical switches. Along the way, there were other objectives. The first objective was creating a fast-running model that can represent the behavior of the hyperbolic metamaterials. For the second objective, an optimization scheme was attached to that model. The third objective was the fabrication of needed test samples and optimized samples. The fourth objective was measurement, with both linear and non-linear measurements performed. The final objective was an uncertainty analysis, where the results of the measurements were directly compared to the model.

To meet these objectives, a fast running modeling scheme based on the two-temperature model and the non-linear effective medium was created. The implementation of the fast running modeling scheme was discussed in section 3.4, with references to theoretical background from Chapter II. Then this model was connected to a genetic algorithm optimization in MATLAB® , after confirming with *Lumerical* that the MATLAB® scheme was optimizing correctly. This is described in section 3.5. Next, initial tests of the optimization scheme were run, and this is shown in section 3.6. Lastly, the final optimization which resulted in the optimal sample designs was performed, which is detailed in section 5.2. The final optimization resulted in a 40% metal fraction design for the indium tin oxide (ITO) and silica (SiO₂) material system.

To fulfill the fabrication objective, the hyperbolic metamaterials were fabricated by physical vapor deposition using magnetron sputtering, and this is explained in section 3.2. Over the course of the effort, fabrication was continuously improved to

overcome challenges, and fabrication quality was confirmed with microscopy. Representative microscopy results of the test samples are shown in section 4.2, and results of the optimized samples are in section 5.3. The final optimized samples were able to match the optimal design which was ITO layers of 55 nm and SiO₂ layers of 135 nm, with 12 periods.

Many measurements were completed, including spectral ellipsometry for linear properties, and Z-scans for non-linear properties. The procedure for the ellipsometry measurements was covered in section 3.3.2, while the Z-scan procedure was covered in section 3.3.3. Linear and non-linear measurements of the test samples were taken, with the linear results in section 4.3 and the non-linear results in section 4.4. The linear results confirmed several aspects of the modeling scheme, for example, showing that the linear properties of the samples could be well represented by the Maxwell-Garnett EMA. Issues with the non-linear measurements such as the dominant substrate effects were discovered and worked through.

Also, linear and non-linear measurements of the optimized samples were taken, with the linear results in section 5.4 and the non-linear results in section 5.5. Results of linear measurements were presented, which again demonstrated that the linear properties of the samples could be represented by the Maxwell-Garnett effective medium approximation (EMA). Results of the non-linear Z-scan measurements showed a large enhancement of the effective non-linear properties at oblique incidence angles and switching behavior in which the sign of the non-linear absorption coefficient changed from positive to negative. The measured switching behavior has a switching intensity near 15 GW/cm² and switching width of about 0.15, which is comparable to the *modeling* results of other researchers [28]. Lastly, to complete the final objective, an uncertainty analysis was performed which shows that the model in this work was able to capture the trends in the real switching behavior of the samples. This is presented

in section 5.6.

From the final results, the overall research objective was achieved, since development of optical switches based on hyperbolic metamaterials was advanced. This was first time that heuristic optimization of these specific devices has been performed, and it is also the first time that modeling and simulation have been directly confirmed with measurement. With a robust characterization of the measurement uncertainty, this work provides a solid foundation for realization of practical hyperbolic optical switches, and possibly other applications, as will be discussed below.

6.2 Applications of Research

The main focus application of the work is optical switching. The current ITO/SiO₂ materials can offer a large switching width, with future work on choosing the material system as well as the geometry expected to increase the switching width further. The switching intensity is lower than a natural material by around an order of magnitude due to the field enhancement, but stronger methods of field enhancement, such as plasmonic nanoparticles, could lower the switching intensity even further. The switching time of these materials is already very small, as the electron temperature effects normalize in the time span of hundreds of femtoseconds, as seen in the two-temperature model results such as Figure 9. For all these reasons, this work has demonstrated that hyperbolic optical switches have the potential to become the future of optical memory for optical computing.

Besides optical switching, there are other possible applications. One application of the special behavior of these materials is tunable optical limiters. An optical limiter is a material with an absorption that increases with intensity, which will limit the output power to a designed maximum level for any input power. The strong change in absorption at oblique incidence angles in the samples could offer an optical

limiter that is mechanically tunable, as in controlled by its rotation, for control of its limiting intensity. Another application is materials for high power laser sources, since the controllable absorption properties of these materials allow for more control of laser outputs such as pulse shape, pulse compression, and pulse power, with pulse power being controlled by the same concept as the optical limiter.

6.3 Publications

The publications associated with this research are two conference proceedings papers and one journal article. The first conference proceedings paper [66] was presented at SPIE Optics and Photonics in August 2021 on the fabrication, linear measurements, and non-linear measurements of unoptimized test samples. Most of this information is presented in Chapter IV. The second conference proceedings paper [64] was presented at SPIE Photonics West in January 2022 on the optimization scheme and initial tests of the scheme. Most of this information is presented in section 3.5-3.6. Lastly, the journal article has been submitted to *Optical Materials Express* and is awaiting peer review. It covers the linear and non-linear measurements of the final optimized samples and is included in Chapter V. A copy of the submitted document is available upon request until it is published.

6.4 Recommendations for Future Research

More research is recommended to investigate related areas, where different properties could be chosen to optimize for in either a full-field computational scheme or a closed fast running scheme. Choosing different objective functions, such as maximizing non-linear refraction and minimizing absorption, could allow for quick optimization of many other devices. Some examples of other properties to test for include enhancement of non-linear refraction in a material with low linear absorption

and non-linear absorption, which would be a very valuable technology that was already shown to be possible to design in the optimization tests in Chapter 3. Other applications to optimize for are second-harmonic generation in non-centrosymmetric materials, and optimization of spontaneous parametric down-conversion for single-photon applications.

More specifically, one area of future work would be to test the same concept with other material systems. It is possible that much stronger switching behavior could be achieved with a different material system, such as switching out the ITO for gold or titanium nitride. Another avenue is to consider active modulation of the properties of the ITO layer, possibly by applying a voltage [69]. This could provide even more tunability of the non-linear properties. Other work could involve rerunning the computation scheme with more computational power and relaxing fabrication limitations to test the possible of very thin or very thick layers. The measurable fifth-order effects of these materials could also be studied.

Bibliography

1. M. Z. Alam, I. De Leon, and R. W. Boyd, “Large optical nonlinearity of indium tin oxide in its epsilon-near-zero region,” *Science*, vol. 352, no. 6287, pp. 795–797, 2016.
2. T. Tanabe, M. Notomi, S. Mitsugi, A. Shinya, and E. Kuramochi, “Fast bistable all-optical switch and memory on a silicon photonic crystal on-chip,” *Optics letters*, vol. 30, no. 19, pp. 2575–2577, 2005.
3. H. Gibbs, *Optical bistability: controlling light with light*. Elsevier, 2012.
4. M. Kim, S. Kim, and S. Kim, “Optical bistability based on hyperbolic metamaterials,” *Optics Express*, vol. 26, no. 9, pp. 11620–11632, 2018.
5. L. Ferrari, C. Wu, D. Lepage, X. Zhang, and Z. Liu, “Hyperbolic metamaterials and their applications,” *Progress in Quantum Electronics*, vol. 40, pp. 1–40, 2015.
6. A. Poddubny, I. Iorsh, P. Belov, and Y. Kivshar, “Hyperbolic metamaterials,” *Nature photonics*, vol. 7, no. 12, p. 948, 2013.
7. P. Shekhar, J. Atkinson, and Z. Jacob, “Hyperbolic metamaterials: fundamentals and applications,” *Nano convergence*, vol. 1, no. 1, p. 14, 2014.
8. T. Tumkur, L. Gu, J. Kitur, E. E. Narimanov, and M. Noginov, “Control of absorption with hyperbolic metamaterials,” *Applied Physics Letters*, vol. 100, no. 16, p. 161103, 2012.
9. J. Kim, V. P. Drachev, Z. Jacob, G. V. Naik, A. Boltasseva, E. E. Narimanov, and V. M. Shalaev, “Improving the radiative decay rate for dye molecules with hyperbolic metamaterials,” *Optics express*, vol. 20, no. 7, pp. 8100–8116, 2012.
10. T. Tumkur, G. Zhu, P. Black, Y. A. Barnakov, C. Bonner, and M. Noginov, “Control of spontaneous emission in a volume of functionalized hyperbolic metamaterial,” *Applied Physics Letters*, vol. 99, no. 15, p. 151115, 2011.
11. C. Cortes, W. Newman, S. Molesky, and Z. Jacob, “Quantum nanophotonics using hyperbolic metamaterials,” *Journal of Optics*, vol. 14, no. 6, p. 063001, 2012.
12. D. Lu, J. J. Kan, E. E. Fullerton, and Z. Liu, “Enhancing spontaneous emission rates of molecules using nanopatterned multilayer hyperbolic metamaterials,” *Nature nanotechnology*, vol. 9, no. 1, p. 48, 2014.
13. Y.-C. Chang, C.-H. Liu, C.-H. Liu, S. Zhang, S. R. Marder, E. E. Narimanov, Z. Zhong, and T. B. Norris, “Realization of mid-infrared graphene hyperbolic metamaterials,” *Nature communications*, vol. 7, no. 1, pp. 1–7, 2016.

14. K. Srekanth, A. De Luca, and G. Strangi, “Negative refraction in graphene-based hyperbolic metamaterials,” *Applied Physics Letters*, vol. 103, no. 2, p. 023107, 2013.
15. I. V. Iorsh, I. S. Mukhin, I. V. Shadrivov, P. A. Belov, and Y. S. Kivshar, “Hyperbolic metamaterials based on multilayer graphene structures,” *Physical Review B*, vol. 87, no. 7, p. 075416, 2013.
16. M. A. Othman, C. Guclu, and F. Capolino, “Graphene-based tunable hyperbolic metamaterials and enhanced near-field absorption,” *Optics express*, vol. 21, no. 6, pp. 7614–7632, 2013.
17. Y. Guo and Z. Jacob, “Thermal hyperbolic metamaterials,” *Optics express*, vol. 21, no. 12, pp. 15014–15019, 2013.
18. Y. Guo, C. L. Cortes, S. Molesky, and Z. Jacob, “Broadband super-planckian thermal emission from hyperbolic metamaterials,” *Applied Physics Letters*, vol. 101, no. 13, p. 131106, 2012.
19. K. V. Srekanth, Y. Alapan, M. ElKabbash, E. Ilker, M. Hinczewski, U. A. Gurkan, A. De Luca, and G. Strangi, “Extreme sensitivity biosensing platform based on hyperbolic metamaterials,” *Nature materials*, vol. 15, no. 6, pp. 621–627, 2016.
20. W. Gao, M. Lawrence, B. Yang, F. Liu, F. Fang, B. Béri, J. Li, and S. Zhang, “Topological photonic phase in chiral hyperbolic metamaterials,” *Physical review letters*, vol. 114, no. 3, p. 037402, 2015.
21. C. Argyropoulos, N. M. Estakhri, F. Monticone, and A. Alù, “Negative refraction, gain and nonlinear effects in hyperbolic metamaterials,” *Optics express*, vol. 21, no. 12, pp. 15037–15047, 2013.
22. X. Ni, S. Ishii, M. D. Thoreson, V. M. Shalaev, S. Han, S. Lee, and A. V. Kildishev, “Loss-compensated and active hyperbolic metamaterials,” *Optics express*, vol. 19, no. 25, pp. 25242–25254, 2011.
23. A. N. Poddubny, I. V. Iorsh, and A. A. Sukhorukov, “Generation of photon-plasmon quantum states in nonlinear hyperbolic metamaterials,” *Physical review letters*, vol. 117, no. 12, p. 123901, 2016.
24. A. Ghoshroy, W. Adams, X. Zhang, and D. Ö. Güney, “Enhanced superlens imaging with loss-compensating hyperbolic near-field spatial filter,” *Optics letters*, vol. 43, no. 8, pp. 1810–1813, 2018.
25. M. Shoaiei, M. K. Moravvej-Farshi, and L. Yousefi, “All-optical switching of nonlinear hyperbolic metamaterials in visible and near-infrared regions,” *JOSA B*, vol. 32, no. 11, pp. 2358–2365, 2015.

26. M. Shoaeei, M. K. Moravvej-Farshi, and L. Yousefi, "Switchable hyperbolic optical metamaterial based on kerr nonlinear effect," in *2014 Third Conference on Millimeter-Wave and Terahertz Technologies (MMWATT)*, pp. 1–4, IEEE.
27. A. D. Neira, G. A. Wurtz, P. Ginzburg, and A. V. Zayats, "Ultrafast all-optical modulation with hyperbolic metamaterial integrated in si photonic circuitry," *Optics express*, vol. 22, no. 9, pp. 10987–10994, 2014.
28. Z. T. Xie, Y. Sha, J. Wu, H. Y. Fu, and Q. Li, "Ultrafast dynamic switching of optical response based on nonlinear hyperbolic metamaterial platform," *Opt. Express*, vol. 30, pp. 21634–21648, Jun 2022.
29. E. Azmoudeh and S. Farazi, "Ultrafast and low power all-optical switching in the mid-infrared region based on nonlinear highly doped semiconductor hyperbolic metamaterials," *Opt. Express*, vol. 29, pp. 13504–13517, Apr 2021.
30. D. de Ceglia, M. A. Vincenti, S. Campione, F. Capolino, J. W. Haus, and M. Scalora, "Second-harmonic double-resonance cones in dispersive hyperbolic metamaterials," *Physical Review B*, vol. 89, no. 7, p. 075123, 2014.
31. E. G. Mironov, L. Liu, H. T. Hattori, and M. Richard, "Analysis of silica-filled slot waveguides based on hyperbolic metamaterials," *JOSA B*, vol. 31, no. 8, pp. 1822–1828, 2014.
32. K. Tanabe, "Field enhancement around metal nanoparticles and nanoshells: a systematic investigation," *The Journal of Physical Chemistry C*, vol. 112, no. 40, pp. 15721–15728, 2008.
33. K. Yao and Y. Liu, "Plasmonic metamaterials," *Nanotechnology Reviews*, vol. 3, no. 2, pp. 177–210, 2014.
34. A. Boltasseva and H. A. Atwater, "Low-loss plasmonic metamaterials," *Science*, vol. 331, no. 6015, pp. 290–291, 2011.
35. S. Kim, J. Jin, Y.-J. Kim, I.-Y. Park, Y. Kim, and S.-W. Kim, "High-harmonic generation by resonant plasmon field enhancement," *Nature*, vol. 453, no. 7196, pp. 757–760, 2008.
36. D. H. Werner, J. A. Bossard, Z. Bayraktar, Z. H. Jiang, M. D. Gregory, and P. L. Werner, "Nature inspired optimization techniques for metamaterial design," in *Numerical methods for metamaterial design*, pp. 97–146, Springer, 2013.
37. Z. H. Jiang, J. A. Bossard, X. Wang, and D. H. Werner, "Synthesizing metamaterials with angularly independent effective medium properties based on an anisotropic parameter retrieval technique coupled with a genetic algorithm," *Journal of Applied Physics*, vol. 109, no. 1, p. 013515, 2011.

38. J. Rayno, M. F. Iskander, and M. H. Kobayashi, "Hybrid genetic programming with accelerating genetic algorithm optimizer for 3-d metamaterial design," *IEEE Antennas and Wireless Propagation Letters*, vol. 15, pp. 1743–1746, 2016.
39. P. Chen, C. Chen, H. Wang, J. Tsai, and W.-X. Ni, "Synthesis design of artificial magnetic metamaterials using a genetic algorithm," *Optics express*, vol. 16, no. 17, pp. 12806–12818, 2008.
40. A. V. Kildishev, U. K. Chettiar, Z. Liu, V. M. Shalaev, D.-H. Kwon, Z. Bayraktar, and D. H. Werner, "Stochastic optimization of low-loss optical negative-index metamaterial," *JOSA B*, vol. 24, no. 10, pp. A34–A39, 2007.
41. S. Goudos and J. Sahalos, "Microwave absorber optimal design using multi-objective particle swarm optimization," *Microwave and Optical Technology Letters*, vol. 48, no. 8, pp. 1553–1558, 2006.
42. M. H. Tahersima, K. Kojima, T. Koike-Akino, D. Jha, B. Wang, C. Lin, and K. Parsons, "Deep neural network inverse design of integrated nanophotonic devices," *arXiv preprint arXiv:1809.03555*, 2018.
43. Y. Chen, J. Zhu, Y. Xie, N. Feng, and Q. H. Liu, "Smart inverse design of graphene-based photonic metamaterials by an adaptive artificial neural network," *Nanoscale*, vol. 11, no. 19, pp. 9749–9755, 2019.
44. W. Ma, F. Cheng, Y. Xu, Q. Wen, and Y. Liu, "Probabilistic representation and inverse design of metamaterials based on a deep generative model with semi-supervised learning strategy," *Advanced Materials*, vol. 31, no. 35, p. 1901111, 2019.
45. Z. Liu, D. Zhu, S. P. Rodrigues, K.-T. Lee, and W. Cai, "Generative model for the inverse design of metasurfaces," *Nano letters*, vol. 18, no. 10, pp. 6570–6576, 2018.
46. A. Sihvola, "Metamaterials in electromagnetics," *Metamaterials*, vol. 1, no. 1, pp. 2–11, 2007.
47. R. W. Boyd, *Nonlinear optics*. Academic press, 2019.
48. H. A. Lorentz, *The Theory of Electrons and Its Applications to the Phenomena of Light and Radiant Heat: A Course of Lectures Delivered in Columbia University, New York, in March and April, 1906*, vol. 29. Columbia University Press, 1909.
49. S. Anisimov, B. Kapeliovich, T. Perelman, *et al.*, "Electron emission from metal surfaces exposed to ultrashort laser pulses," *Zh. Eksp. Teor. Fiz*, vol. 66, no. 2, pp. 375–377, 1974.

50. N. Rotenberg, A. Bristow, M. Pfeiffer, M. Betz, and H. Van Driel, “Nonlinear absorption in au films: Role of thermal effects,” *Physical Review B*, vol. 75, no. 15, p. 155426, 2007.
51. R. W. Boyd, R. J. Gehr, G. L. Fischer, and J. Sipe, “Nonlinear optical properties of nanocomposite materials,” *Pure and Applied Optics: Journal of the European Optical Society Part A*, vol. 5, no. 5, p. 505, 1996.
52. F. Papoff and B. Hourahine, “Geometrical mie theory for resonances in nanoparticles of any shape,” *Optics express*, vol. 19, no. 22, pp. 21432–21444, 2011.
53. M. Born and E. Wolf, *Principles of optics: electromagnetic theory of propagation, interference and diffraction of light*. Elsevier, 2013.
54. J. A. Thornton, “Magnetron sputtering: basic physics and application to cylindrical magnetrons,” *Journal of Vacuum Science and Technology*, vol. 15, no. 2, pp. 171–177, 1978.
55. L. Sun, J. T. Grant, J. G. Jones, and N. R. Murphy, “Tailoring electrical and optical properties of al-doped zno thin films grown at room temperature by reactive magnetron co-sputtering: from band gap to near infrared,” *Optical Materials*, vol. 84, pp. 146–157, 2018.
56. N. R. Murphy, R. C. Gallagher, L. Sun, J. G. Jones, and J. T. Grant, “Optical and chemical properties of mixed-valent rhenium oxide films synthesized by reactive dc magnetron sputtering,” *Optical Materials*, vol. 45, pp. 191–196, 2015.
57. H. Tompkins and E. A. Irene, *Handbook of ellipsometry*. William Andrew, 2005.
58. J. A. Wollam, *Guide to Using WVASE Spectroscopic Ellipsometry Data Acquisition and Analysis Software*. J. A. Wollam Co. Inc, 1994.
59. P. Chapple, J. Staromlynska, J. Hermann, T. McKay, and R. McDuff, “Single-beam z-scan: measurement techniques and analysis,” *Journal of Nonlinear Optical Physics & Materials*, vol. 6, no. 03, pp. 251–293, 1997.
60. E. W. Van Stryland and M. Sheik-Bahae, “Z-scan measurements of optical nonlinearities,” *Characterization techniques and tabulations for organic nonlinear materials*, vol. 18, no. 3, pp. 655–692, 1998.
61. M. Reichert, H. Hu, M. R. Ferdinandus, M. Seidel, P. Zhao, T. R. Ensley, D. Peceli, J. M. Reed, D. A. Fishman, S. Webster, *et al.*, “Temporal, spectral, and polarization dependence of the nonlinear optical response of carbon disulfide,” *Optica*, vol. 1, no. 6, pp. 436–445, 2014.
62. M. R. Ferdinandus, M. Reichert, T. R. Ensley, H. Hu, D. A. Fishman, S. Webster, D. J. Hagan, and E. W. Van Stryland, “Dual-arm z-scan technique to extract

- dilute solute nonlinearities from solution measurements,” *Optical Materials Express*, vol. 2, no. 12, pp. 1776–1790, 2012.
63. P. Kabaciński, T. M. Kardaś, Y. Stepanenko, and C. Radzewicz, “Nonlinear refractive index measurement by spm-induced phase regression,” *Optics express*, vol. 27, no. 8, pp. 11018–11028, 2019.
 64. J. A. Ethridge, J. G. Jones, M. R. Ferdinandus, M. J. Havrilla, and M. A. Marciniak, “Linear and nonlinear properties of ito/sio2 layered metamaterials,” in *Active Photonic Platforms XIII*, vol. 11796, p. 117960U, International Society for Optics and Photonics, 2021.
 65. J. Sukham, O. Takayama, M. Mahmoodi, S. Sychev, A. Bogdanov, S. H. Tavassoli, A. V. Lavrinenko, and R. Malureanu, “Investigation of effective media applicability for ultrathin multilayer structures,” *Nanoscale*, vol. 11, no. 26, pp. 12582–12588, 2019.
 66. J. A. Ethridge, J. G. Jones, M. D. Ferdinandus, M. J. Havrilla, and M. A. Marciniak, “Efficient optimization of nonlinear optical devices with ito/sio2 layered hyperbolic metamaterials,” in *Optical Components and Materials XIX*, vol. 11997, pp. 37–45, SPIE, 2022.
 67. J. Pflüger and J. Fink, “Handbook of optical constants in solids ii,” 1991.
 68. W. Koechner, *Solid-state laser engineering*, vol. 1. Springer, 2013.
 69. S. Stankowski and J. J. Ramsden, “Voltage-dependent coupling of light into ito-covered waveguides,” *Journal of Physics D: Applied Physics*, vol. 35, no. 4, p. 299, 2002.

REPORT DOCUMENTATION PAGE

1. REPORT DATE 20220915	2. REPORT TYPE Dissertation	3. DATES COVERED	
		START DATE 20201002	END DATE 20220915
4. TITLE AND SUBTITLE Optimizing Optical Switching of Non-linear Hyperbolic Metamaterials			
5a. CONTRACT NUMBER	5b. GRANT NUMBER 2018-109, 2021-094	5c. PROGRAM ELEMENT NUMBER	
5d. PROJECT NUMBER	5e. TASK NUMBER	5f. WORK UNIT NUMBER	
6. AUTHOR(S) James Allen Ethridge			
7. PERFORMING ORGANIZATION NAME(S) AND ADDRESS(ES) AFIT/ENP 2950 Hobson Way, WPAFB, OH 45433			8. PERFORMING ORGANIZATION REPORT NUMBER AFIT-ENP-DS-22-S-042
9. SPONSORING/MONITORING AGENCY NAME(S) AND ADDRESS(ES) Air Force Office of Scientific Research 875 N Randolph St, Ste 325 Arlington AFB, VA 22203		10. SPONSOR/MONITOR'S ACRONYM(S) AFOSR/RTB1	11. SPONSOR/MONITOR'S REPORT NUMBER(S)
12. DISTRIBUTION/AVAILABILITY STATEMENT DISTRIBUTION STATEMENT A. Approved for public release: distribution unlimited.			
13. SUPPLEMENTARY NOTES			
14. ABSTRACT Modern optical materials are engineered to be used as optical devices in specific applications, such as optical computing. For optical computing, efficient forms of a particular device, the optical switch, have still not been successfully demonstrated. This problem is addressed in this research through the use of designed optical metamaterials, specifically, hyperbolic metamaterials, which offer the possibility of large non-linear properties with a low switching intensity. One-dimensional layered hyperbolic metamaterials composed of alternating layers metal and dielectric were used here, with ITO as the metal and SiO ₂ as the dielectric. The non-linear behavior of the ITO/SiO ₂ layered structure was first modeled and optimized. Samples were then fabricated using this optimized design through physical vapor deposition at the Materials and Manufacturing Directorate of the Air Force Research Laboratory, and the linear and non-linear properties of these samples were measured by ellipsometry and the Z-scan technique, respectively. These materials showed a large enhancement of their effective nonlinear properties, and an intensity dependent switching behavior where the sign of the non-linear absorption coefficient changes from positive to negative. This switching behavior has a switching intensity near 15 GW/cm ² and switching width of about 0.15. This is the first experimental demonstration of such behavior in a simple one-dimensional layered hyperbolic metamaterial. Since this behavior is tunable, this technique may now be used to further engineer devices for specific applications. The unique properties of these materials increase their potential for use in optical switching applications.			

15. SUBJECT TERMS

metamaterial, non-linear, hyperbolic, optical switch, genetic algorithm, optimization, Z-scan, ellipsometry

16. SECURITY CLASSIFICATION OF:**a. REPORT**

U

b. ABSTRACT

U

c. THIS PAGE

U

17. LIMITATION OF ABSTRACT

U

18. NUMBER OF PAGES

124

19a. NAME OF RESPONSIBLE PERSON

Michael Marciniak, AFIT/ENP

19b. PHONE NUMBER (Include area code)

(937) 255-3636 x4529